

**COMPUTATION OF STATISTICS FOR
POPULATIONS OF DIFFUSION
TENSOR IMAGES**

by

Casey Brett Goodlett

A dissertation submitted to the faculty of
The University of Utah
in partial fulfillment of the requirements for the degree of

Doctor of Philosophy

School of Computing

The University of Utah

August 2009

Copyright © Casey Brett Goodlett 2009

All Rights Reserved

THE UNIVERSITY OF UTAH GRADUATE SCHOOL

SUPERVISORY COMMITTEE APPROVAL

of a dissertation submitted by

Casey Brett Goodlett

This dissertation has been read by each member of the following supervisory committee and by majority vote has been found to be satisfactory.

Chair: Guido Gerig

Sarang Joshi

P. Thomas Fletcher

Edward Hsu

Carl-Fredrik Westin

THE UNIVERSITY OF UTAH GRADUATE SCHOOL

FINAL READING APPROVAL

To the Graduate Council of the University of Utah:

I have read the dissertation of Casey Brett Goodlett in its final form and have found that (1) its format, citations, and bibliographic style are consistent and acceptable; (2) its illustrative materials including figures, tables, and charts are in place; and (3) the final manuscript is satisfactory to the Supervisory Committee and is ready for submission to The Graduate School.

Date

Guido Gerig
Chair, Supervisory Committee

Approved for the Major Department

Martin Berzins
Chair/Dean

Approved for the Graduate Council

David S. Chapman
Dean of The Graduate School

ABSTRACT

The magnetic resonance imaging (MRI) technique known as diffusion tensor imaging (DTI) provides a unique method for investigating the architecture of neural white matter in human subjects *in-vivo*. DTI has a promising ability to better understand the biological root of disease in white matter between healthy subjects and those presenting white matter pathology or altered cognitive function. Because of the complexity of the acquired data, new image analysis techniques are essential to enable clinical research. This thesis presents a framework for evaluating tract specific group differences in populations of diffusion tensor images.

The ability of DTI to quantify diffusion parameters in living tissue requires a careful understanding of the imaging protocol and techniques for estimating diffusion parameters from measurements. An investigation of the effect of imaging noise on both tensor estimation and gradient sequence design is presented using both simulation and validation experiments. This evaluation provides recommendations for future studies as well as an understanding of potential confounds in retrospective analysis. Techniques for atlas building and tract-based analysis are developed to provide a reference coordinate frame for statistical analysis. Atlas building enables the study of a population of images in a common coordinate system. Novel validation measures for comparing streamline tractography results are used to evaluate the results of atlas tract identification. Tract-based analysis of diffusion measures within atlas space enables intuitive statistical methods for testing the differences of specific tracts. The statistical framework allows for joint analysis of multiple diffusion statistics and accounts for along tract correlation. These methods provides a generic framework for neuroimaging studies and has been demonstrated on clinical studies of normal development and schizophrenia to illustrate potential new findings as well as confirmation of previous studies.

For my grandfather Claude B Goodlett.

CONTENTS

ABSTRACT	iv
LIST OF TABLES	ix
LIST OF FIGURES	x
LIST OF ABBREVIATIONS	xii
ACKNOWLEDGMENTS	xiii
CHAPTERS	
1. INTRODUCTION	1
1.1 Motivation	1
1.2 Overview of White Matter Anatomy	3
1.3 Application Areas	5
1.3.1 Normal Development	5
1.3.2 Schizophrenia	6
1.3.3 Other Applications	7
1.4 Thesis and Contributions	8
1.5 Overview of Chapters	9
2. BACKGROUND	10
2.1 Diffusion Weighted Magnetic Resonance Imaging	10
2.1.1 Source of Diffusion Signal	10
2.1.2 Diffusion Tensor Model	11
2.1.3 Higher Order Models	12
2.1.4 Scalar Invariants	13
2.1.5 Fiber Tractography	16
2.2 Statistical Analysis of DTI	17
3. DIFFUSION WEIGHTED IMAGE PREPROCESSING	20
3.1 Introduction	20
3.2 Methods	22
3.3 ML Estimation of Rician Parameters	26
3.4 Simulation of Tensor Estimation	28
3.5 Experiments and Validation	31
3.6 Conclusions	37

4.	DTI ATLAS BUILDING	39
4.1	Introduction	39
4.2	Registration	39
4.3	Tensor Processing	43
4.3.1	Spatial Transformations of Tensor Images	43
4.3.2	Interpolation and Averaging of Tensor Images	45
4.4	Atlas Tractography	46
4.5	Experiments and Results	47
4.6	Preservation of Edges	47
4.7	Conclusion	51
5.	MEASURES FOR VALIDATION OF TRACTOGRAPHY ...	52
5.1	Introduction	52
5.2	Tractography Comparison Measures	53
5.2.1	Volumetric Overlap	53
5.2.2	Point Cloud Divergence	54
5.2.3	Ellipsoid Distance	56
5.2.4	Functional Difference	56
5.3	Evaluation of Atlas Tractography	57
5.4	Conclusion	60
6.	TRACT STATISTICS	62
6.1	Introduction	62
6.2	Tract Oriented Statistics	63
6.3	Functional Data Analysis	65
6.4	Example Results	70
6.5	Conclusion	74
7.	CLINICAL APPLICATIONS	75
7.1	Introduction	75
7.2	Study of Brain Development	75
7.2.1	Cross-Sectional Atlases of Development	76
7.2.2	Normal Development From One to Two years	76
7.2.3	Hypothesis Testing Between Controls and MVMs in Neonates .	83
7.3	Schizophrenia	89
7.4	Conclusion	89
8.	DISCUSSION	97
8.1	Summary of Contributions	97
8.2	Limitations	100
8.2.1	Atlas Building	100
8.2.2	HARDI	101
8.3	Additional Projects	103
8.4	Future Work	104
8.4.1	Improvement of Atlas Building	104
8.4.2	Physical Meaning of Diffusion Measures	105

8.4.3	Tract Oriented Analysis	106
8.4.4	Longitudinal Tract Oriented Statistics	106
8.4.5	Incorporating Covariates	107
9.	PUBLICATIONS	108
9.1	Journal Publications	108
9.2	Peer-Reviewed Conference Publications	108
9.3	Invited Presentations	109
9.4	Peer-Reviewed Short Papers and Workshops	109
APPENDICES		
A.	SOFTWARE USER GUIDE	110
B.	GRADIENT DIRECTION SCHEMES	130
	REFERENCES	133

LIST OF TABLES

3.1	Mean and variance of FA values in aligned and unaligned voxels.	37
3.2	Mean and variance of trace values in white matter.	37
5.1	Mean and standard deviation of geometric distance measures between warped atlas tract and individual tract over the population.	60
5.2	Mean and standard deviation of average absolute difference in FA and MD between atlas tract and warped individual tract.	60
5.3	Summary of measure advantages and disadvantages.	61
7.1	Tract differences from one to two years	86
7.2	Tract differences from neonate controls to MVMs	89
B.1	6 direction gradient list.	130
B.2	21 direction gradient list.	130
B.3	60 direction gradient list.	131

LIST OF FIGURES

1.1	Diagram of a neuron	4
2.1	The random walk of water molecules within anisotropic tissue such as an axon fiber bundle tends to travel more easily along the fiber bundle.	12
2.2	Example of noncrossing and crossing fibers.	13
2.3	Single streamline trace through a tensor field.	16
3.1	Geometric interpretation of Rician noise	23
3.2	Example of tensors with principal eigenvectors aligned or unaligned with a gradient direction.	24
3.3	Simulated comparison of ML estimation and averaging of DWI intensity.	27
3.4	The orientation dependence of estimated FA and trace under different sampling schemes.	29
3.5	Comparison of Frobenius norm of the difference between the estimated and true tensor in Monte Carlo simulations	29
3.6	Comparison of MD estimate in Monte Carlo simulations	30
3.7	Comparison of FA estimate in Monte Carlo simulations	30
3.8	Simulated estimation of FA for highly isotropic tensors.	32
3.9	Histograms from diffusion weighted images	34
3.10	Labels for aligned and unaligned voxels	35
3.11	Histograms of estimated FA using weighted least squares estimation for aligned and unaligned tensors	36
4.1	Flowchart of atlas building process.	40
4.2	Deformation of tensor fields into atlas space preserves the full information needed for fiber tractography and diffusion statistic analysis.	40
4.3	Comparison of FA and feature images.	42
4.4	Comparison of affine and diffeomorphic registration.	44
4.5	Axial slice of the FA and ellipsoids for the affine and deformable atlases	48
4.6	Fibers in atlas and corresponding fibers in subject space	49
4.7	FA gradient in affine and diffeomorphic atlases	50
5.1	Example of instability of overlap measures for thin structures.	54

5.2	Closest point distances for atlas and individual tractography results for the right cingulum in a subject.	55
5.3	Histogram of closest point distances from atlas tract to individual tract.	55
5.4	Ellipsoid representation of bundle shape.	57
5.5	Mean and standard deviation of differences between functions produced by atlas tractography and individual tractography mapped to atlas for the right uncinate.	58
5.6	Fiber bundles in population atlas.	59
6.1	Diffusion properties within a fiber bundle are summarized as a function of arc length	64
6.2	Schematic diagram of tract analysis procedure.	65
6.3	Visualization of the PCA modes for the joint analysis of FA and FRO	69
6.4	Discriminant for genu tract	72
6.5	Discriminant for left motor tract	73
7.1	Axial slices of atlases at neonate, 1 year, 2 year, and adult.	77
7.2	Axial slices of all subjects after nonlinear registration	79
7.3	Comparison of atlas and individual tractography	80
7.4	Tract and arc length functions for genu	81
7.5	Tract and arc length functions for splenium	82
7.6	Tract and arc length functions for left cortico-spinal tract	84
7.7	Tract and arc length functions for right cortico-spinal tract	85
7.8	Discriminant function for the genu tract	86
7.9	Discrimination function left cortico-spinal tract	87
7.10	Template fiber tracts in atlas of neonate subjects overlaid on the FA image of the neonate atlas.	88
7.11	Discriminant for splenium from control to MVM groups	88
7.12	Fiber bundles for analysis of schizophrenia data.	90
7.13	Functions and discriminant for fornix	91
7.14	Functions and discriminant for left uncinate	92
7.15	Functions and discriminant for right uncinate	93
7.16	Functions and discriminant for left cingulum	94
7.17	Functions and discriminant for right cingulum	95
8.1	FA image and fiber tracts from atlas of adults.	104

LIST OF ABBREVIATIONS

ADC	apparent diffusion coefficient
CSF	cerebrospinal fluid
DWI	diffusion weighted imaging
DTI	diffusion tensor imaging
FA	fractional anisotropy
FLD	Fisher linear discriminant
FRO	Frobenius norm
HARDI	high angular resolution diffusion imaging
LLS	linear least squares
LPS	left-posterior-superior
MD	mean diffusivity
MRI	magnetic resonance imaging
ML	maximum likelihood
MVM	mild ventriculomegaly
NLS	nonlinear least squares
PCA	principal component analysis
PDF	probability density function
ROI	region of interest
sMRI	structural MRI
SNR	signal-to-noise ratio
WLS	weighted least squares

ACKNOWLEDGMENTS

As a graduate student, I have had the opportunity to work with a number of talented researchers and meet many lifelong friends. A move midway through my graduate studies from the University of North Carolina at Chapel Hill to the University of Utah initially seemed like a challenge, but the support of the faculty and students at both institutions has made the transition enjoyable and professionally rewarding. Thanks to my family for endless support throughout my many years as a student.

This document is due in large part to the tireless assistance and encouragement from my advisor Guido Gerig. I would also like to thank the rest of my committee Sarang Joshi, P. Thomas Fletcher, Edward Hsu, and Carl-Fredrik Westin who have all been both professional mentors and personal friends.

At the University of North Carolina, I am indebted to the faculty, staff and students of the medical image display and analysis group (MIDAG) especially the advice and guidance from Stephen M Pizer. I would also like thank Brad Davis, Remi Jean, Martin Styner, Clement Vachet, John Gilmore, Weili Lin, and Eli Broadhurst in particular for assistance in developing the research of this thesis.

The University of Utah and especially the scientific computing and imaging institute faculty, staff, and students have been very welcoming and accommodating in my transition here. I would like to thank Ross Whitaker, Ran Tao, and Sylvain Gouttard for helpful discussions. Also thanks to everyone in the third floor lab for making time at work enjoyable.

I would also like to thank the national alliance for medical image computing (NA-MIC) which provided both the funding for my studies under grant U54 EB005149 as well as a wealth of opportunities to improve my research and education. The interaction with the students, scientists, and engineers of the NA-MIC project

provided an education in medical image analysis that could not have been matched anywhere else.

CHAPTER 1

INTRODUCTION

1.1 Motivation

The development of medical imaging technology revolutionized the ability to safely investigate human anatomy. In particular, the invention of magnetic resonance imaging (MRI) has enabled noninvasive investigation of the central nervous system in living humans. Clinical evaluation of neurological disorder routinely acquires MRI of patients to diagnose damage to the nervous system from trauma, stroke, tumors, or other lesions, and modern psychiatric investigations routinely rely on imaging technology to probe the underlying biology of mental disorder. However, prior to the development of diffusion imaging, conventional MRI lacked the capacity to investigate the structure of the axon fiber bundles that comprise the brain white matter. Pioneering work in the 1980s by Le Bihan et al. enabled the acquisition of diffusion weighted imaging (DWI) with spatially varying measurements of the diffusion rate of water [60]. Basser et al. later introduced the diffusion tensor formalism to characterize the anisotropic diffusion found in white matter structures [9, 10]. The development of DWI and diffusion tensor imaging (DTI) has enabled detailed investigation of white matter fiber bundles by mapping the anisotropic diffusion of water generated by axon fiber bundles. However, for image analysis, diffusion imaging presents an added dimension of complexity over traditional imaging because of the multivariate, directional nature of the diffusion images. The development of new algorithms to process and analyze diffusion images, therefore, provides a unique opportunity to improve clinical understanding of brain white matter and to shed light on the biological basis of development and disease.

The human brain is a complex organ built from many interconnected processing

units. Tissue in the brain is often classified into white or grey matter based on function and anatomical structure. The grey matter of the brain comprises the processing circuitry of the nervous system, whereas the white matter consists primarily of bundles of axons that connect regions of the brain to each other as well as to peripheral motor and sensory neurons. These can be thought of analogous to a computer system consisting of processing units (grey matter) and wiring (white matter). Traditional structural MRI (sMRI) contrast produces images where the white matter appears as a homogeneous region. However, the microstructure of the white matter consists of a coherent structure of directionally organized axons separated into distinct fiber bundles. The development of DTI provides a new type of image contrast that allows the investigation of this microstructure by measuring macroscopically the molecular self-diffusion of water locally at each voxel of brain images. The underlying assumption in DTI is that diffusion of water molecules is restricted across fiber bundles but relatively unrestricted along fiber bundles. As a result, changes in tissue microstructure such as axon packing density, axon diameter, myelination, and other factors of tissue microstructure are reflected in directional diffusion measurements.

Scientific investigations trying to make inferences about white matter structure from DTI require sophisticated processing methods to translate the complex diffusion data into an anatomically relevant set of measurements. Computational methods are required to align populations of images, estimate tensors, compute fiber tractography, and perform statistical analysis. This thesis combines these techniques in a framework for investigating tract specific differences in diffusion properties between populations. The methods presented in this thesis draw inspiration from the field of brain mapping [101]. The field of brain mapping is concerned with transferring data from a population of brain images to a reference anatomy by spatial transformations of each image. This thesis provides an alternative computational framework for brain mapping and statistical analysis of DTI that provides several advantages for the analysis of specific tracts.

1.2 Overview of White Matter Anatomy

The central nervous system is the biological seat for cognitive thought, sensory information processing, homeostatic regulation, and control of motor function. The major components of the central nervous system are the spinal cord, the medulla, the midbrain and pons, the cerebellum, the thalamus, and the cerebrum or telencephalon. This thesis focuses on imaging and analysis of fiber tracts in the cerebrum. The cerebrum consists of two large hemispheres divided along the center by the central sulcus. Each hemisphere is a highly folded structure of neural tissue with the cortex comprising a few millimeters of the outside surface and containing most of the gray matter used for processing. The interior includes primarily white matter connections and subcortical structures such as the thalamus, the hypothalamus, the basal ganglia, the amygdala, and the hippocampus. The creases in the surface of the cortex are known as sulci and the folds of cortical tissue are gyri.

The fundamental cell of the nervous system is the neuron. As depicted in Fig. 1.1, the neuron consists of a cell body receiving signal through a set of dendrites and a long axon that connects via a synapse to other neurons. The presynaptic ending of the axon releases neurotransmitters that can excite or inhibit the postsynaptic neuron. Large collections of axons in the white matter of the brain make up the fiber bundles imaged using DTI. The bundles are often divided based on location and function into three categories: association, projection, and commissural.

Association fibers connect regions within the same hemisphere of the cerebral cortex. For example, neighboring gyri are often connected by short U-shaped fibers. The uncinate fasciculus connects the frontal lobe to the temporal lobe in each hemisphere. The arcuate fasciculus is another structure that connects Wernicke's and Broca's areas, which are responsible for speech production and comprehension, respectively. The cingulum and the fornix are two other major fiber bundles involved in the classic circuit of Papez. The circuit of Papez is a major component of the limbic system responsible for many activities including memory formation and learning. The cingulum connects regions of the cingulate cortex

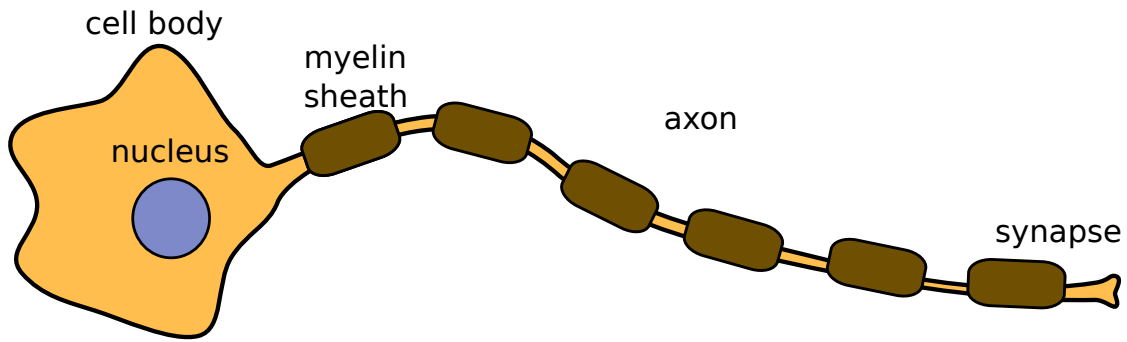


Figure 1.1. Diagram of a neuron. The neuron consists of a cell body with receiving dendrites and an axon that connects to another neuron. Large collection of axons formed in organized bundles known as fiber tracts make up the white matter of the nervous system.

to the hippocampus, and the fornix connects the hippocampus to the mamillary bodies.

Projection fibers are responsible for connecting the cortex to subcortical structures and the spinal cord. Sensory input and control of motor function for the body pass through the internal capsule tract. The internal capsule includes bidirectional connections between the thalamus and the cortex as well as bidirectional connections between the spinal cord and thalamus. The fiber tract connecting the postcentral gyrus, which is responsible for processing of sensory input, is referred to in this thesis as the sensory tract. The fiber tract connecting the precentral or motor gyrus to the spinal cord is referred to as the motor tract.

Commissural fibers are responsible for connecting the two hemispheres of the cerebrum. The corpus callosum is by far the largest commissural connection and is a large structure in the center of the midsagittal plane. The anterior region of the corpus callosum is often referred to as the genu, or bend, of the corpus callosum, whereas the posterior region is referred to as the splenium. Other smaller commissural connections include the anterior and posterior commissures. For further information on the anatomy of the nervous system, the reader is referred to Haines [45].

1.3 Application Areas

A wide variety of application areas in medicine and neuroscience exist for the methods presented in this thesis. These methods enable researchers to build a normative model of white matter diffusivity for fiber tracts and to use this model for statistical comparison. A significant number of neuroscience investigations into a variety of mental disorders already rely on DTI to investigate white matter changes. In this thesis, the primary clinical applications are the study of normal and abnormal development in children from birth to two years and the study of schizophrenia in adults. Additional applications using the methodology of this thesis are mentioned briefly in section 8.3.

1.3.1 Normal Development

The study of normal development presents an opportunity both to gain a better scientific understanding of the process of development as well to obtain a baseline of normal anatomy for the investigation of psychiatric disease. The rapid developmental changes in childhood are accompanied by significant development of the brain after birth. The brain increases in total volume after birth until about the age of 5 [29]. White matter structures increase in volume and develop well into early adulthood, while cortical gray matter regions undergo a period of growth followed by pruning in later adolescence [39]. MRI is an attractive tool for the investigation of development because of the minimal risk posed to healthy subjects. DTI, in particular, presents a safe method for investigating the myelination, development, and pruning of axon bundles during development.

MRI has so far proved to be a valuable tool for the investigation of normal development. Investigations so far have focused primarily on morphometric measures such as brain volume, cortical thickness, white and grey matter volumes, etc. However, the rapid change of tissue properties during development present major challenges for traditional morphometry studies based on segmentation. The quantitative nature of diffusion imaging may provide a more stable reference for many of these studies [47]. Furthermore, DTI elucidates additional features of tissue microstructure, especially in white matter. A majority of myelination occurs

before birth and during the first 2 years of life with some myelination occurring throughout life [29]. There has been substantial interest recently in acquiring large databases of pediatric DTI images [19]. Preliminary analysis of DTI statistics in pediatric subjects has illustrated the capacity of DTI to quantify biological changes due to development such as changes in myelination and axon packing. Gilmore et al. quantified differences in DTI images of neonates between fiber tracts to investigate differences in development rates [40]. In a review of DTI applied to pediatric imaging, Casicio et al. found consistent reports of increased anisotropy and decreased total diffusion due to development [22]. Bonekamp et al. found DTI measurements to be reproducible in pediatric studies [18]. Clinical studies such as these have so far required time-consuming manual region of interest (ROI) segmentation to identify regions for statistical analysis. This thesis provides an improved technology for efficient processing of large image databases that is both repeatable and reliable. DTI atlases built over different ranges of development serve to illustrate the development of white matter properties over time, and the construction of atlases from normal data provides a reference point for studying abnormal development.

1.3.2 Schizophrenia

In addition to the study of normal development, this thesis also examines differences between adults with schizophrenia and controls. Schizophrenia is a psychiatric disorder affecting approximately 1% of the world's population and accounts for a large percentage of public health resources [72]. Clinical symptoms of the disease include delusions, apathy, and auditory hallucinations [59]. There is some evidence that schizophrenia involves deficits in connectivity between different functional regions. Because of this hypothesis, recent studies have made extensive use of DTI in the investigation of schizophrenia to determine the location and extent of possible white matter differences between Schizophrenics and controls. Many studies have relied on voxelwise analysis methods such as statistical parametric mapping (SPM). For example, Burns et al. found reduced anisotropy in the left

uncinate and arcuate fasciculus in adult schizophrenics versus matched controls [20]. The advantage of this method of analysis is efficient processing requiring minimal manual intervention. However, the major drawback is that the statistical analysis can only test the relatively weak hypothesis of no differences between two populations that requires sophisticated multiple comparison correction and results in hard to interpret “blobs” of significance. Other groups have used manually drawn ROI to investigate specific hypotheses about differences between white matter anatomy. Kubicki et al. found anisotropy differences in the uncinate fasciculus with manual selection [58]. Although these methods are able to test more specific hypotheses, they suffer from time consuming manual segmentation. The methods presented in this thesis are useful tools for future research in schizophrenia, because they provide an automatic method to perform tract specific analysis of diffusion values.

1.3.3 Other Applications

Many other clinical neuroscience studies have acquired DTI, in addition to the areas of application focused on in this thesis. A significant number of studies have used DTI to investigate the anatomical root of the behavioral disconnects associated with autism. Alexander et al. showed that after controlling for age, IQ, and other factors, there are significant differences between diffusion measurements in the corpus callosum between subjects with autism and controls [1]. Barnea-Gorlay et al. observed decrease tensor anisotropy in white matter in a variety of areas including white matter deep to the ventromedial prefrontal cortex and the anterior cingulate gyrus [8]. Krabbe disease is a degenerative disease characterized by loss of axon myelination, and there is hope that DTI can be a useful tool for characterizing the progress of the disease as well as potential treatments [44]. Other disorders such as Alzheimers, drug addiction, alcoholism, etc. may involve deceits of white matter that can be investigated using DTI [99, 107, 62]. Although this thesis will not focus on any of these other application areas, the methods of this thesis are potentially valuable in any of these investigations.

1.4 Thesis and Contributions

Thesis: Populations of diffusion tensor images provide valuable insight into white matter tissue structure. Measurement error and image preprocessing steps must be controlled to minimize error in statistics. Computation of an anatomically relevant coordinate system through atlas building and fiber tract modeling provides an intuitive shape-based framework for understanding differences in white matter microstructure. The combination of preprocessing, atlas building, and tract analysis provides a robust framework for making inferences about white matter differences in populations.

This thesis describes the following developments in image analysis that contribute to the analysis of DTI:

1. An analysis of diffusion tensor estimation under different acquisition schemes illustrates the bias introduced by gradient sampling schemes with repeated directions.
2. An analysis of diffusion tensor estimation methods shows a preference towards weighted least squares tensor estimation to achieve efficient computation with reduced bias and variability of derived tensor measures.
3. A method for spatial normalization of tensor images based on unbiased atlas building allows populations of tensor images to be analyzed in a common coordinate frame.
4. Measures for evaluating geometric and functional differences in tractography are introduced and evaluated with specific application to validation of the spatial normalization.
5. A novel method for computing tract oriented statistics enables population comparison to account for multivariate tensor shape measures and along tract correlation.
6. The atlas building method is applied to cross-sectional data of normal development to understand the maturation of diffusion properties over time.

7. The tract oriented statistical method is applied to group analysis of pediatric and adult schizophrenia data.
8. The framework developed in this thesis is made available as an open source toolkit for the benefit of the scientific community.

1.5 Overview of Chapters

The following chapters of this thesis cover a background on DTI of human populations as well as present the contributions of this thesis for statistical analysis.

Chapter 2 presents a review of the use of DTI for the study of white matter anatomy. The imaging process and fundamental assumptions of DTI are reviewed. This chapter also provides a brief background on brain mapping, diffeomorphic image registration, and statistical analysis in neuroimaging.

Chapter 3 presents the contributions of this thesis in preprocessing of diffusion weighted images. Numerical simulation of the effects of diffusion weighting gradient design on measurements are presented and validated with experiments using real images.

Chapter 4 develops a method for the computation of a population atlas from diffusion images that includes invertible transformations between each image and a population mean.

Chapter 5 develops metrics for comparing fiber bundles generated from tractography and uses these methods to evaluate the spatial normalization method presented in Chapter 4.

Chapter 6 builds on the previous chapter by developing a novel statistical method for tract oriented analysis of diffusion properties.

Chapter 7 covers the application of the methods developed in this thesis to clinical problems including neurodevelopment and schizophrenia.

Chapter 8 reviews the contributions of the thesis, discusses limitations of the methodology, and presents potential areas of future research and development.

Appendix A presents a users manual for the software developed in conjunction with Chapter 4 of this thesis.

CHAPTER 2

BACKGROUND

2.1 Diffusion Weighted Magnetic Resonance Imaging

This section provides a mathematical background for measuring the diffusion of water using DWI and DTI and the application to evaluating white matter tissue properties.

2.1.1 Source of Diffusion Signal

MRI acquires images by applying powerful magnetic fields to tissue to align the nuclei of hydrogen atoms present in the water of the human body. In the presence of a strong magnetic field, these protons align their spins with the direction of the magnetic field. When a radio frequency (RF) pulse is used to knock the spins out of alignment, a corresponding RF signal is generated as the spins recover. Traditionally, structural MRI has focused on measuring two constants of this recovery, T_1 and T_2 , as a mechanism for providing tissue contrast. Diffusion imaging relies on the use of two gradient pulses to dephase and then rephase protons within a voxel. The self-diffusion of water along the direction of gradient pulses causes protons to experience varying field strengths during the two pulses as a result of diffusion. As a result, the phases of protons do not completely refocus after application of the second gradient resulting in signal attenuation. The modeling equation is the Stejskal-Tanner equation

$$S_i = S_0 \exp(-bg_i \mathbf{D} g_i^T), \quad (2.1)$$

where S_i is the observed intensity in a gradient direction g_i , S_0 is the intensity without diffusion weighting, and b is a constant proposed by Le-Bihan [97, 60]. b is defined as

$$b = \gamma^2 G^2 \delta^2 \left(\Delta - \frac{\delta}{3} \right), \quad (2.2)$$

where γ is the gyromagnetic ratio, G is the amplitude of the diffusion weighting gradient, δ is the duration of the gradient, and $\Delta - \delta$ is the time between the end of one gradient pulse and start of the next pulse [67]. (2.1) provides the fundamental mechanism for measuring the diffusion of water in a particular direction. The value $g_i \mathbf{D} g_i^T$ is the measured diffusion in direction g_i for a voxel and is referred to as the apparent diffusion coefficient (ADC).

2.1.2 Diffusion Tensor Model

In materials with isotropic diffusion such as free water, the diffusion of water measured in any direction is the same. However, in brain white matter the presence of biological tissue such as axons hinders the diffusion of water. The structure of axon bundles creates an anisotropic limitation on the diffusion of water based on the orientation of fiber bundles within the tissue. Figure 2.1 shows an example of a tissue arrangement that generates diffusion anisotropy compared with another that produces more isotropic diffusion. If the orientation of the fiber direction was known prior to the imaging experiment, the anisotropy could be measured by 1 ADC measurement along the fiber orientation and 1 measurement perpendicular to the orientation. However, the fiber orientation of brain white matter varies over the image and is not known prior to imaging.

To solve this problem, the diffusion tensor model was introduced [9]. In this model, diffusion is approximated as a single Gaussian distribution for each voxel with probability density function (PDF)

$$p(x|x_o, \tau) = \frac{1}{(2\pi)^{3/2} |D(\tau)|^{1/2}} \exp \left(-\frac{(x - x_o)^T D(\tau)^{-1} (x - x_o)}{2} \right). \quad (2.3)$$

This gives the probability that a particle originally located at point x_0 is at point x after time τ . The covariance is assumed to depend on the time τ as restrictive interfaces for the diffusion are more likely to affect the diffusion at larger τ . That is, at low τ D is typically closer to isotropic. D is measured by the log ratio of nondiffusion weighted signal to diffusion weighted signal following (2.1) in at least

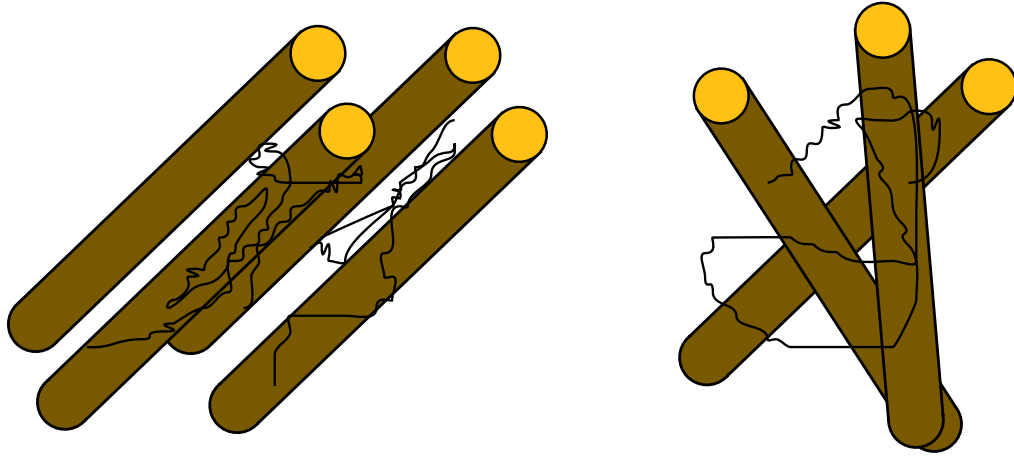


Figure 2.1. The random walk of water molecules within anisotropic tissue such as an axon fiber bundle tends to travel more easily along the fiber bundle.

six linearly independent directions. The diffusion tensor D is a covariance matrix and is therefore symmetric positive-definite. Further details on the estimation of the diffusion tensor from observed signals will be covered in Chapter 3.

2.1.3 Higher Order Models

Although the tensor model of diffusion has proven useful in clinical studies, there are several well-known deficiencies associated with the tensor model. The primary deficit is the inability of the tensor model to deal with fiber crossings or other complex fiber architectures. An illustration of this problem is shown in Fig. 2.2, where crossing fibers reduce the anisotropy of the measured tensor. This problem was initially identified by Tuch et al. who showed that multiple fiber orientations per voxel could be resolved using high b-values and increase angular sampling [103]. The problem arises from multiple compartments of tissue within the relatively large spatial size of a voxel.

Higher order distributions have been a recent area of research interest for instances where the microstructure of a voxel is substantially heterogeneous. Preliminary work on q -space MRI showed that more complex measurements could be made but were clinically unfeasible at the time [11]. A variety of different models have been proposed to overcome the limitation of DTI including higher order diffusion

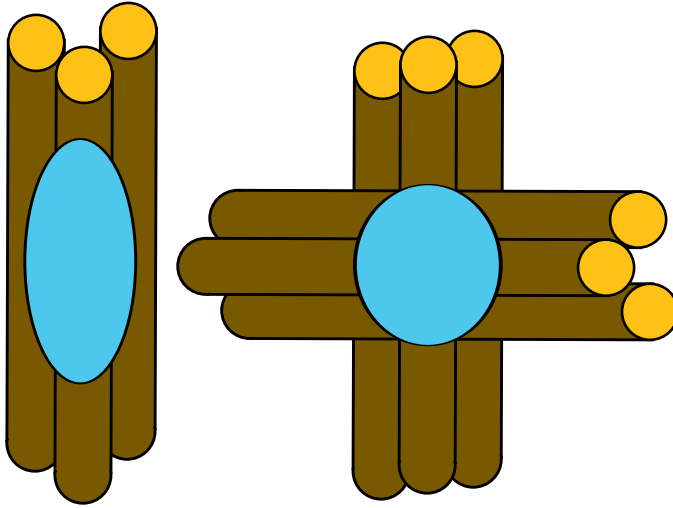


Figure 2.2. Example of noncrossing and crossing fibers.

tensors [77, 78], q-ball imaging [102], spherical harmonics [27], and mixtures of tensors [80, 56]. However, high angular resolution diffusion imaging (HARDI) imaging techniques are not yet widely used in clinical neuroscience studies. Given the focus of this thesis on population studies, the following chapters will focus primarily on the single tensor model. Chapter 8 gives a brief discussion on future work that could extend the methods of this thesis to more complex diffusion models.

2.1.4 Scalar Invariants

The analysis methods presented in this thesis rely on the ability of DTI to provide quantitative information about tissue microstructure. Several scalar quantities have been proposed to summarize information about tissue microstructure from the diffusion tensor. Because the diffusion tensor, \mathbf{D} , is symmetric positive-definite, the spectral decomposition theorem ensures that there exists

$$\mathbf{D} = \mathbf{V}\mathbf{\Lambda}\mathbf{V}^T, \quad (2.4)$$

where V has as columns the eigenvectors $\{\hat{\mathbf{e}}_1, \hat{\mathbf{e}}_2, \hat{\mathbf{e}}_3\}$ and $\mathbf{\Lambda}$ are the corresponding eigenvalues $\{\lambda_1, \lambda_2, \lambda_3\}$. If $\lambda_1 \gg \lambda_2, \lambda_3$, then the hypothesis is that $\hat{\mathbf{e}}_1$ points in the same direction as the underlying fiber bundle. The eigenvalues of the tensor are rotationally invariant. That is, they are the same when measuring arbitrary

rotations of the tensor. As the orientation of the tissue structures is not known prior to the experiment, only scalar measures that are invariant to rotation are considered here. For this reason, measures will be expressed in terms of both the tensor elements and eigenvalues. This section will cover invariant measures to evaluate the anisotropy and size of diffusion tensors.

Initial ADC diffusion measurements were made by MRI in a small, two or three, number of directions. Rotationally invariant measures were initially proposed as part of the diffusion tensor model by Basser and Pierpaoli to avoid error introduced by the choice of laboratory reference frame when using a small number of measurement directions [10, 83]. Some of the initially proposed measures include fractional anisotropy (FA), mean diffusivity (MD), relative anisotropy (RA), the lattice index (LI), and the organization index. The purpose of these measures is to produce a contrast for MRI that reflects the biological tissue invariant to changes in the laboratory coordinate frame. Because these measures are rotationally invariant, they can be expressed in terms of the eigenvalues of the diffusion tensor. For computational efficiency, many are implemented in terms of the tensor elements to avoid diagonalizing the tensor matrix.

By far the most commonly used measures in the published literature are the FA and MD. FA is a dimensionless quantity bounded between $0 \leq FA \leq 1$. Tensors with high FA are elongated in 1 dimension and narrow in the other dimensions. Tensors with low FA are close to spherical. FA is defined as

$$FA = \frac{\sqrt{3}}{\sqrt{2}} \frac{|\mathbf{D} - \frac{1}{3}\text{trace}(\mathbf{D})\mathbf{I}|}{|\mathbf{D}|} \quad (2.5)$$

$$FA = \frac{1}{\sqrt{2}} \frac{\sqrt{(\lambda_1 - \lambda_2)^2 + (\lambda_1 - \lambda_3)^2 + (\lambda_2 - \lambda_3)^2}}{\sqrt{\lambda_1^2 + \lambda_2^2 + \lambda_3^2}}. \quad (2.6)$$

Mean diffusivity is the average ADC over all directions and can be expressed as

$$MD = \text{trace}(\mathbf{D})/3 \quad (2.7)$$

$$MD = (\lambda_1 + \lambda_2 + \lambda_3)/3. \quad (2.8)$$

A related size measure is the trace of the tensor, $tr(D)$, which is equal to $3MD$. MD is expressed in physical diffusion units of mm^2/s . Another metric of tensor

size which will be used in this thesis is the Frobenius norm (FRO) of the diffusion tensor,

$$\|D\|_F = \sqrt{\sum_{i=1}^3 \sum_{j=1}^3 D_{ij}^2} \quad (2.9)$$

$$\|D\|_F = \sqrt{\lambda_1^2 + \lambda_2^2 + \lambda_3^2}. \quad (2.10)$$

Another pair of measures include the axial and radial diffusivity λ_{\perp} and λ_{\parallel} ,

$$\lambda_{\perp} = \lambda_1 \quad (2.11)$$

$$\lambda_{\parallel} = \frac{\lambda_1 + \lambda_2}{2}. \quad (2.12)$$

Axial and radial diffusivity are expressed in physical units of mm^2/s . The definition of additional invariant measures not used in this thesis can be found in [10, 83, 108].

Although the true relationship between these invariant measures and the underlying tissue properties remains unknown, there have been several important findings that give credibility to the use of these measures as biomarkers for tissue change. Early results in developing anisotropy measures showed these measures were typically high in white matter regions in cat and primate animal models as well as humans [83]. Investigation of Krabbe disease using the RA showed a strong correlation with known deficits in myelination in patients with the disease and was shown to be more sensitive than standard T2 imaging [44]. Experiments in diffusion imaging of the developing mouse brain showed a correlation between anisotropy and development of brain tissue [70]. Song et al. showed that mice with a genetic deficiency in myelin production with no additional axonal damage displayed higher values for λ_{\perp} than matched controls that would also correspond to lower FA and higher MD [96]. This study gives credibility to the use of anisotropy as a biomarker for changes in tissue myelination. In a related field to material presented later in this thesis, a negative correlation of MD with age and a positive correlation of FA with age has been shown in healthy developing adolescents [88]. These findings are unable to demonstrate the specificity of DTI invariant changes with biological causes. They do, however, provide credibility for the use of DTI as a biomarker for tissue change.

2.1.5 Fiber Tractography

Segmenting anatomically known fiber bundles remains an important challenge for DTI analysis. The most common approach, fiber tractography, integrates the field of tensor principal eigenvectors to create streamlines that sample anatomical fiber bundles [14]. The fiber tractography algorithm used in this thesis is a relatively simple streamline method based on 4th order Runge-Kutta integration. In this algorithm, a seed region is defined manually. Within the seed region, a streamline is initialized at each voxel center and propagated by following the principal eigenvector of the tensor using a fixed step size. Tensors are interpolated using linear interpolation of the tensor elements. Eigenvector sign is disambiguated by ensuring that the inner product of the previous direction with the current eigenvector is positive. An example tracing of a streamline through a fiber bundles is shown in Fig. 2.3. Tracts are terminated when they reach a region of low FA, typically around 0.2. A second ROI is typically also specified and only streamlines that pass through both are retained. The goal of the tractography algorithm used in this thesis is to select a reasonable geometry for the analysis of diffusion statistics and is not intended to determine if two brain regions are connected.

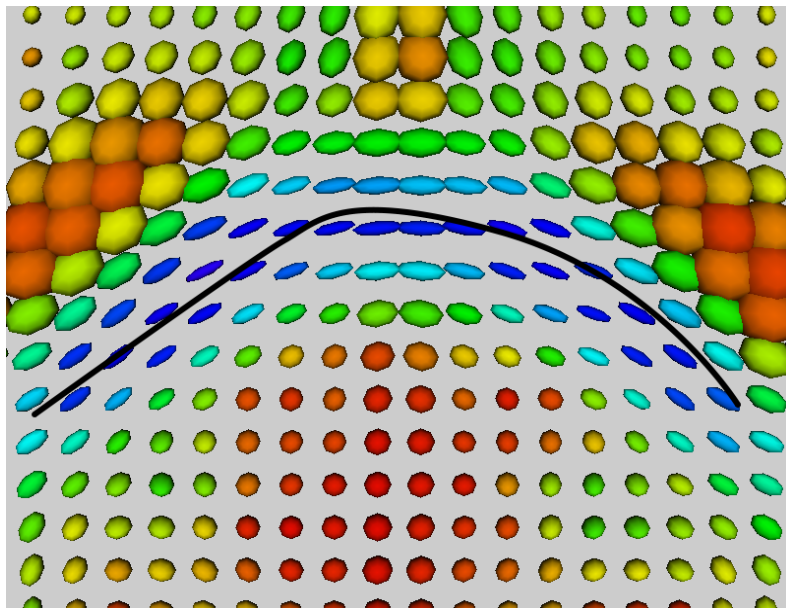


Figure 2.3. Single streamline trace through a tensor field.

Additional research has been reported by groups working on explicit volumetric segmentation of white matter tracts. Several groups have proposed distance metrics between tensors to enable levelset segmentation of white matter fiber tracts [106, 61]. Nonparametric methods for calculating the distribution of diffusion has been applied to enable segmentation of difficult structures such as the cingulum [7]. Other research has used Finsler metrics to enable optimization of paths through a tensor field [68, 69]. A similar approach using a geodesic distance between points in an image is used to identify volumetric fiber bundles [35]. These methods provide more explicit segmentation of the volume of white matter fiber bundles. The focus of this thesis is statistical analysis of diffusion properties parametrized fiber bundles. Therefore, this thesis will rely on streamline tractography methods.

The tractography algorithm used in this thesis is deterministic. To obtain better connectivity measures from DTI probabilistic tractography has been proposed to evaluate the connectivity between two regions of the brain. Friman et al. proposed a Bayesian approach for dealing with local uncertainty in fiber orientation to obtain a global measure of connectivity [36]. Later work by Zhang et al. developed a fast and efficient sampling method to solve this connectivity problem using a particle filter [113]. Both of these models are able to integrate information over the tract to overcome local ambiguity in the orientation of fiber bundles due to noise.

2.2 Statistical Analysis of DTI

Most approaches to group analysis in the clinical DTI literature have relied on voxel-based analysis or manually drawn ROI. An overview of the differences between voxel-based and ROI analysis in DTI population studies was described by Snook et al [95]. ROI analysis typically uses manual segmentation of white matter structures. Within the ROIs, diffusion properties such as FA or MD are averaged to create a single statistic. Examples of studies using ROI methods can be found in normal development [18, 40, 47], schizophrenia [57], and Krabbe’s disease [44]. The major drawback of ROI analysis is the time consuming and unreliable manual identification of regions, especially the challenge to identify the long, curved structures

common in DTI fiber tracts. Furthermore, reliability is reduced by the interrater and intrarater variability introduced by manual segmentation. This thesis improves on previous methods in the ability to perform automatic processing through the use of high-dimensional deformable registration as well as the ability to focus on testing specific hypotheses regarding tracts of interest using a novel method for joint analysis of multivariate tensor measures in a tract model.

Voxel-based analysis methods are characterized by alignment of images to a template followed by independent hypothesis tests per voxel that are typically smoothed and corrected for multiple comparisons. The most popular frameworks for voxelwise analysis are the statistical parametric mapping (SPM) and FMRIB software library (FSL) [37, 94]. Voxelwise analysis has been applied in DTI studies including autism [8] and schizophrenia [20]. The major challenge in voxel-based analysis is the need for multiple comparison correction and smoothing that can make localization of changes challenging to interpret [51].

One of the most popular frameworks for statistical analysis of DTI is the tract-based spatial statistics (TBSS) software [93]. TBSS is a modified voxelwise approach for analysis of diffusion properties using nonlinear registration to a template combined with a skeletonization of FA voxels. FA values are globally projected onto the skeleton followed by pointwise hypothesis tests on the skeleton. This method improves the localization of voxelwise approaches for DTI by projecting diffusion invariants on a white matter surface. However, this approach lacks a method for performing analysis of specific tracts. Furthermore the use of local rather than global hypothesis tests limits the ability to account for along tract correlation of diffusion values.

Tract oriented analysis has been proposed as a mechanism for understanding the diffusion statistics of white matter tracts in the context of the anatomy as extracted by fiber tractography. Jones et al. created the pointwise assessment of streamline tractography attributes (PASTA) tool, a graphical tool for visualizing diffusion statistics of a fiber bundle [52]. Lin et al. used a length normalized framework for investigating diffusion statistics in the pyramidal tract [63]. Corouge et al. proposed

to analyze tensors as a function sampled along arc length of fiber bundles using appropriate statistics for the space of diffusion tensors [23]. These methods will be extended in this thesis with the development of methods normalizing measures in a population and a novel statistical framework for populations of arc length functions.

In work closely related to the proposed methodology, [112] propose a method for statistical analysis along the two-dimensional medial manifolds of fiber tracts for specific tracts of interest after unbiased group alignment. On the tract medial axis, permutation tests are applied to detect clusters of pointwise differences between MD of groups. This method has the advantage of modeling structures using a medial sheet rather than an arc length function as will be used in this thesis. However, this flexibility in geometric modeling comes at the price of increased data dimensionality. The global method for tract analysis discussed in Chapter 6 of this thesis cannot be easily applied to functional data parametrized by 2 variables. For those tracts that can be adequately modeled as a single parameter function, uncinate, fornix, cingulum, etc., this thesis provides a statistical mechanism more appropriate for addressing global changes in tract statistics.

O'Donnell and Westin used clustering to obtain a consistent set of fiber tracts across a population [75]. Further work used the population of fiber tracts to perform pointwise statistics along tract functions [76]. An alternative framework by Maddah et al. performs joint clustering and point matching of fiber bundles [64]. This framework has been applied to a study of schizophrenia in adults [65].

CHAPTER 3

DIFFUSION WEIGHTED IMAGE PREPROCESSING

3.1 Introduction

Clinical neuroimaging studies that acquire DTI commonly rely on derived tensor measures such as FA or MD for statistical analysis. Most studies in the literature employ voxelwise or ROI analysis of derived measures, although some studies have begun to use tract specific analysis [40]. In any of these methods, the precision and accuracy of diffusion measurements must be well understood to understand the limits and power of statistical analysis. DTI is particularly sensitive to errors introduced by imaging noise for three major reasons. First, since multiple diffusion weighted images are needed, each individual image must be acquired relatively quickly, reducing the signal-to-noise ratio (SNR) for each image. Second, unlike structural MRI, where intensities are primarily used to establish contrast between tissue types, DTI measures quantitative physical properties requiring a more careful evaluation of noise. Finally, many of the interesting features of the image such as the FA are nonlinear transformations of the original images and consequently need to be analyzed carefully to understand the impact of imaging noise. In this chapter, simulation of the influence of Rician noise on tensor derived measures is presented along with an evaluation of the simulation against *in-vivo* experiments.

Since the introduction of DTI, many studies have investigated the effects of noise on tensor measurements through theory and Monte Carlo simulation. Early on, Bastin et al. showed the effect of imaging noise and SNR on estimation of FA using Monte Carlo simulation [15]. Skare et al. later extended this work to show a comparison of the effect of noise on different anisotropy measures [92]. Basser and Pajevic illustrated some of the nonlinearities in diffusion tensor statistics

by demonstrating the sorting bias associated with estimating the value of the eigenvalues of diffusion tensors [12]. Anderson presented a theoretical framework for investigating the effects of noise and developed some preliminary results on the implications for fiber tractography [4]. Hasan compared different gradient encoding schemes for DTI by developing metrics on the geometry of diffusion weighting gradients [46]. Mangin et al. combine distortion correction and tensor estimation to reduce motion artifacts in tensor statistics [66]. Derek Jones elaborated on the previous investigations by simulating the effect of noise under a variety of gradient directions [49]. Further investigation of the impact of imaging noise on fiber tractography was developed by Basser and Pajevic [13]. Jones and Basser showed how Rician noise tends to underestimate high values of the ADC along gradient directions [50]. Koay et al. describe methods to overcome negative eigenvalues in tensor estimation caused by imaging noise [55]. Basu et al. used the Rician noise model to demonstrate statistical bias and develop a regularization filter for diffusion weighted images [16]. Fillard et al. combined a maximum likelihood (ML) tensor estimator with a regularization function to jointly smooth and estimate a tensor field [31, 32].

This chapter builds on previous work by combining a comparison of gradient direction schemes with tensor estimation methods to study the error in diffusion tensors given the noisy image acquisition typical in a clinical framework. This chapter assumes the use of a single diffusion tensor model per voxel and does not consider high angular resolution diffusion imaging (HARDI). The simulations in this chapter show that increasing the number of gradient directions reduces the bias introduced by sparse sampling of highly anisotropic tensors. Furthermore, experiments demonstrate the increased variability caused by linear least squares estimation on sequences with many gradient directions. Finally a novel *in-vivo* experiment validates the predictions of the simulation.

3.2 Methods

The estimated diffusion in a direction \mathbf{g} can be understood as a function of observed diffusion weighted MR intensities via the Stejskal-Tanner equation

$$S_i = S_0 \exp(-b\mathbf{g}_i\mathbf{D}\mathbf{g}_i^T). \quad (3.1)$$

Magnetic resonance images are acquired by computing the Fourier transform of a measured k-space signal. Noisy k-space measurements are converted into a complex spatial image via the inverse Fourier transform. The complex spatial image is converted to a real image by taking the magnitude at every voxel. Pure thermal noise in both the real and imaginary components of k-space is well-approximated by a Gaussian distribution, and noise in the magnitude signal S_i is consequently well-characterized by a Rician distribution [91, 90]. A noisy measurement R of an underlying signal A in the diffusion weighted image is a random variable given by

$$R = \sqrt{(A + X)^2 + (Yi)^2}, \quad X, Y \sim N(0, \sigma^2), \quad (3.2)$$

where X and Y are Gaussian random variables. The PDF for a Rician random variable R with true intensity A and noise variance σ^2 is

$$f(x|A, \sigma) = \frac{x}{\sigma^2} \exp\left(-\frac{x^2 + A^2}{2\sigma^2}\right) I_0\left(\frac{xA}{\sigma^2}\right), \quad (3.3)$$

where I_0 is the zero-order modified Bessel function of the first kind. By substituting $A = 0$ into (3.3), the PDF reduces to that of a Raleigh distribution,

$$f(x|\sigma) = \frac{x}{\sigma^2} \exp\left(-\frac{x^2}{2\sigma^2}\right), \quad (3.4)$$

which is assumed to be the distribution of background voxels in an image. When A is much larger than σ , (3.3) converges to a Gaussian distribution. The consequence of these two limits is that low intensity voxels have a positive measurement bias, $E[R] > A$, whereas high intensity values are relatively unbiased. A geometric interpretation of Gaussian noise in the complex plane can be seen in Fig. 3.1, where low magnitude signals appear biased because more mass of the measurement PDF falls outside circles of equivalent magnitude.

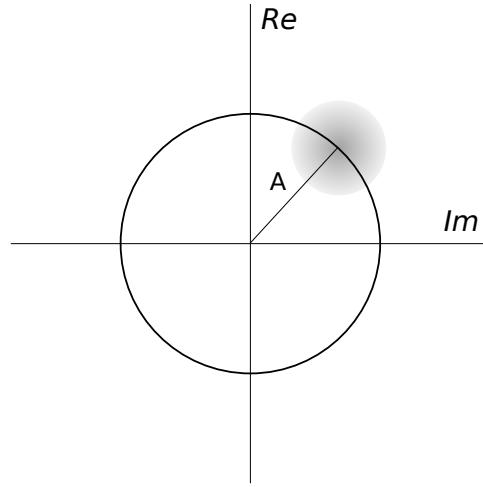


Figure 3.1. Geometric interpretation of Rician noise. All values in concentric circles about the origin have the same magnitude in the final image. For small circles, magnitudes, the mass of the measurement distribution is greater outside the circle than inside.

The ADC in a direction \mathbf{g}_i is measured in a voxel by the log of the ratio of a baseline signal S_0 and an attenuated diffusion weighted signal S_i . Because diffusion weighted measures have low intensity, they are likely to be positively biased. Overestimation of a diffusion weighted intensity S_i causes an underestimation of diffusion in the direction g_i because of the exponential decay in the Stejskal-Tanner equation (3.1). Measurements of low diffusion have lower attenuation and correspondingly less bias. The tendency to underestimate high ADC values causes two major challenges for reliable measurements in DTI. First, MD is likely to be underestimated for regions with high diffusion. This is a particular problem in the cerebrospinal fluid (CSF), where the ADC is high in all directions. Secondly, anisotropy can be underestimated depending on the alignment of the principal diffusion direction of a highly anisotropic tensor with the gradient directions. The maximum measured ADC of a highly anisotropic tensor depends on the gradient direction sampling. Although a noiseless measurement of the tensors in Fig. 3.2 would produce identical results, the tensor shown in Fig. 3.2(a) is more likely to be biased because of the large ADC measurement of the gradient direction aligned with the principal eigenvector.

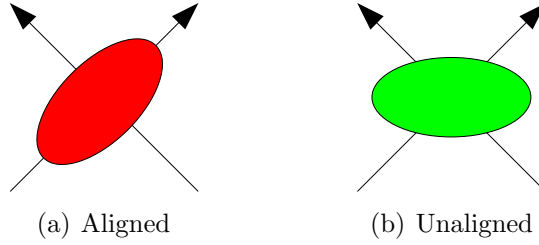


Figure 3.2. Example of tensors with principal eigenvectors aligned or unaligned with a gradient direction.

The relevant tissue parameters for each voxel in the image are the six unique components of the diffusion tensor along with the baseline T_2 intensity S_0 that will be formed into the 7 element vector $\boldsymbol{\beta}$. Specifically, the elements of $\boldsymbol{\beta}$ are defined as

$$\mathbf{D} = \begin{pmatrix} \beta_0 & \beta_1 & \beta_2 \\ \beta_1 & \beta_3 & \beta_4 \\ \beta_2 & \beta_4 & \beta_5 \end{pmatrix}, \quad \log S_0 = \beta_6. \quad (3.5)$$

Assuming there are N gradient directions with unit vector \mathbf{g}_i and b-value b_i , then the matrix \mathbf{X} , which is $N \times 7$, can be used to express the relationship between the vector $\boldsymbol{\beta}$ and the observed signals \mathbf{S} :

$$\mathbf{X} = - \begin{pmatrix} b_1 g_{0x}^2 & 2b_1 g_{0x} g_{0y} & 2b_1 g_{0x} g_{0z} & b_1 g_{0y}^2 & 2b_1 g_{0y} g_{0z} & b_1 g_{0z}^2 & 1 \\ \vdots & \vdots & \vdots & \vdots & \vdots & \vdots & 1 \\ b_N g_{Nx}^2 & 2b_N g_{Nx} g_{Ny} & 2b_N g_{Nx} g_{Nz} & b_N g_{Ny}^2 & 2b_N g_{Ny} g_{Nz} & b_N g_{Nz}^2 & 1 \end{pmatrix}. \quad (3.6)$$

Using the definition of \mathbf{X} in (3.6), the Stejskal-Tanner equation, (3.1), can be reformulated as

$$\mathbf{S} = \exp(\mathbf{X}\boldsymbol{\beta}). \quad (3.7)$$

A minimum of seven gradient images with at least two different b-values are required to have a fully determined system for the parameters of the diffusion tensor. Because diffusion weighted images typically have low SNR, acquiring more images than the minimum seven is desirable to improve SNR and obtain more robust measures of the diffusion parameters. Imaging protocols in clinical use commonly employ repetitions of gradient directions and are typically processed by averaging of repetitions on the scanner using a number of excitations (NEX) setting greater

than 1, or the repeated images are processed offline where corresponding images are registered and averaged. Alternatively, many studies acquire additional diffusion weighted images using more unique gradient directions, and the additional observations are combined in the tensor estimation. In images with multiple repetitions of the same gradient direction, the signals are typically averaged. However, the mean of the signals is a poor estimator of the true signal A , because of the bias in the Rician distribution. Averaging of magnitude values tends to overestimate the signal, which leads to underestimation of high ADC values. Retrospective analysis of data with repeated directions could employ ML estimation of Rician distributed measurements or incorporate the measurements into an appropriate tensor estimation routine.

For gradient schemes with more than the minimal number of gradient directions, several methods exist in the literature for estimating diffusion tensors from the diffusion weighted images. For the following investigation, these methods have been implemented in both MATLAB and c++ using the insight toolkit (ITK). The most common approach has been a linear least squares (LLS) estimator for the tensor parameters $\boldsymbol{\beta}$ from the log of the observed signal intensities \mathbf{S} with baseline signal S_0 [108].

$$\hat{\boldsymbol{\beta}}_{\text{lls}} = (\mathbf{X}^T \mathbf{X})^{-1} \mathbf{X}^T (\ln \mathbf{S}). \quad (3.8)$$

The matrix \mathbf{X} , which is $N \times 7$, was described in (3.6). To avoid the reweighting penalties associated with the logarithm, nonlinear least squares (NLS) estimation numerically optimizes the objective function

$$f_{\text{nls}}(\boldsymbol{\beta}) = \|\mathbf{S} - \exp(\mathbf{X}\boldsymbol{\beta})\|^2 \quad (3.9)$$

on the diffusion weighted signal. For efficient optimization of sum of squares functions such as (3.9), Levenberg-Marquardt optimization is employed. The optimizer is initialized using the LLS solution. Salvador et al. proposed a weighted least squares (WLS) estimator

$$\hat{\boldsymbol{\beta}}_{\text{wls}} = (\mathbf{X}^T \mathbf{W}^2 \mathbf{X})^{-1} (\mathbf{X}^T \mathbf{W}^2 (\ln \mathbf{S})) \quad (3.10)$$

$$\mathbf{W} = \text{Diag}(\mathbf{X} \hat{\boldsymbol{\beta}}_{\text{lls}}) \quad (3.11)$$

based on an analysis of the log Rician probability distribution [87]. The implementation used in this work uses one iteration of weight computation.

An ML estimate of the diffusion tensor using the log-likelihood function of the Rician distribution was proposed by Fillard et al. [31]. Here, a similar method does not use a spatial regularization term or the log of the tensor matrix. The spatial regularization term is avoided to provide the best estimate for each voxel independently. The ML method explicitly accounts for the noise model and uses an estimate of the noise level computed from the background of the image. The ML estimation of tensor parameters is obtained by numerical optimization of the log-likelihood function

$$\log L(\boldsymbol{\beta}) = \sum_i \log \left(\frac{S_i}{\sigma^2} \right) - \frac{S_i^2 + S_0^2 e^{2X_i \boldsymbol{\beta}}}{2\sigma^2} + \log \left(I_0 \left(\frac{S_i S_0 e^{2X_i \boldsymbol{\beta}}}{\sigma^2} \right) \right), \quad (3.12)$$

where X_i is a row of the matrix \mathbf{X} and N is the number of gradient directions. Our implementation uses a gradient descent optimizer to maximize the objective function. The analytical derivative of the log-likelihood function (3.12) is

$$\nabla \ln L(\boldsymbol{\beta}) = \sum_{i=1}^N -\frac{S_0^2 X_i}{\sigma^2} e^{2X_i \boldsymbol{\beta}} + \frac{X_i e^{X_i \boldsymbol{\beta}} S_0 S_i}{\sigma^2} I_1 \left(\frac{S_i S_0 e^{X_i \boldsymbol{\beta}}}{\sigma^2} \right) / I_0 \left(\frac{S_i S_0 e^{X_i \boldsymbol{\beta}}}{\sigma^2} \right).$$

The following section presents an evaluation of the different tensor estimation methods across several different gradient sampling schemes using a Monte Carlo framework for simulating the effect of imaging noise on derived properties.

3.3 ML Estimation of Rician Parameters

ML estimation of the true intensity A from a set of Rician distributed samples was compared to averaging the observed samples. ML estimation is optimal in the asymptotic limit, but clinically applicable studies do not have the capability to acquire unlimited repetitions, so a comparison of ML estimation to standard averaging at expected noise levels and sample sizes is necessary. Four different signal levels were simulated, and the ML estimator is substantially less biased, as shown in Fig. 3.3. This result demonstrates the bias that can be introduced by averaging repeated images to improve SNR in image acquisition, and the improvement by

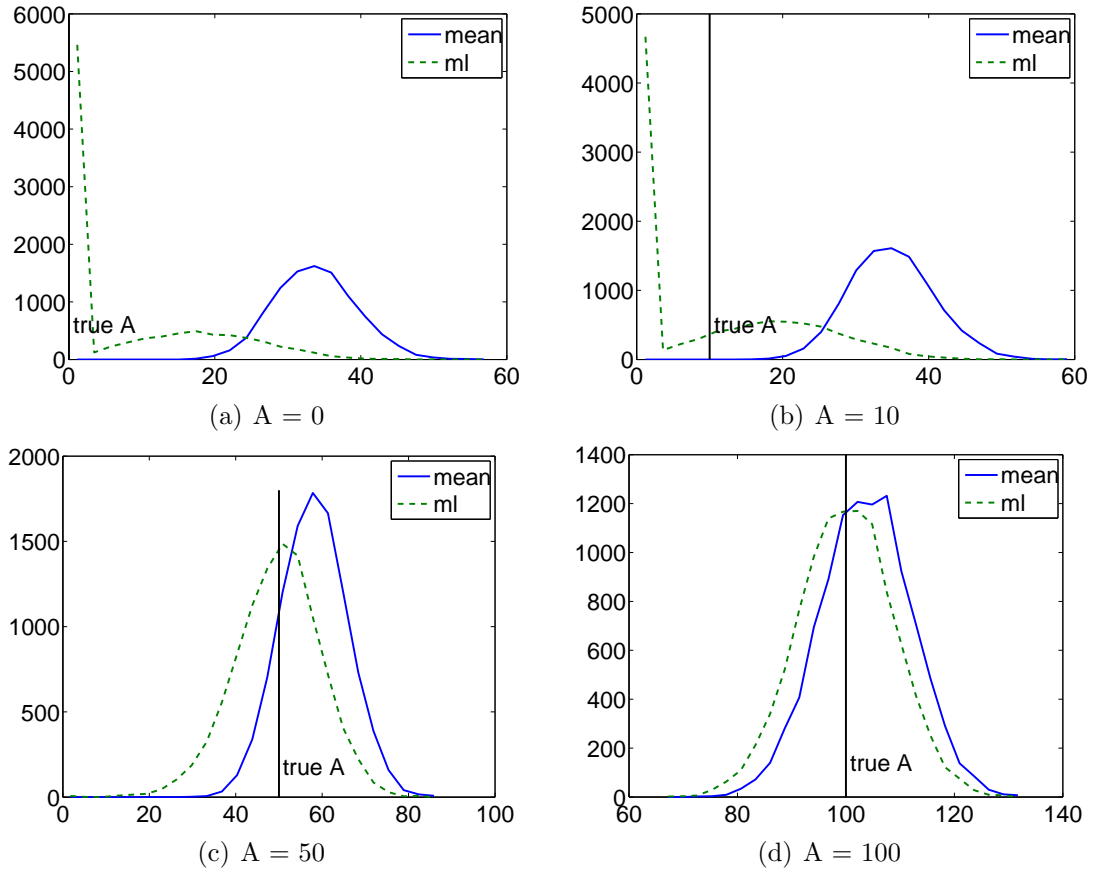


Figure 3.3. Simulated comparison of ML estimation (dashed line) and averaging (solid line) of DWI intensity. Shown above are histograms of Monte-Carlo simulation at four intensity levels (a) 0 (b) 10 (c) 50 (d) 100. The sigma used, $\sigma = 27$, was experimentally determined from test data. Ten samples of the intensities were used in the estimators, and 5,000 repetitions were performed. The ML estimator is less biased at signal levels that commonly occur in real images.

using ML estimation of intensities for retrospective analysis. The primary drawback of the ML method is the singularity that occurs when the intensity is very close to zero. At very low signal levels, quantization artifacts coupled with numeric instability make it difficult to obtain an estimator that does not converge to zero. This instability indicates that careful selection of b-values is important to ensure that the diffusion weighted signal is not completely attenuated.

3.4 Simulation of Tensor Estimation

A framework for Monte Carlo simulation was implemented in MATLAB to compute the distribution of estimated tensors from the predicted signal of a given true tensor with added Rician noise. The true tensor in all simulations had a fixed trace of $2.1 \times 10^{-3} mm^2/s$, which is a typical value for white matter. Several levels of anisotropy and orientation were simulated. The simulations used a b-value of $1000 s/mm^2$, a noise level of $\sigma = 27$ estimated experimentally from the background of an image acquired on a clinically used scanner, and a baseline signal of 250. Three different gradient direction schemes were employed and are referred to using the following abbreviations:

6x10 6 gradient directions with 10 repeated measurements for each direction

21x3 21 gradient directions with 3 repeated measurements along for each direction

60x1 60 gradient directions with 1 measurement for each direction

A complete list of the gradient directions is given in appendix B.

The simulation experiments show that the positive bias of Rician noise at low signal level can lead to underestimation of FA and trace. Furthermore, the orientation of the tensor within the gradient fields correlates with the bias, and statistical comparison of structures with different fiber orientations is, therefore, potentially biased. Many common clinical gradient schemes use the minimal six gradient directions and with these schemes, the expected bias depends on the orientation of the fiber structure with respect to the gradient direction sampling. Figure 3.4 shows the bias and variability of the FA and trace of a fixed diffusion tensor as the tensor rotates in space relative to a gradient direction. The simulations show that estimated FA is substantially correlated with orientation. The trace estimate has less bias due to orientation, but the trace is underestimated in gradient schemes with repeated directions.

Figures 3.5, 3.6, and 3.7 show the simulated distribution of the Frobenius norm of the difference between the estimated and true tensor, MD, and FA, using a 60 direction protocol. Weighted least squares and maximum likelihood perform similarly, whereas linear least squares has more variability. Nonlinear least squares tends to

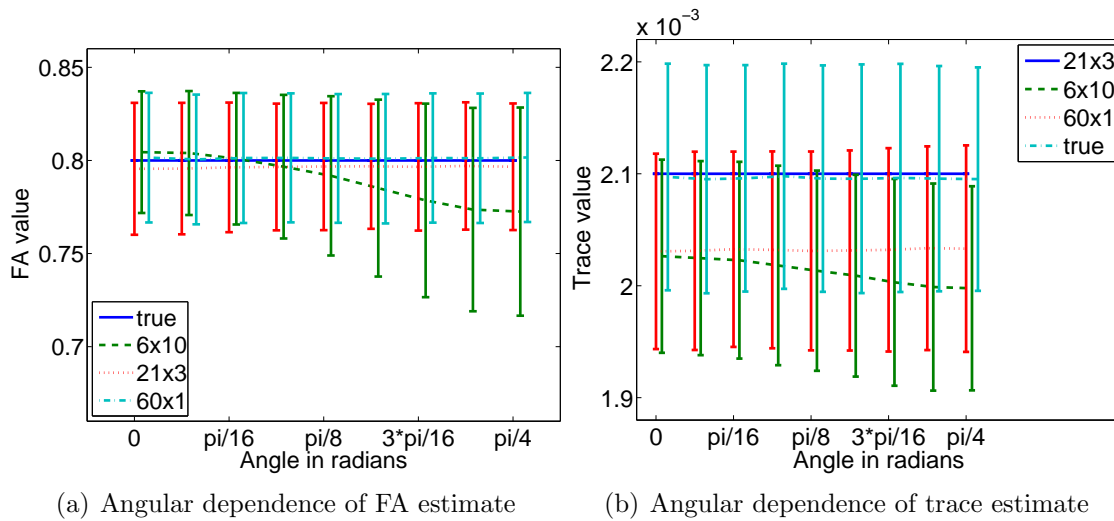


Figure 3.4. The orientation dependence of estimated FA and trace under different sampling schemes. The horizontal axis ranges from the principal diffusion direction unaligned with any gradient direction for $x = 0$ to being perfectly aligned with one of the gradient directions for a rotation of $x = \pi/4$. The noise level is $\sigma = 27$ as determined from our collected data. Notice in the 6 direction scan the difference in mean estimated FA of .04 (5%) between the same tensor orientated at 0 and $\pi/4$ radians. Weighted least squares estimation was used for this simulation.

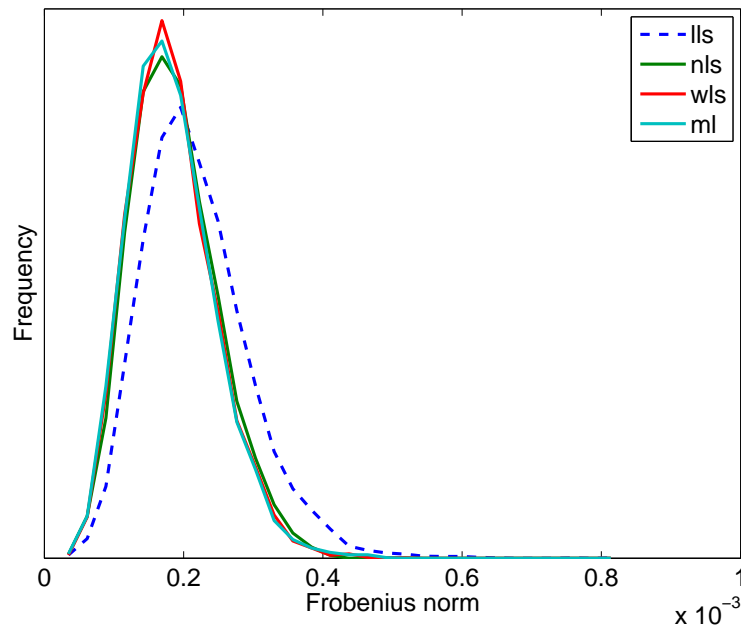


Figure 3.5. Comparison of Frobenius norm of the difference between the estimated and true tensor in Monte Carlo simulations of a tensor with FA=0.8 using 10,000 repetitions and a 60 direction protocol

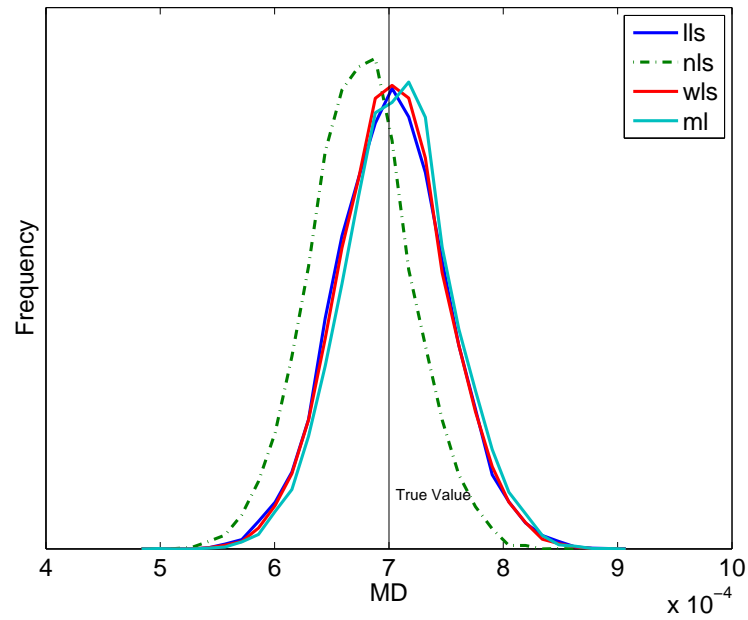


Figure 3.6. Comparison of MD estimate in Monte Carlo simulations of a tensor with FA=0.8 using 10,000 repetitions and a 60 direction protocol

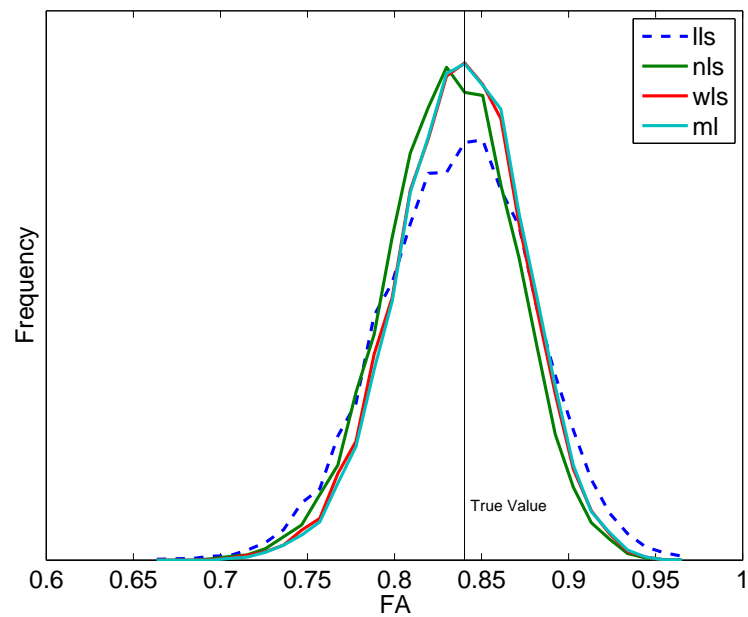


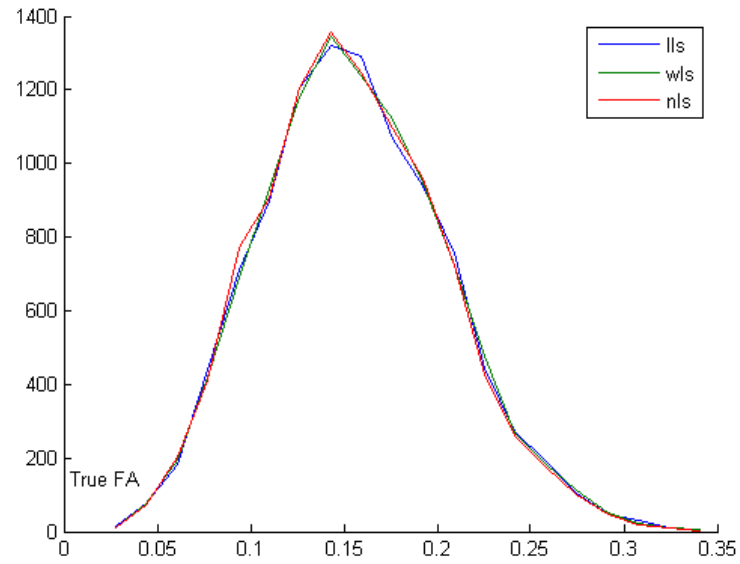
Figure 3.7. Comparison of FA estimate in Monte Carlo simulations of a tensor with FA=0.8 using 10,000 repetitions and a 60 direction protocol

have a lower estimate of trace. Figure 3.8 indicates that most estimation methods produce similar estimates of anisotropy on tensors that are close to isotropic.

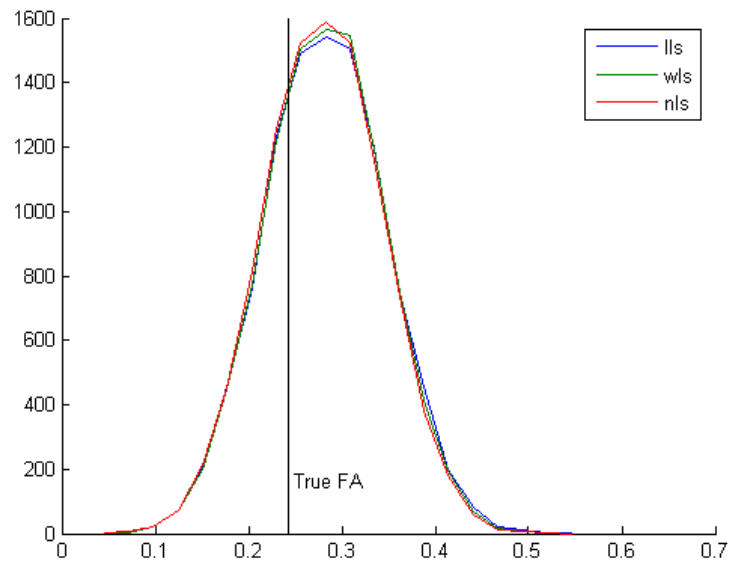
The simulations demonstrate the bias due to orientation of tensor derived measures when using protocols with a minimal number of gradient directions. Furthermore, when protocols with many gradient directions are used, linear least squares estimation can increase variability, and nonlinear least squares estimation can underestimate trace. The simulations predict that the minimum error is introduced by using as many isotropic nonrepeated gradient directions as possible with WLS or ML estimation methods.

3.5 Experiments and Validation

Test sets of real DTI data were acquired under different imaging protocols to compare with the Monte Carlo simulations. Three sets of images of a single healthy adult volunteer were acquired on a Siemens Allegra 3T head-only scanner. The scanning time for each sequence was approximately 12 minutes. Diffusion weighted images were acquired with an isotropic resolution of $2 \times 2 \times 2 \text{ mm}^3$ resolution and image size $128 \times 128 \times 39$. Three different sequences were used: 6 directions with 10 repetitions, 21 directions with 3 repetitions, and 60 directions with 1 repetition. All scans were of approximately equal time to demonstrate the trade-off between image repetition and acquiring more gradient directions. To eliminate bias from differences in the baseline images, the 14 acquired baseline images were registered to a T_2 atlas using a rigid transformation and normalized mutual information. The baseline images were averaged to produce a common baseline image that was used as the reference for the S_0 signal in the following experiments. The transformation from each baseline image to the atlas was also applied to the diffusion weighted images in the corresponding set, and the gradient directions were corrected by the rotation component of the transformation. For sequences with repeated directions, the corresponding gradient directions were averaged as is typical in current processing methods. The noise level σ was estimated from the set of background voxels $\{B_i\}$ using the formula,



(a) FA 0.0



(b) FA 0.2

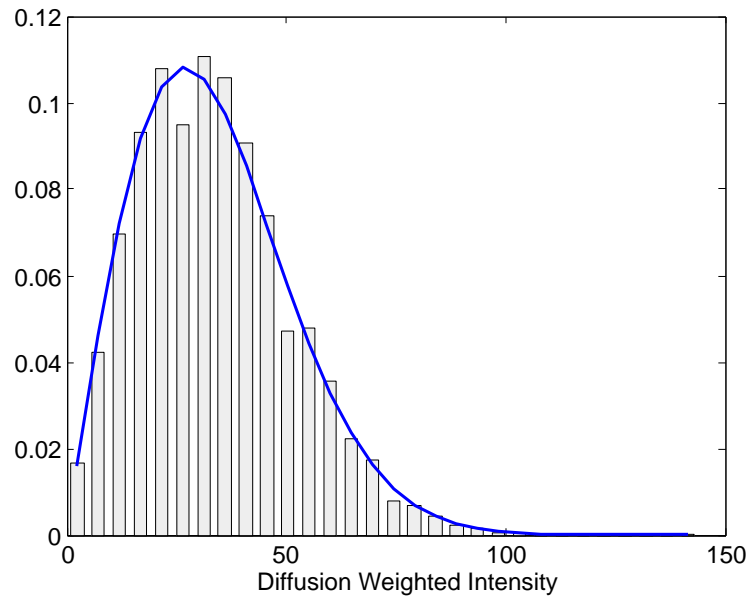
Figure 3.8. Simulated estimation of FA for highly isotropic tensors. In this case, all estimation methods perform similarly.

$$\hat{\sigma} = \sqrt{\frac{1}{2N} \sum_{i=1}^N B_i^2}. \quad (3.13)$$

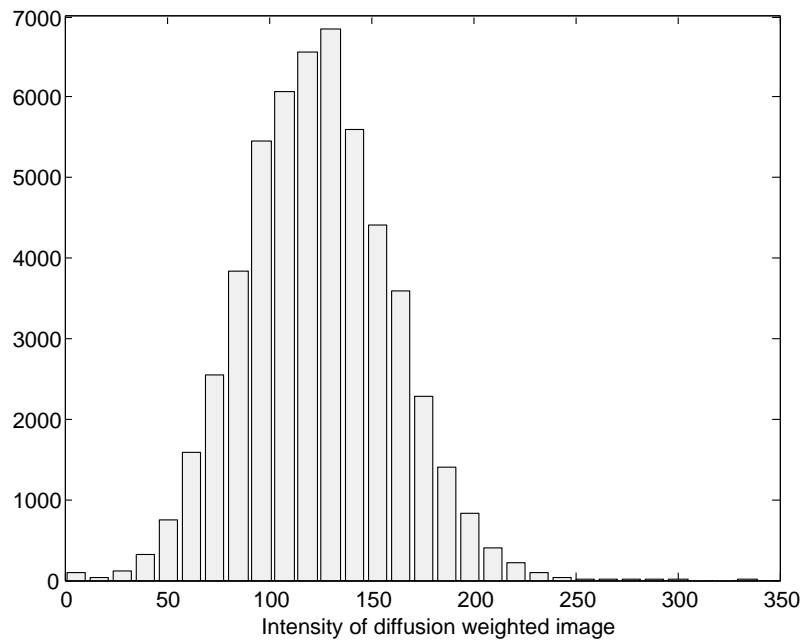
Figure 3.9 show that a Rayleigh distribution fits the distributions of the background voxels.

A white matter segmentation was created by coregistration of a T1 structural image to the averaged baseline image and applying a tissue segmentation tool to the two channels [105, 104]. A label image was created from the six direction image by identifying voxels within the white matter segmentation that are highly aligned or highly unaligned with the closest gradient direction. The angle for each voxel is given by $\theta = \arccos(\min_i(\hat{e}_1 \cdot \vec{g}_i))$, where \hat{e}_1 is the estimated principal eigenvector. In the six direction scan, nearby gradients are separated by $\pi/2$, and as a result, the maximum angle between the principal eigenvector and the nearest gradient direction is $\pi/4$ so $\theta \in [0, \pi/4)$. The threshold for aligned tensors was $\theta < \pi/16$ and for unaligned tensors $\theta > 3\pi/16$. In this experiment, tensors labeled to one of the classes had to have the same label in all three of the gradient schemes. Figure 3.10 shows the labels for the test data overlaid on the FA image.

The difference between the histograms of FA for aligned and unaligned tensors decreases with an increase in the number of gradient directions as shown in Fig. 3.11. Table 3.1 lists the mean difference between aligned and unaligned voxels using the three different gradient schemes and each tensor estimation method. Table 3.2 gives the mean and variance of the estimate for trace for each estimation method and acquisition scheme. The experimental results confirmed the simulation prediction of underestimated anisotropy in tensors aligned in the 6 direction scan, because the difference decreases as the number of gradient direction increases. The experimental estimate of tensor trace is higher for low directions images, which is different than the simulation prediction. The difference could be due to the assumption of a single tensor model in the simulation. The evidence indicates that studies comparing different regions could be substantially biased by the orientation of the tissue within the magnetic field. Therefore, studies relying on statistical analysis of anisotropy measures should use as many gradient directions as possible within the



(a) Image background



(b) White matter gradient image

Figure 3.9. Histograms from diffusion weighted images. The histogram on the left (a) is a sample from the background used for estimating the noise level $\sigma = 27$. The Rayleigh distribution parametrized by σ fits the histogram nicely. The figure on the right (b) is a histogram of the observed intensity values in one of the diffusion weighted images. As shown in Fig. 3.3, intensities measurement are biased up to four times the noise level, and a significant percentage of the voxels in (b) falls within this range.

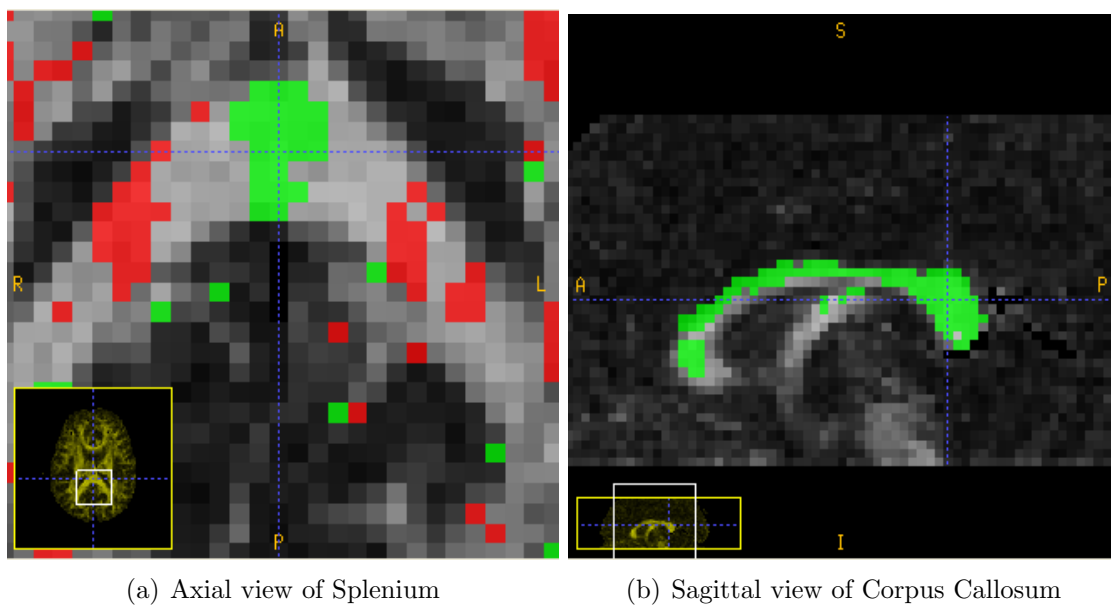
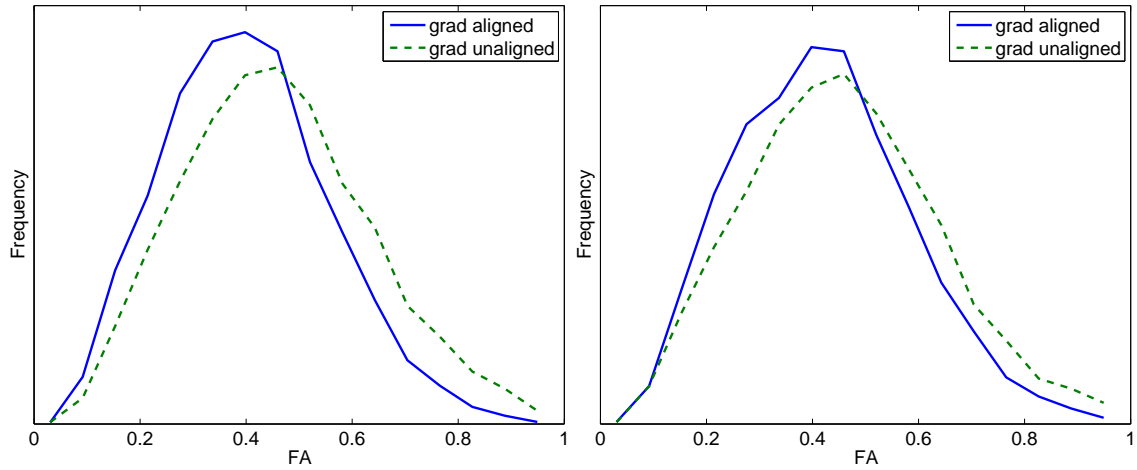
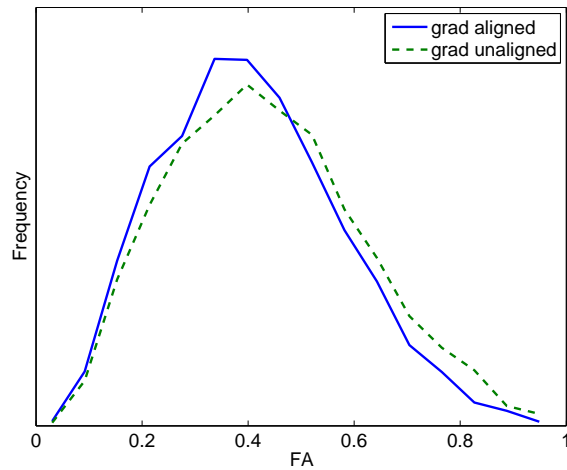


Figure 3.10. Labels for aligned and unaligned voxels. The voxels labeled as aligned or unaligned are highlighted in red and green, respectively. The figure on the left (a) shows an axial slice of the Splenium and the figure on the right (b) shows a sagittal view of the corpus callosum.



(a) 6 gradient directions with 10 repetitions

(b) 21 gradient directions with 3 repetitions



(c) 60 gradient directions with 1 repetition

Figure 3.11. Histograms of estimated FA using weighted least squares estimation for aligned and unaligned tensors with (a) 6 gradient directions with 10 repetitions (b) 21 gradient directions with 3 repetitions and (c) 60 gradient directions with 1 repetition. Notice the significant reduction in difference between the two histograms as the number of gradient directions increases, because of a decrease in noise bias.

Table 3.1. Mean and variance of FA values in aligned and unaligned voxels.

	6 (10 reps)	21 (3 reps)	60 (1 reps)
lls (aligned):	0.401 (0.0240)	0.414 (0.0259)	0.403 (0.0269)
lls (unaligned):	0.453 (0.0298)	0.444 (0.0291)	0.422 (0.0291)
difference:	0.053	0.030	0.019
nls (aligned):	0.401 (0.0240)	0.417 (0.0265)	0.399 (0.0270)
nls (unaligned):	0.453 (0.0298)	0.449 (0.0304)	0.420 (0.0299)
difference:	0.053	0.032	0.020
wls (aligned):	0.401 (0.0240)	0.419 (0.0267)	0.406 (0.0276)
wls (unaligned):	0.453 (0.0298)	0.451 (0.0306)	0.427 (0.0306)
difference:	0.053	0.032	0.021
ml (aligned):	0.416 (0.0272)	0.425 (0.0272)	0.407 (0.0278)
ml (unaligned):	0.461 (0.0303)	0.458 (0.0315)	0.427 (0.0309)
difference:	0.045	0.033	0.021

The difference rows highlight the change between the mean FA of the aligned and unaligned voxels. The difference between the mean FA decreases with an increase in the number of gradient directions, indicating that some of the difference is due to the choice of gradient sampling.

Table 3.2. Mean and variance of trace values in white matter.

	6 directions (10 reps)	21 directions (3 reps)	60 directions (1 reps)
LLS:	2.373e-03 (7.2071e-08)	2.304e-03 (7.7886e-08)	2.307e-03 (2.2293e-07)
NLS:	2.373e-03 (7.2071e-08)	2.289e-03 (7.7122e-08)	2.235e-03 (2.0839e-07)
WLS:	2.373e-03 (7.2071e-08)	2.307e-03 (7.8263e-08)	2.311e-03 (2.2847e-07)
ML:	2.472e-03 (8.5249e-08)	2.383e-03 (1.0698e-07)	2.326e-03 (2.4044e-07)

The six direction scan has the highest estimated trace. In the 21 and 60 direction scans, the nonlinear least squares method has a lower estimate of the trace than the other methods. The ML estimator has the highest estimate of trace of all the methods.

time constraints instead of repeating a minimum number of gradient directions. The results from the analysis of the *in-vivo* scans confirms the results of the simulation experiments.

3.6 Conclusions

In this chapter, the magnitude of error in DTI measurements caused by imaging noise was evaluated through Monte Carlo simulations and *in-vivo* experiments. Low direction gradient acquisition schemes introduce a statistical bias due to orien-

tation within the magnetic field with a clinically relevant magnitude of around 5% for highly anisotropic tensors. Furthermore, standard linear least squares tensor estimation introduces additional variability in tensor estimation when many gradient directions are employed. Understanding the magnitude of these two effects is critical for interpreting the results of statistical analysis. For new imaging studies, these results indicate that scans with one image for each of a large number of gradient direction should be preferred over protocols with a small number of repeated gradient directions, and that WLS or ML tensor estimation should be preferred.

CHAPTER 4

DTI ATLAS BUILDING

4.1 Introduction

This chapter uses the techniques of registration and atlas building to provide intersubject correspondence for statistical analysis of diffusion data. An overview of the procedure is shown in Fig. 4.1. The metric for optimizing the registration parameters is based on a structural operator of the tensor volumes. An initial alignment is performed by computing the affine transformation between the structural images, and applying the transformation to the tensor volumes. An unbiased, deformable atlas building procedure is then applied that produces mappings between each subject and a common atlas coordinate system using the method of Joshi et al. [53]. Deformed images are averaged to produce a template tensor atlas suitable for fiber tractography, as shown in Fig. 4.2. The atlas tracts may be mapped back into individual native space using the inverse of the transformations to the atlas. In the native space, individual diffusion statistics are collected. This provides a mechanism for establishing a population correspondence of atlas geometry. Preliminary validation is provided by showing an improvement over affine registration alone. Validation measures for comparing fiber tracts produced in the atlas are provided in Chapter 5.

4.2 Registration

This chapter presents an intermediate, heuristic solution for DTI registration positioned between using only baseline images and using metrics based directly on the diffusion tensors. A feature image for registration is based on a structural operator of the FA image that is sensitive to major fiber bundles. Given a tensor image I and the corresponding FA image FA , the structural operator C is defined

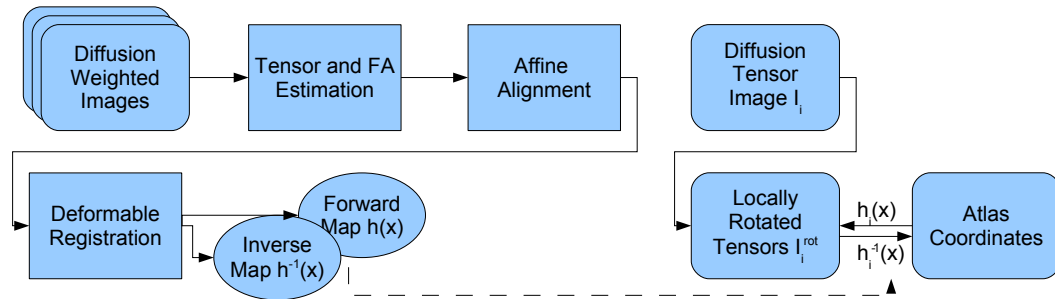


Figure 4.1. Flowchart of atlas building process.

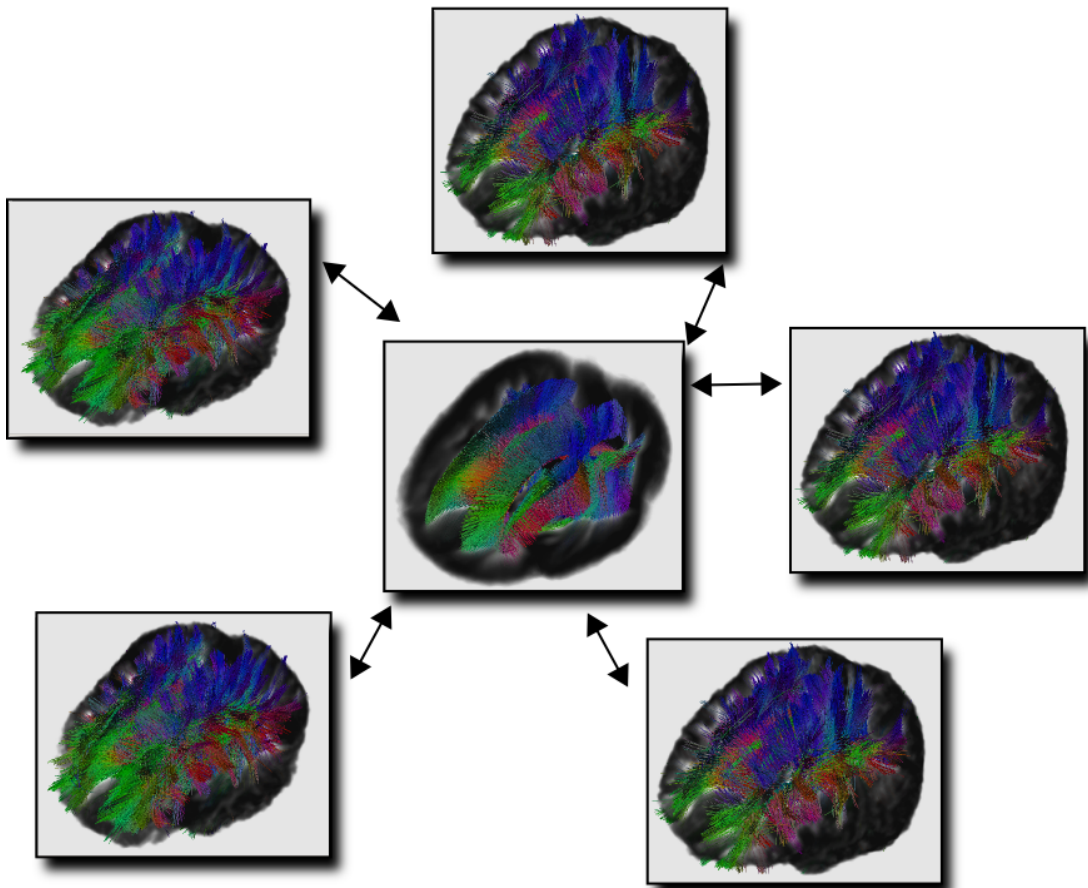


Figure 4.2. Deformation of tensor fields into atlas space preserves the full information needed for fiber tractography and diffusion statistic analysis.

in terms of the maximum eigenvalue of the Hessian,

$$C = \max [\text{eigenvalues}(\mathbf{H})], \text{ where } \mathbf{H} \equiv \begin{pmatrix} FA_{xx} & FA_{xy} & FA_{xz} \\ FA_{yx} & FA_{yy} & FA_{yz} \\ FA_{zx} & FA_{zy} & FA_{zz} \end{pmatrix}. \quad (4.1)$$

Figure 4.3 shows the FA image of a tensor field and the corresponding structural image C . As discussed in early computer vision work, the second derivative of Gaussian serves as an efficient detector of ridge structures [21]. The Hessian serves as a computational approach for finding the direction of maximum ridge response. Let $h_i(x)$ be a mapping that gives the corresponding point in the subject image I_i for all x in the domain Ω of the atlas image \hat{I} . Given two images I_1 and I_2 , the image match functional that is optimized in the registration process is

$$M(I_1(x), I_2(h(x))) = \int_{x \in \Omega} [C_1(x) - C_2(h(x))]^2 dx, \quad (4.2)$$

the mean squared error between C_1 and C_2 .

The feature image C is chosen over existing methods for two main reasons. First, C is a good detector of major fiber bundles that occur as tubular or sheet-like structures. Callosal fibers form a thin swept U; the corona radiate is a thin fan; the cingulum is a tubular bundle. C serves as a feature detector for all types of these thin structures. Consequently, C optimizes correspondence of fiber tracts better than the baseline image, because C has the strongest response at the center of major fiber bundles, whereas the baseline image has the strongest signal in the cortico-spinal fluid (CSF). In practice, achieving maximal response at the center of a sheet like structure requires the width of the derivative kernel to be appropriately optimized. In this work, the scale was chosen heuristically by computing the feature image using uniform sampling of a range of scales from $.5 - 4mm$. Visual inspection of these results was used as a guideline for selecting σ in order to have a strong response in white matter structures, especially the corpus callosum and internal capsule. As a secondary consideration, the scale was also chosen to be sure that the fornix and cingulum bundles were preserved in the feature image. C is used instead of a full tensor metric or the FA itself in order to reduce overfitting the diffeomorphic registration by using the same feature for registration that will be

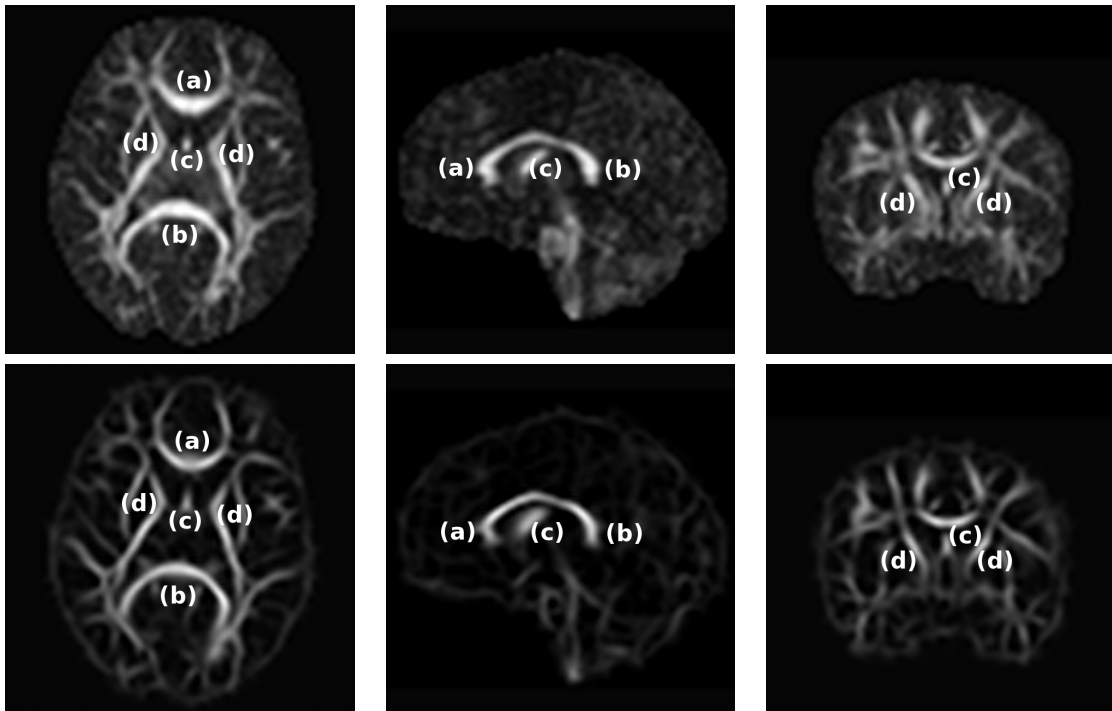


Figure 4.3. Comparison of FA and feature images. The top row shows axial, sagittal, and coronal slices of the FA image from a DTI scan of a 1-year old subject. The bottom row shows the result of the structural operator on the FA image taken at $\sigma = 2.0mm$. Major fiber bundles such as the (a) genu of the corpus callosum, (b) splenium of the corpus callosum, (c) fornix, and (d) internal capsules are highlighted, whereas the background noise is muted.

used for statistical comparison. The Hessian at a fixed scale is a first step towards basing the registration on a geometric model of the white matter, and future work could investigate a multiscale approach to computing C to make the measurement dependent only on the local width of the structure.

Using the definition for the image match functional, registration of the images proceeds in two stages. First, each subject image is aligned into a standardized coordinate system by affine alignment of the baseline image with a T_2 atlas using normalized mutual information. However, the affine registration does not account for the nonlinear variability of the white matter geometry, and atlases built from only affine aligned images result in blurring of many of the white matter structures. For this reason, a deformable registration procedure is employed to obtain anatomical correspondence between the population of images I_i and a common atlas space [53]. This procedure jointly estimates an atlas image \hat{I} and a set of diffeomorphic mappings h_i that define the spatial correspondence between \hat{I} and each I_i . Figure 4.4 shows the improved correspondence attained from the deformable registration. The computed transformations are applied to each tensor volume as described in the next section.

4.3 Tensor Processing

The application of high-dimensional transforms to the DTI volumes must account for the space of valid tensors. The orientation of a diffusion tensor provides a measurement of fiber orientation relative to the anatomical location, and spatial transformations of the tensor fields must account for the reorientation of the tensor. Furthermore, because diffusion tensors are symmetric positive-definite matrices, operations on the images must preserve this constraint.

4.3.1 Spatial Transformations of Tensor Images

When spatial transformations of diffusion images are performed to align the anatomy of different scans, the tensors must also be transformed to maintain the relationship between anatomy and tensor orientation. The finite strain approach of Alexander et al. to reorient tensors in a deformation field decomposes the local linear

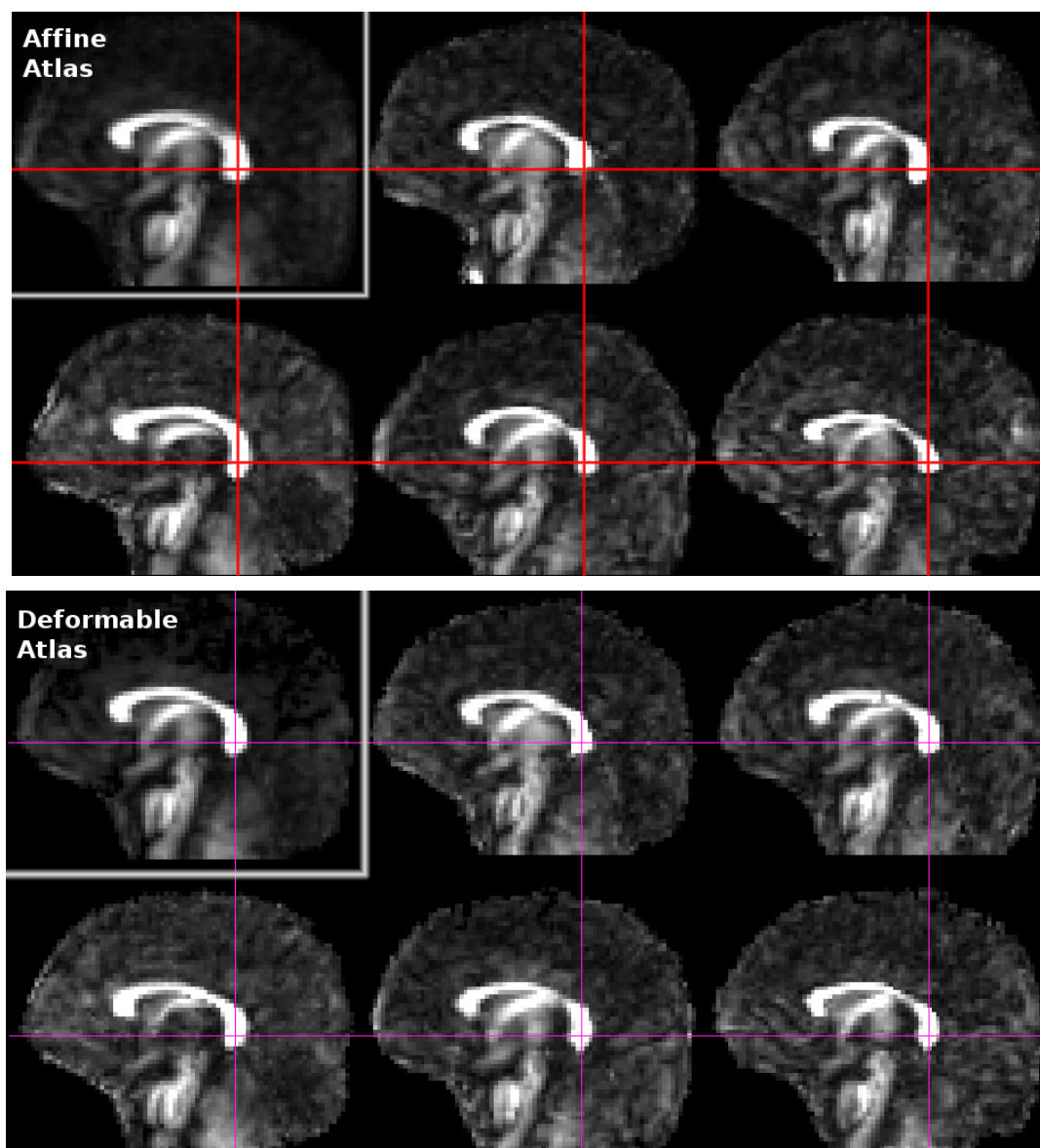


Figure 4.4. Comparison of affine and diffeomorphic registration. The top six images show the correspondence of the affine atlas and the five subject images at a point in the splenum of the corpus callosum. Notice the corresponding index in the subject images does not necessarily correspond to the same anatomical location. The bottom six images show the deformable atlas and subject images with the same point selected. Here, the atlas provides better anatomical correspondence, and the deformable atlas has sharper structures.

approximation of the transformation into a rotation and deformation component [2]. The local linear transformation, F , is found by computing the Jacobian matrix from the deformation field with finite differences. The rotation of each tensor is computed by performing singular value decomposition (SVD) on the local transformation F . A local linear deformation F is decomposed into a rotation matrix R and a deformation matrix U , where

$$F = UR. \quad (4.3)$$

The local transformation of a tensor D is given as

$$D' = RDR^T. \quad (4.4)$$

4.3.2 Interpolation and Averaging of Tensor Images

The space of valid diffusion tensors does not form a vector space. Euclidean operations on diffusion tensors such as averaging can produce averages with a larger determinant than the interpolating values, which is not physically sensible. Furthermore, operations on diffusion tensors are not guaranteed to preserve the positive-definite nature of diffusion. The Riemannian framework has been shown as a natural method for operating on diffusion tensors, which preserves the physical interpretation of the data, and constrains operations to remain in the valid space of symmetric positive-definite matrices [33, 34, 81]. In these methods, statistics are computed in a tangent space to the manifold of symmetric positive definite matrices. For the case of computing statistics of diffusion tensors, the mean is defined as a Fréchet mean that minimizes the geodesic distances between the mean tensor, \hat{D} , and the set of tensors D_i ,

$$\hat{D} = \arg \min_D \sum_{i=1}^N d(D, D_i)^2. \quad (4.5)$$

Covariance statistics are computed in the tangent plane located at the mean \hat{D} on the manifold. Further simplifications have shown an efficient method for computation using the Log-Euclidean metric [5, 6]. This simplification assumes that the identity matrix is a close approximation to the mean, removing the need to

compute the mean via a gradient descent algorithm. Interpolation and averaging are treated as weighted sums in the Log-Euclidean framework defined as

$$\hat{D} = \exp \left(\sum_{i=1}^N w_i \log(D_i) \right), \quad (4.6)$$

where \log and \exp are the matrix logarithm and exponential, respectively. To produce the atlas tensor volume, the deformed tensor volumes with locally rotated tensors are averaged per-voxel using the Log-Euclidean scheme,

$$I^{\text{rot}}(x) = R(x)I(x)R(x)^T, \quad (4.7)$$

$$\hat{I}(x) = \exp \left(\frac{1}{N} \sum_{i=1}^N \log(I_i^{\text{rot}}(h_i(x))) \right). \quad (4.8)$$

4.4 Atlas Tractography

The atlas tensor volume provides an image with improved SNR that is used to create template fiber tracts. The diffusion tensors obtained from averaging across the population can be integrated using streamline tractography approaches with significantly less outliers than in noisy individual images. For the purpose of this study, a simple streamline integration method based on fourth order Runge-Kutta integration of the principal eigenvector field is applied. Manual seeding and clustering of resulting tracts is used to input prior anatomical knowledge into the segmentation of fiber bundles. After creation of the template atlas fiber tracts, diffusion statistics from the individual cases are mapped to the atlas tracts. When mapping the diffusion properties from native space to the template tracts, scalar invariants are interpolated from the native space using trilinear interpolation. The procedure results in a fiber bundle for each subject with the geometry of the template atlas tract but replacing the diffusion properties with those mapped from the subject. In this work, tracts were chosen by the author to illustrate the methodology, but future clinical studies should rely on clinical hypotheses and expert neuroanatomical knowledge for tract definition. The set of individual tracts with corresponding geometry but varying diffusion properties are compared in a

novel statistical framework as described in Chapter 6. Validation of the atlas tracts is investigated in Chapter 5.

4.5 Experiments and Results

The atlas building procedure was initially tested on 5 image volumes of healthy 1-year-old subjects from a clinical study of neurodevelopment. The images were acquired on a Siemens head-only 3T scanner. Multiple sets of diffusion weighted images were taken for each subject and averaged to improve signal-to-noise ratio. Each dataset consisted of 1 baseline image and 6 gradient direction images with $b=1000\text{s/mm}^2$ using the standard orientation scheme. An image volume of $128 \times 128 \times 65$ voxels was acquired with $2 \times 2 \times 2 \text{ mm}^3$ resolution. Imaging parameters were $\text{TR/TE} = 5200\text{ms}/73\text{ms}$.

For each set of diffusion weighted images, the diffusion tensors were estimated using LLS estimation. In this case all least squares techniques are equivalent because a minimal gradient encoding was applied. The structural image C was computed from the FA volume with $\sigma = 2.0\text{mm}$. Affine and deformable alignment were computed using the methods described in section 4.2. The warped DTI volumes were averaged to produce an affine atlas and a deformable atlas. Figure 4.5 shows a comparison between the tensor volumes of the two atlases. Tractography was performed in the atlas space, and the tract bundles were warped to each subject image using h_i . Figure 4.6 shows the results of tractography in the atlas and the corresponding warped fibers in two subject images.

4.6 Preservation of Edges

Visual inspection of tractography in the atlas volume shows an initial qualitative validation that the registration and averaging methods provide anatomically sensible results. Histogram comparisons of derived tensor measures in the affine and diffeomorphic atlas show an initial quantitative validation of the improvement of the deformable registration over affine registration alone. The gradient magnitude of the FA was measured in the whole brain of the affine and deformable atlases. Figure 4.7 shows the gradient magnitude images and a histogram comparison. At

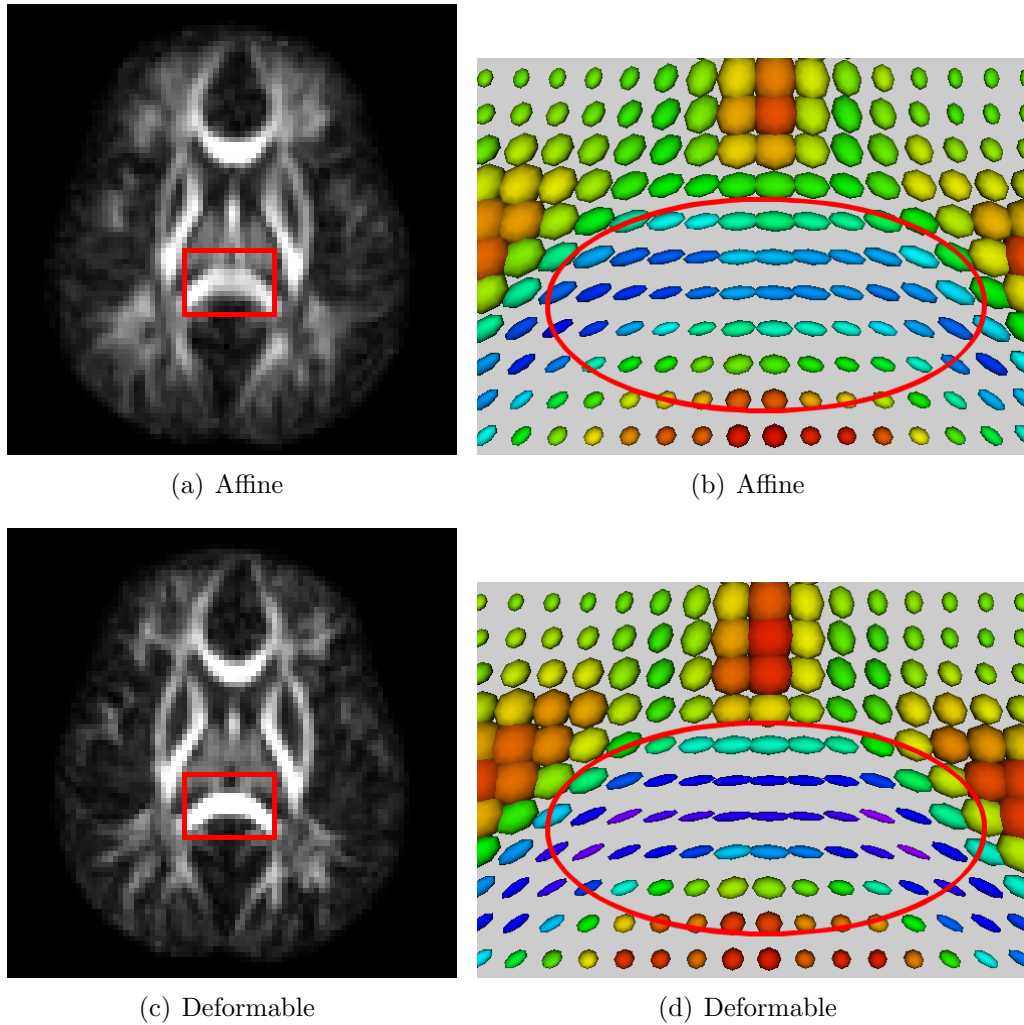
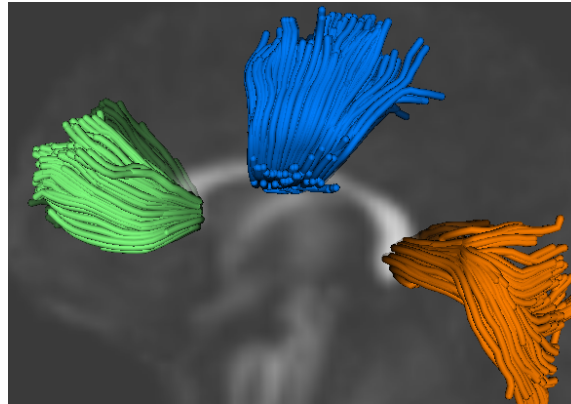
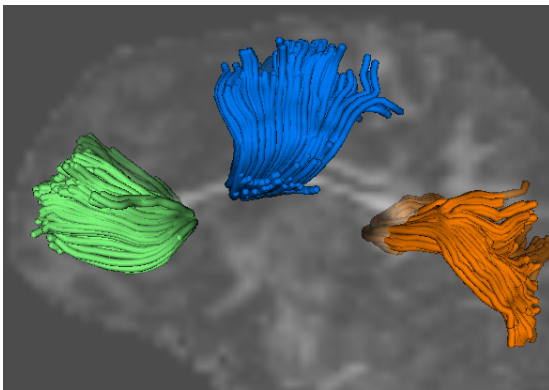


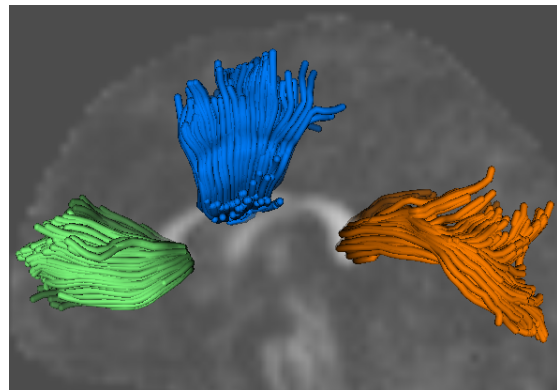
Figure 4.5. Axial slice of the FA and ellipsoids for the affine and deformable atlases. (a) and (c) show a slice of the FA for the affine and deformable atlases. (b) and (d) illustrate a subregion of tensors in the splenium of the corpus callosum. Notice that the FA image of the affine atlas is more blurry, and that the tensors in the splenium are more swollen in the affine atlas.



(a) Atlas



(b) Image 1



(c) Image 2

Figure 4.6. Fibers in atlas and corresponding fibers in subject space. Fibers traced in the corpus callosum of the atlas (a) are mapped to corresponding locations in the subject images (b) (c) despite pose and shape changes.

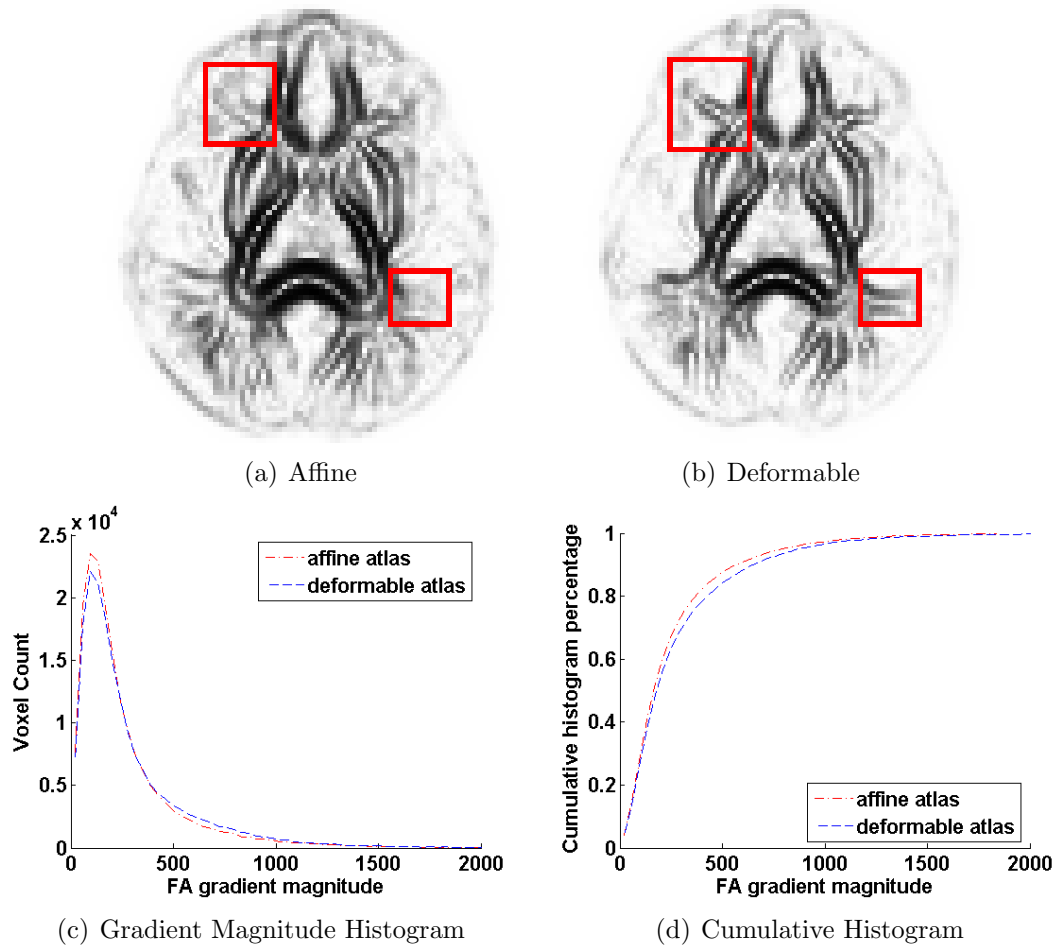


Figure 4.7. FA gradient in affine and diffeomorphic atlases. (a) and (b) show an axial slice of the gradient magnitude image. Notice the structures in the marked regions that are visible in the deformable atlas, but not the affine atlas, and the increased sharpness of the splenium of the corpus callosum. Figures (c) and (d) show the histogram and cumulative histogram of gradient magnitude intensities in the whole brain.

the 90th percentile of the cumulative histogram, the deformable atlas has a gradient magnitude of 684 whereas the affine atlas is 573, an increase of 20%. This shows that the deformable atlas better preserves thin structures via improved alignment.

4.7 Conclusion

This chapter presented an automatic method for producing correspondence in diffusion tensor images through deformable registration and a novel image match metric that aligns images based on local geometry measures. Transformations are applied to the tensor images using the finite strain model for tensor rotation and a Riemannian framework for averaging and interpolation. Tractography can be performed in the atlas space to identify a fiber bundle population model. Initial validation of the deformable registration showed an improvement in thin structure preservation over affine alignment alone. Additional validation is presented in Chapter 5 to evaluate the differences between tracts computed in the atlas and those generated in the subjects native space.

CHAPTER 5

MEASURES FOR VALIDATION OF TRACTOGRAPHY

5.1 Introduction

Chapter 4 presented a method for building an atlas from a population of DTI that is used in Chapter 6 for tract-based statistical analysis. To validate the use of atlas building for the tract-based analysis, some error bounds need to be placed on differences between tracts produced in the population atlas and those generated in individual images. This problem is closely related to many other validation problems in DTI analysis. This chapter, therefore, proposes a set of validation measures for evaluating differences in fiber bundles generated by streamline tractography.

Several groups have previously proposed measures for evaluating tractography and DTI atlas building. Zhang et al. proposed several methods for evaluating their registration procedure including differences in tensor parameters as well as evaluation of white matter fiber bundle differences [115]. The fiber bundle measure is similar to that presented later in section 5.2.2 but does not account for the distribution of closest point distances between two fiber bundles. Ziyang et al. proposed a fiber match metric, FiT, to evaluate the agreement of a fiber bundle deformed into an image for the particular case of comparing tracts to a registered image [117]. This method, however, is unable to compare tracts produced by different algorithms and places an emphasis on the tangent vector of individual streamlines. This chapter presents a set of measures for evaluating the difference between fiber bundles including both geometric measures and comparison of the diffusion statistics segmented by fiber bundles. These measures can be used for evaluating new tractography algorithms, quality control, measuring reproducibility, and comparing atlas-based segmentation to manual tractography. In this thesis,

measures are used to evaluate tractography mapped from an atlas to fiber bundles generated by tractography in native space.

5.2 Tractography Comparison Measures

This section covers a set of measures that can be used to compare streamlines generated by fiber tractography. The motivation is to compare fiber bundles using measures that are robust to outliers, provide physical intuition, and focus on the global shape of the fiber bundle rather than individual streamlines.

5.2.1 Volumetric Overlap

As a preliminary measure of volumetric overlap, the probabilistic overlap metric implemented in Valmet was adapted to tractography [38]. This measure is referred to as the binary tractography overlap (BTO) and is defined by

$$BTO = 1 - \frac{\sum_i |P_A(x_i) - P_B(x_i)|}{\sum_i P_A(x_i) + P_B(x_i)}. \quad (5.1)$$

Here, $P_A(x_i)$ is a measure of the probability that voxel x_i is part of the fiber tract. This is approximated by dividing the number of streamlines in the voxel by the median number of streamlines over all voxels containing any streamlines and clamping to a maximum value of 1. This approximation is intended to label as high probability voxels of the tract containing a significant number of streamlines while tapering out the influence for voxels with only a few streamlines.

This method benefits from the similarity to existing volumetric overlap measures and its relative simplicity. Furthermore, this method can compare streamline methods with recently proposed volumetric tractography methods [35, 68]. However, volumetric overlap measures for tractography have several serious drawbacks. First, the measure is limited to grid-based measurements that are significantly affected by partial voluming effects. Second, many fiber tracts in the human brain are long in 1 dimension and narrow in 1 or 2 orthogonal dimensions. For example, the cingulum is a long thin tube. As shown in Fig. 5.1, misregistration of fiber bundles by less than 1 voxel in thin dimensions can result in overlap measures that are significantly smaller, whereas larger structures misaligned by similar physical

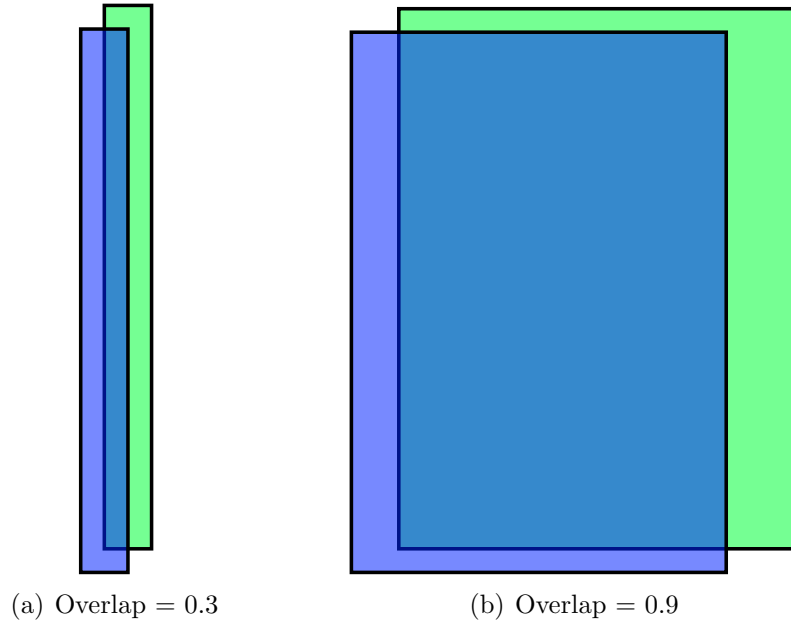


Figure 5.1. Example of instability of overlap measures for thin structures.

amounts have much higher overlap measures. An additional drawback of the *BTO* measure is the lack of physical units that gives little intuition into how tracts differ.

5.2.2 Point Cloud Divergence

A second method of measuring tract differences can be considered that treats fiber bundles as sampled point clouds. This approach avoids some of the drawbacks of converting streamlines into a voxel grid. To compare two fibers bundles A and B , find the distance between each point p_i in A and the closest point q_i in B . A graphical representation showing the closest point distance for each fiber bundle is shown in Fig. 5.2. For efficient lookup of the closest point, a Delaunay triangulation of the points in tract B can be computed and used for fast lookup of the closest point to p_i . This produces a distribution of distances $d(p_i, q_i)$, from bundle A to bundle B . As shown in Fig. 5.3, these distributions are heavily weighted towards zero with a large percentage of points being very close. At the maximum of the distribution, there are typically a small number of streamlines, which diverge between the bundles that produce large distances. Previous research has considered the minimum, mean, or maximum of such distributions [24, 115]. However, the minimum and mean

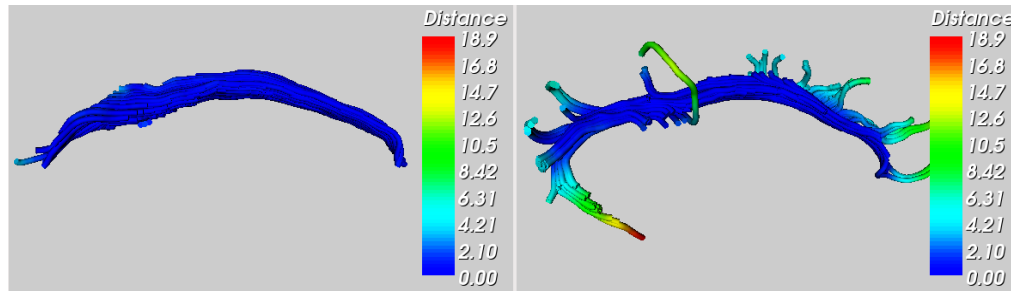


Figure 5.2. Closest point distances for atlas and individual tractography results for the right cingulum in a subject.

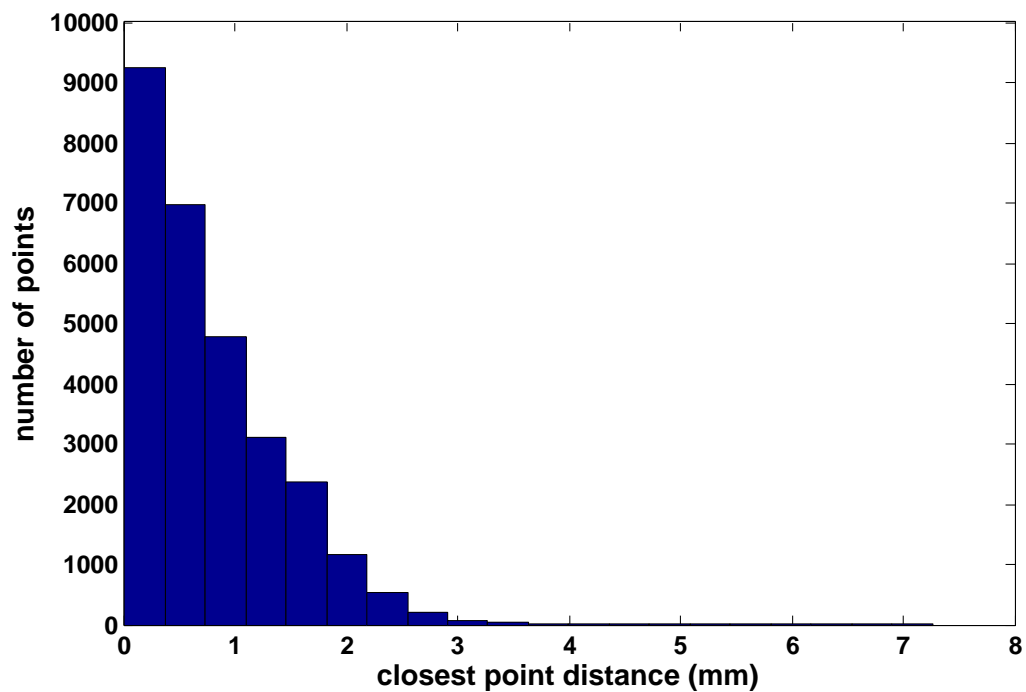


Figure 5.3. Histogram of closest point distances from atlas tract to individual tract.

distance are heavily biased by the large percentage of closest point distances that are very close to zero. The maximum, on the other hand, is extremely sensitive to the outliers common in streamline tractography.

Instead, a family of closest point distances between two fiber bundles A and B , $PC_\alpha(A, B)$, should be defined as the α quantile of the distribution of distances from A to B . Choosing α to be relatively close to 1 gives a measure that is resistant to outliers, but gives an intuition of how close the bulk of points are between the

two bundles. For example, $CP_9(A, B) = 2.0mm$ provides an upper confidence limit that 90% of points in A are within 1 voxel of B with the $2 \times 2 \times 2 mm^3$ voxels common in DTI. PC_α is not symmetric with respect to the order of A, B and is therefore not a true metric. Although the measure could be made symmetric by combining both the closest point distances from A to B and B to A , the asymmetry is left to enable measurements such as tract A being contained within a larger tract B . For this situation, $PC_\alpha(A, B)$ would be small, but $PC_\alpha(B, A)$ would be large.

5.2.3 Ellipsoid Distance

A third measure provides a global estimate of the distance between two tracts. For this metric, an ellipsoid is computed for each fiber bundle and serves as a first order shape model. The ellipsoid for each fiber bundle is computed by finding the center and covariance of all points making up the fiber bundle. A diagram of two fiber bundles and their respective ellipsoids is shown in Fig. 5.4. Because streamline tractography is prone to outliers, the ellipsoid is computed by the fast implementation of the minimum covariance determinant (MCD) estimator [85]. The distance between the two ellipsoids is measured in two ways. First, the Euclidean distance between the centers of the two ellipsoids is referred to as ED_c . Second, the Bhattacharyya coefficient ED_ρ is used to measure the difference between the ellipsoids [54]. For Gaussian distributions with means m_1, m_2 and covariances S_1, S_2 with pooled covariance $S = (S_1 + S_2)/2$,

$$B = \frac{1}{8}(m_2 - m_1)^T R^{-1}(m_2 - m_1) + \frac{1}{2} \ln \left(\frac{|S|}{\sqrt{|S_1||S_2|}} \right) \quad (5.2)$$

$$ED_\rho = e^{-B}. \quad (5.3)$$

ED_ρ is bounded $0 \leq ED_\rho \leq 1$ and equals 1 when the distributions are equal.

5.2.4 Functional Difference

The previous three measures all focus on establishing geometric distances between two fiber bundles. The final proposed measure instead describes differences in the diffusion parameters sampled by the fiber bundles. This provides a more explicit measure of differences for studies focused on the statistical analysis of

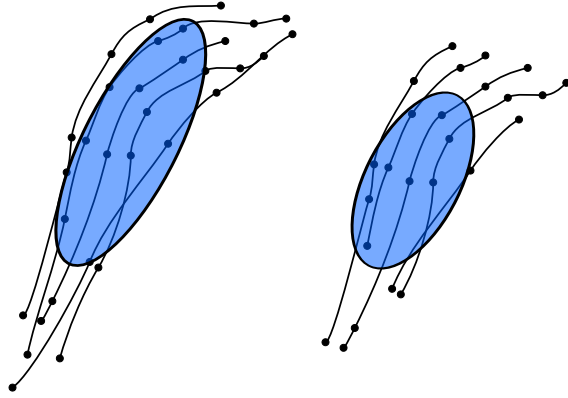


Figure 5.4. Ellipsoid representation of bundle shape.

scalar invariants. Using the methodology described by Corouge et al., an arc length function for FA and MD is compared between fiber bundles [23]. To summarize the functional difference, FD , the mean difference between the function for bundle A , $f_A(t)$, and the function for bundle B , $f_B(t)$, is computed by

$$FD = \frac{1}{t_n - t_m} \int_{t_m}^{t_n} |f_A(t) - f_B(t)| dt. \quad (5.4)$$

(5.4) is computed for both FA and MD.

For this study, all tracts were mapped into a template atlas space to compare the functional differences. A single origin was used for each tract to compare the tract generated in the atlas to the native space tract mapped to the atlas. To ensure that functions for both bundles have the same domain, the values for t_m and t_n are restricted to the interval that contains at least an adequate percent of the total streamlines. For this study, the interval was restricted to contain at least 30% of the streamlines for both fiber bundles. An example of $f_A(t) - f_B(t)$ for a population is shown in Fig. 5.5. The summary measure, Eq. 5.4, is the average absolute difference over the domain.

5.3 Evaluation of Atlas Tractography

The measures from the previous section were used to evaluate tractography based on an atlas built from images of 37 subjects in a study of schizophrenia in adults. Each subject was imaged using a protocol with 8 nondiffusion weighted

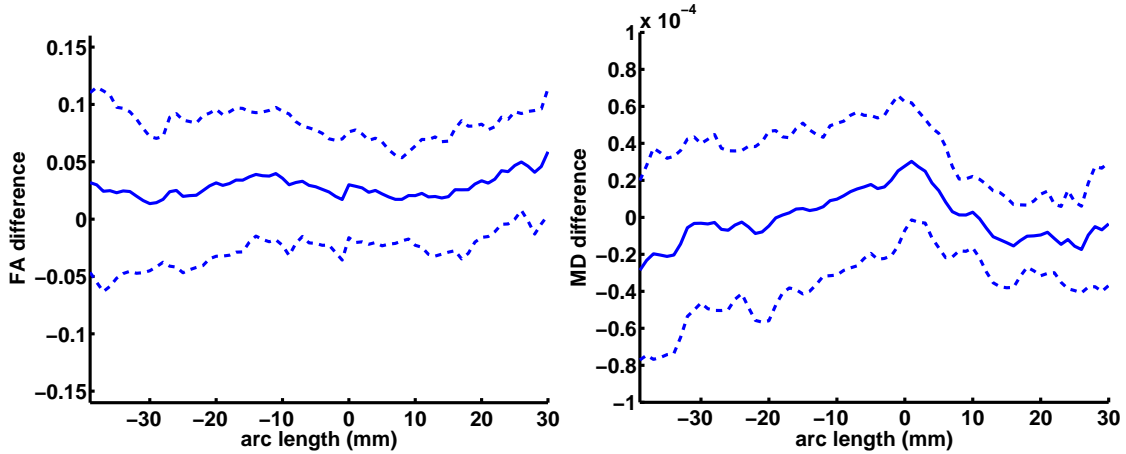


Figure 5.5. Mean and standard deviation of differences between functions produced by atlas tractography and individual tractography mapped to atlas for the right uncinatus.

images and 51 diffusion weighted images at a resolution of $1.6667 \times 1.6667 \times 1.7 \text{ mm}^3$. A b-value of 900 was used for the diffusion weighted images. The purpose of this application was to use the proposed measures to evaluate differences between tractography produced by mapping from an atlas to tractography generated in an individual. As is true for most DTI studies, there is no ground truth for the true geometry of fiber bundles. Instead, this evaluation bounds differences of atlas mapped tractography to native space analysis. An atlas was computed using the method described in Chapter 4. Fiber bundles were extracted in the mean atlas image using a Runge-Kutta streamline tractography algorithm. Manual clustering and cutting of the tract was performed to obtain an anatomically appropriate set of streamlines for several tracts. The five extracted tracts were the fornix, left and right cingulum, and left and right uncinatus and are shown in the atlas space in Fig. 5.6. These atlas tracts were mapped into each individual using the transformations from the atlas building.

Tractography was then computed in each individual image space. Seed regions for the tractography were manually developed in the atlas and then mapped to each subject using the atlas transformations. After testing a variety of FA thresholds for the individual tractography, a global threshold of $FA = 0.15$ was chosen to

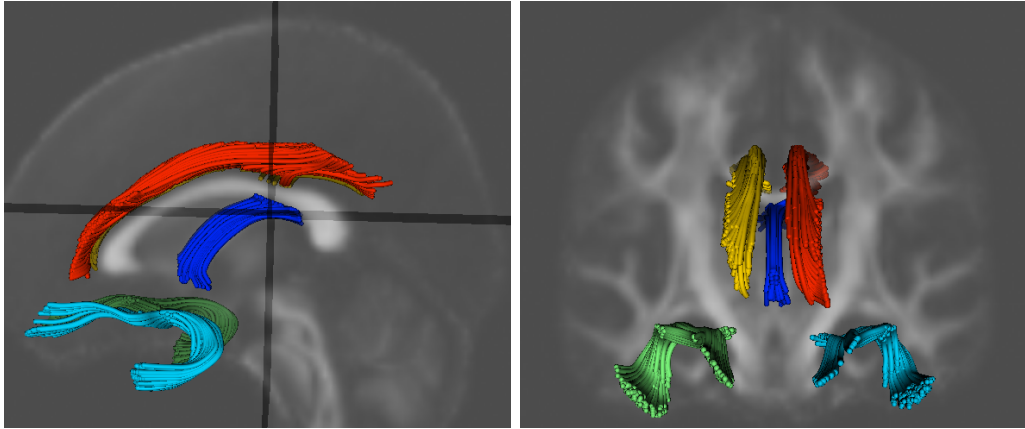


Figure 5.6. Fiber bundles in population atlas.

give a reasonable approximation of tract geometry. No additional cleaning of the individual tracts was performed. This method potentially exaggerates the difference between atlas and individual tractography because obvious tract outliers were not removed in the individual tracts. Furthermore, due to manpower constraints, seeding ROIs were not manually selected in each individual. This validation study could be extended by expert manual seeding, clustering, and tractography parameter setting for each individual subject.

The results of individual tractography and tractography mapped from the atlas were then compared for each tract and subject. A summary of the mean and standard deviation of proposed measures over the population is presented in Tbl. 5.1. Table 5.2 gives a summary of the differences in scalar invariants sampled along these tracts. The binary overlap metrics are significantly lower than those typically encountered in segmentation studies. However, as mentioned in section 5.2.1, this is likely due to the thin shape of fiber bundles. The CP measure indicates that for most bundles, 90% of points in the atlas tract are within slightly about 1 voxel of the native space tract. This lends evidence that the atlas mapped tracts are in reasonable agreement with tracts produced by individual tractography. The ellipsoid measures are also within a relatively small range, further supporting the evidence of the CP measure. Functional measures showed the atlas tract to be about 10% lower for FA and 4% higher for MD. This difference may be due

Table 5.1. Mean and standard deviation of geometric distance measures between warped atlas tract and individual tract over the population.

Tract	BTO	CP_5	CP_9	ED_c	ED_ρ
fornix	0.46 (0.08)	0.60 (0.25)	2.55 (2.77)	5.19 (3.01)	0.68 (0.21)
uncinate-left	0.40 (0.07)	0.48 (0.13)	2.51 (2.27)	6.15 (3.77)	0.79 (0.09)
uncinate-right	0.48 (0.06)	0.49 (0.21)	2.00 (1.17)	4.56 (2.29)	0.77 (0.11)
cingulum-left	0.49 (0.04)	0.33 (0.04)	0.99 (0.22)	5.55 (3.12)	0.78 (0.07)
cingulum-right	0.50 (0.05)	0.31 (0.03)	0.97 (0.27)	5.59 (2.38)	0.77 (0.06)

Table 5.2. Mean and standard deviation of average absolute difference in FA and MD between atlas tract and warped individual tract. Percent differences are expressed as the ratio of the difference to the value from individual tractography.

Tract	FD_{FA}	$FD_{FA\%}$	FD_{MD}	$FD_{MD\%}$
fornix	0.07 (0.04)	16.40%	2.07e-04 (9.24e-05)	13.21%
uncinate-left	0.04 (0.01)	9.78%	3.58e-05 (1.38e-05)	3.98%
uncinate-right	0.03 (0.01)	8.41%	3.75e-05 (1.55e-05)	3.99%
cingulum-left	0.05 (0.02)	9.60%	3.21e-05 (1.24e-05)	3.68%
cingulum-right	0.05 (0.02)	9.62%	2.94e-05 (9.21e-06)	3.33%

to partial voluming effects combined with the use of taking the mean value at corresponding arc length values. The atlas tract often appears slightly larger than the individual tract and using the mean FA at each arc length point biases the atlas tract lower. The fornix showed greater differences than the other tracts, indicating that individual tractography does not consistently agree with the atlas for this tract. As no gold standard exists, further evaluation is needed to determine a preference for the atlas or individual tract.

5.4 Conclusion

This chapter presented a set of metrics that can be used to evaluate the similarity of tractography results. The application of these metrics here is the comparison of atlas-based tractography to tractography generated in the individual. A summary of some of the advantages and disadvantages of each measure is presented in Tbl. 5.3. Volumetric overlap proved to be hard to evaluate given that many tracts are narrow in at least 1 dimension, resulting in relatively low overlap measures

Table 5.3. Summary of measure advantages and disadvantages.

Measure	Advantages	Disadvantages
BTO	Similar to previous methods Compare streamline to volume	Unstable for thin tracts Lack of physical units
PC	Physical measures Robust to outliers	Requires parameter α
ED	Physical measures Robust to outliers	Simplified tract representation
FD	Error analysis of invariant statistics	Not a geometric measure

with even subvoxel differences in registration. The point cloud divergence served to be particularly useful because of the physical units involved, as well as resistant to outliers in unstable streamline tractography. Ellipsoid distance also provides a physical measurement of difference in tract location, size, and shape; the drawback is the simplification of the tract shape. Future work on the ellipsoid distance could decompose the difference into measures of frame difference, and scale changes of the ellipsoid in a common frame. Functional diffusion differences is a useful tool for evaluating variability of statistics but does not provide a geometric evaluation. Together, these methods can be used to improve quality control and validation of DTI analysis. Other uses of these metrics could include the comparison of different tractography routines, the evaluation of reproducibility on repeated scans of the same anatomy, and generation of variance measures to be used for power analysis for future clinical studies. Future work using an expert segmentation of individual tracts could further evaluate atlas based tractography. The measures presented here provide confidence that tracts mapped from the atlas provide a reasonable similarity to individual tractography and are appropriate as the basis for the tract-based statistics presented in the following chapter.

CHAPTER 6

TRACT STATISTICS

6.1 Introduction

The diffusion properties of white matter tracts measured by DTI provide a unique source of information for group comparison and regression in clinical neuroimaging studies. Previous work has shown the importance of modeling the diffusion properties of a fiber tract as a function sampled by arc length along the axis of the bundle [23, 35, 28]. The major challenge in implementing tract oriented statistics in population studies is finding a consistent spatial parametrization within and between populations. Defining anatomically equivalent ROIs to seed tractography for large population studies is time consuming, error prone, and often requires significant postprocessing such as cleaning and clustering [40]. Furthermore, even given tractography seeds for each image, the natural variability of brain size and shape prohibits a naturally consistent parametrization for arc length models of diffusion. To solve both the needs for tract segmentation in individual cases as well as shape normalization for fiber tracts, we apply a population-based registration method. Jones et al. [48] and Xu et al. [110] described the advantages of spatial normalization for DTI population studies. Recent work has focused on the use of unbiased methods for mapping tensor images to a common coordinate system [114, 82]. A reference atlas of fiber bundles visible in DTI was produced by [71]. Xu et al. [109] highlighted the need for smooth invertible mappings in a registration framework. Other work on DTI atlas building has used the geometry information contained within tractography results rather than image registration to build a population model [75]. In this framework, atlas building for DTI creates a global spatial normalization that can be used to parametrize tract oriented measures across a population.

This chapter combines the anatomically relevant coordinate system of tract statistics with the population coordinate system provided by atlas building. The combination of the tract coordinate system with atlas building provides an automated, clinically interpretable framework for understanding group differences. Furthermore, whereas most previous studies have analyzed tensor derived measures such as FA and MD independently, the method presented in this chapter enables the joint analysis of multiple tensor measures. In this method, deformable registration, as described in Chapter 4, is used to estimate and remove shape variability in a population of images. Analysis of shape normalized fiber bundles is performed in an anatomically relevant coordinate system defined by fiber tractography. The diffusion measures are treated as a continuous smooth function of arc length in atlas space, and statistical tests are applied for the joint analysis of the orthogonal measures FA and FRO. The framework provides a single multivariate hypothesis test between groups, eliminating the need for multiple comparison correction and incorporating the joint information of tensor anisotropy and size. Visualization of the linear discriminant provides a clinically meaningful interpretation of the group differences as shown in the example study of pediatric images.

6.2 Tract Oriented Statistics

After spatial normalization of tensor images, described in Chapter 4, diffusion measures across subjects can be compared. In previous work, this has been accomplished primarily through voxel-based tests that require sophisticated smoothing and multiple comparison correction. Although this type of analysis is effective for hypothesis generation, the results are often challenging to interpret, and strong group differences are necessary to overcome multiple comparison correction. I propose to use a semiparametric B-spline model of diffusion statistics along fiber bundles as the basis for group analysis.

Following previous work by Corouge et al., the diffusion properties of fiber tracts are modeled as smooth functions of arc length [23]. In this model, the diffusion data in a fiber bundle is reduced to a function of arc length for each tensor measure of

interest. As illustrated in Fig. 6.1, tensor measures in a bundle are averaged at each cross-section along the bundle to produce a function of arc length. In practice, this is achieved by manually placing a plane at a geometric or anatomical landmark of the fiber tract. The streamlines are then sampled at equivalent arc length distances from the origin and points with corresponding arc length are considered homologous. In our framework, template fiber bundles are computed in the tensor atlas using streamline tractography, and the improved signal-to-noise ratio of the atlas allows reliable extraction of fiber bundles. Furthermore, the origin for defining along tract correspondence is defined only once in the atlas space, significantly improving efficiency and repeatability of the analysis. The template fiber tract is warped back into the individual subject images to collect the diffusion data, as shown in Fig. 6.2. Because the geometry of the individual fiber bundles is identical in atlas space, the data for each subject are parametrized consistently. In the reduction of each tract to an arc length function, the exact same point geometry from the atlas is used, but varying diffusion measures are mapped from each subject, as shown in the right side of Fig. 6.2.

The analysis of diffusion properties focuses on invariant measures of tensor shape for two primary reasons. First, tensor orientation is an unstable measurement due to approximations of tensor reorientation during deformation. More important,

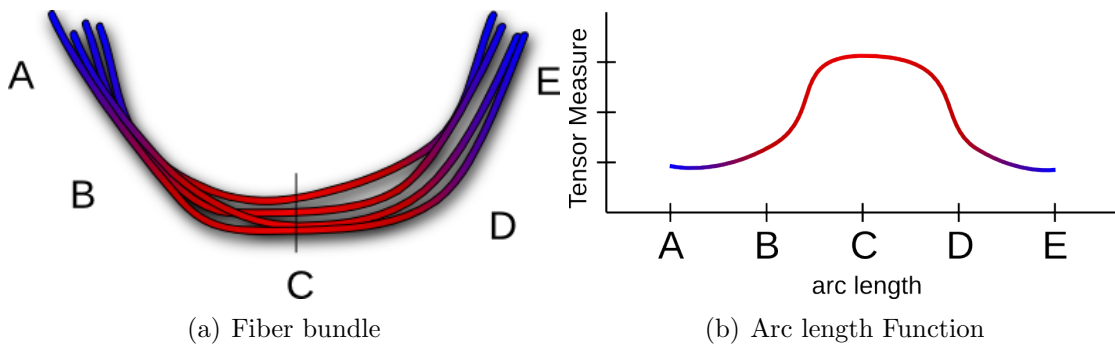


Figure 6.1. Diffusion properties within a fiber bundle (a) are summarized as a function of arc length (b). For example, the FA value along the cross-section at points A,B,C,D,E are averaged and become the value of the function at the points A,B,C,D,E along the x-axis of the arc length function.

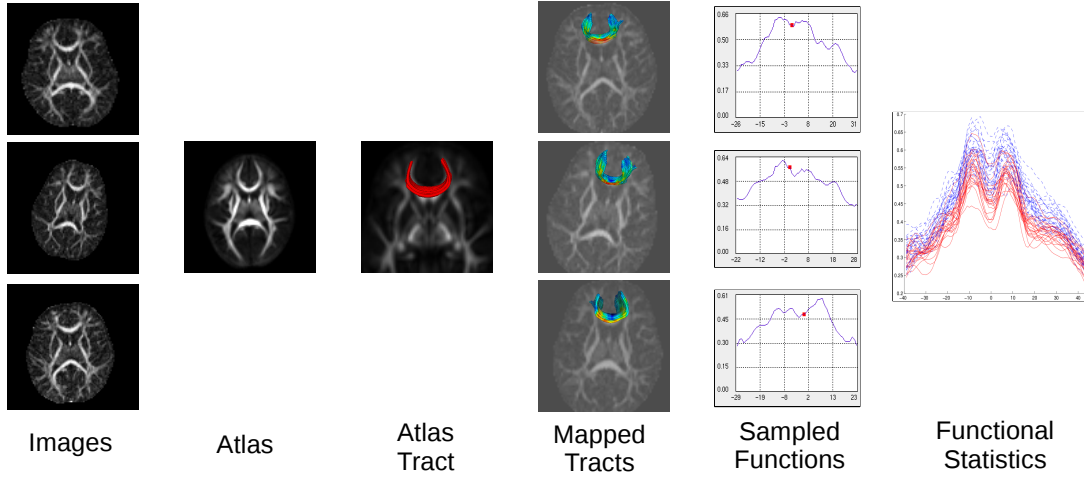


Figure 6.2. Schematic diagram of tract analysis procedure.

however, rotationally invariant measures such as anisotropy and MD have been linked to changes in tissue properties [17]. The most commonly used measurements of tensor shape are FA and MD. However, Ennis and Kindlmann showed that FA and MD are not orthogonal and therefore not appropriate for joint statistical analysis [30]. The nonorthogonality implies that differences in FA have different meanings depending on the magnitude of the MD. In this framework, FA is used as a measure of anisotropy because of its common usage in the literature. As a measure orthogonal to FA, the FRO of the tensor \mathbf{D} is chosen as a measure of the tensor size.

6.3 Functional Data Analysis

The population of multivariate functions produced by the fiber tract model requires a new method for statistical inference. Image sampling as well as the fiber tract extraction process create a sampled representation of the fiber bundle diffusion properties. However, there exists a continuous underlying biology that generates these samples. Therefore, statistical analysis of the sampled diffusion functions must account for the underlying continuity and spatial correlation of the samples. Statistics of the diffusion curves are computed as an infinite dimensional

extension to multivariate statistics known as functional data analysis [84].

The simplest extensions of ordinary statistics to the functional setting is the sample mean function $\bar{f}(t)$, parametrized by arc-length t for N samples, given by

$$\bar{f}(t) = \frac{1}{N} \sum_{i=1}^N f_i(t), \quad (6.1)$$

and the sample covariance function, which is the bivariate function parametrized by the two arc-length values s and t ,

$$v(s, t) = \frac{1}{N-1} \sum_{i=1}^N (f_i(s) - \bar{f}_i(s))(f_i(t) - \bar{f}_i(t))^T. \quad (6.2)$$

The diagonal of the function, $v(t, t)$, is the pointwise variance of the population of functions.

In this framework, the sample functions for statistics will be vector-valued functions resulting from the procedure described in the previous section. To be concrete, statistics are computed on the space of functions $\mathbf{f}(t)$ that map an arc length value t to a 2-element vector containing the FA and FRO. Similarly, the covariance function $\mathbf{v}(s, t)$ returns a 2×2 covariance matrix for every pair of parameters (s, t) .

Hypothesis testing and discriminant analysis in the space of continuous functions has an inherent high-dimension, low-sample-size problem because of the infinite-dimensional space of continuous functions. Regularization methods are, therefore, essential in the computation of functional statistics. To enforce regularity, B-spline fitting and functional principal component analysis (PCA) are used for data-driven smoothing, where the number of B-spline coefficients and retained PCA modes acts as a smoothing parameter.

In order to approximate the space of smooth functions, basis functions are fit to the sampled diffusion curves. B-splines were selected as basis functions due to the nonperiodic nature of the data, the compact support of the B-spline basis, and the ability to enforce derivative continuity. A large number of B-spline bases are first fit to the sampled functions using a least squares approach. Typically, the number of B-spline coefficients is chosen to be between 60% to 80% of the number of original samples. The number of basis functions is chosen empirically to maintain local

features while providing some smoothing. The mean function is computed by the sample mean of the B-spline coefficients. Computation of the variance-covariance function is more complex and requires accounting for the mapping between basis coefficients and function values. Let $\mathbf{f}_i(t)$ be the B-spline function fit to the samples from subject i . Following the notation of Ramsay and Silverman [84], in matrix form, we express all functions $\mathbf{f}_i(t)$ as a matrix of coefficients \mathbf{C} times the basis functions $\boldsymbol{\phi}$, so that

$$\mathbf{f}(t) = \mathbf{C}\boldsymbol{\phi}(t). \quad (6.3)$$

Assuming the functions are centered about the sample mean, the variance-covariance function of $\mathbf{f}(t)$ is

$$v(s, t) = \frac{1}{N-1} \boldsymbol{\phi}(s)^T \mathbf{C}^T \mathbf{C} \boldsymbol{\phi}(t). \quad (6.4)$$

Note that the vector-valued function $\mathbf{f}(t)$ gives a column vector for each value t , therefore computing the variance-covariance with respect to the arc length parameters s, t in (6.4) is transposed from the usual notation.

PCA of the functions $\mathbf{f}_i(t)$ decomposes $v(s, t)$ into the orthogonal unit eigenfunctions $\xi(t)$ that satisfy

$$\int v(s, t) \xi_i(t) dt = \lambda_i \xi_i(s). \quad (6.5)$$

Equation (6.5) can be solved numerically by rewriting in terms of the basis functions $\boldsymbol{\phi}$ with coefficients \mathbf{b} ,

$$\boldsymbol{\phi}(s)^T \mathbf{C}^T \mathbf{C} \boldsymbol{\phi}(t) \boldsymbol{\phi}(t)^T \mathbf{b} = \lambda \boldsymbol{\phi}(s)^T \mathbf{b}. \quad (6.6)$$

Let \mathbf{W} be a matrix of basis function inner products with entries

$$W_{ij} = \int \phi_i(t) \phi_j(t), \quad (6.7)$$

then equation (6.6) can be simplified in the matrix form,

$$\frac{1}{N-1} \mathbf{C}^T \mathbf{C} \mathbf{W} \mathbf{b} = \lambda \mathbf{b}. \quad (6.8)$$

The B-spline basis is not orthonormal, resulting in a nonsymmetric eigenvalue problem to solve (6.8). This system can be solved by the symmetric eigenvalue problem for the basis coefficients \mathbf{b} , with the change of variable $\mathbf{W}^{-1/2}\mathbf{u} = \mathbf{b}$:

$$\frac{1}{N-1}\mathbf{W}^{1/2}\mathbf{C}^T\mathbf{C}\mathbf{W}^{1/2}\mathbf{u} = \lambda\mathbf{u}. \quad (6.9)$$

Remember that this framework computes statistics of several diffusion measures jointly. Consider analysis of the vector-valued function, $\mathbf{f}(t)$ with basis coefficients \mathbf{C}_1 and \mathbf{C}_2 representing the FA and FRO values, respectively. The joint PCA is computed from the eigenanalysis of $\mathbf{\Sigma}$, where

$$\begin{aligned} \Sigma_{ij} &= \mathbf{W}^{1/2}\mathbf{C}_i^T\mathbf{C}_j\mathbf{W}^{1/2}, \text{ and} \\ \mathbf{\Sigma} &= \begin{bmatrix} \Sigma_{11} & \Sigma_{12} \\ \Sigma_{21} & \Sigma_{22} \end{bmatrix}. \end{aligned} \quad (6.10)$$

In practice, \mathbf{C}_1 and \mathbf{C}_2 are the same size because the same samples are used for both FA and FRO. Each vector-valued function $\mathbf{f}(t)$ is represented as a vector b containing the B-spline coefficients. b is organized with the parameters representing FA as the first half of the vector and the coefficients for FRO contained in the second half of the vector.

Hypothesis testing and discriminant analysis is performed on the projection of the data onto the first K PCA modes, where K serves as a smoothing parameter. The PCA projection accounts for the different scalings of the FA and FRO values enabling a joint analysis despite the differences in scale of the two values. An example of the PCA modes for the genu tracts from 1- and 2-year-old subjects is shown in Fig. 6.3. In this work, K is chosen to maintain 90% of the variability of the variance-covariance matrix. Let \mathbf{x}_i and \mathbf{y}_i be the projection of the curves from two populations of functions onto the PCA space. In this space, the basis mapping has already been incorporated and standard multivariate analysis can be applied. The normal parametric hypothesis test for mean differences between two multivariate normal populations is the Hotelling T^2 statistic,

$$T^2 = \frac{n_x n_y}{n_x + n_y} (\bar{\mathbf{x}} - \bar{\mathbf{y}}) \mathbf{S}^{-1} (\bar{\mathbf{x}} - \bar{\mathbf{y}})^T \quad (6.11)$$

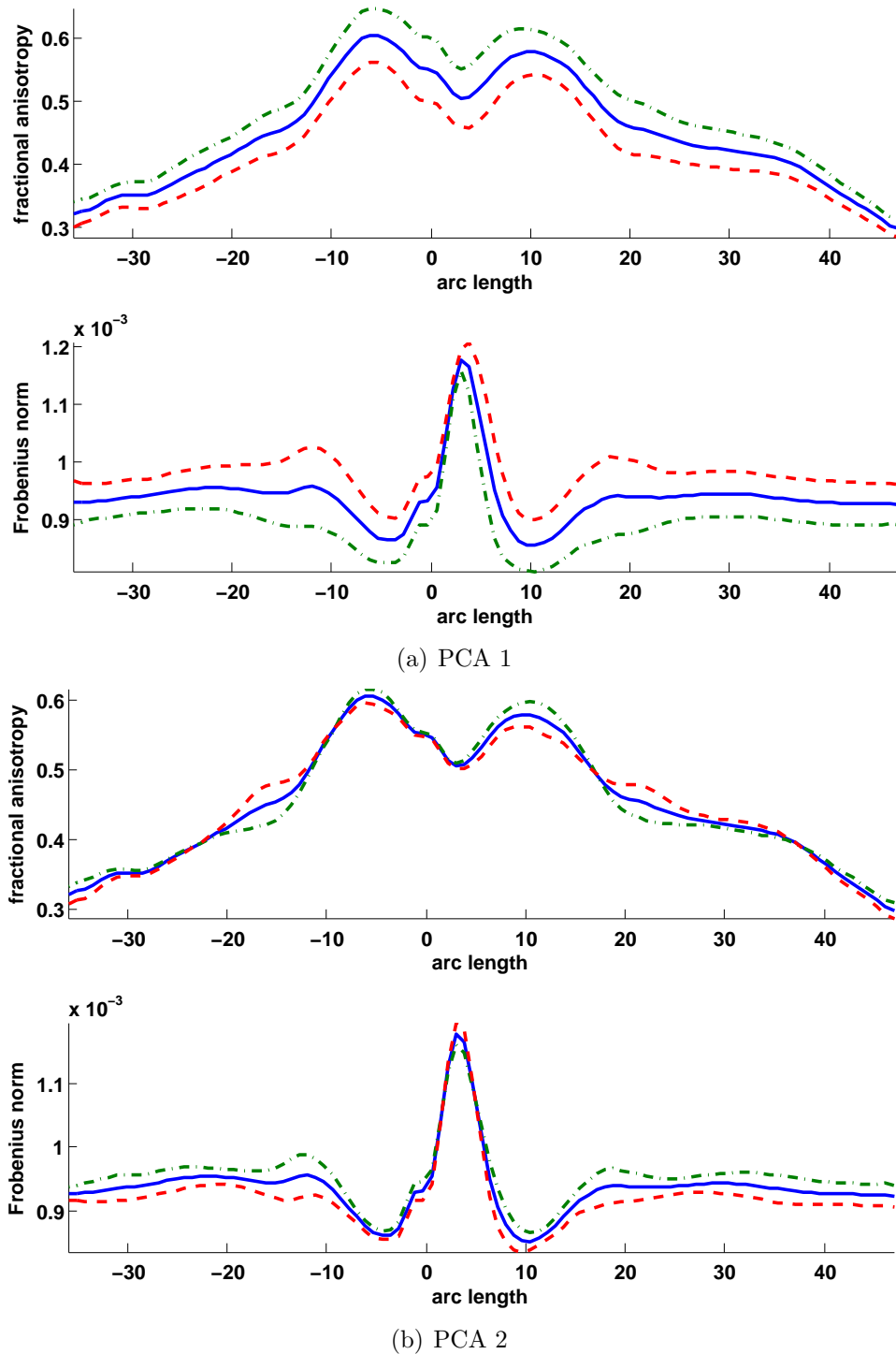


Figure 6.3. Visualization of the PCA modes for the joint analysis of FA and FRO in the genu of the corpus callosum for the 1- and 2-year-old populations. The (a) mean functions for the combined population are shown with (b) the 1st and (c) 2nd PCA modes. The 1st PCA mode accounts for a large percentage of the variability and shows constant changes of FA with an anticorrelated change in FRO.

where \mathbf{S} is the pooled covariance matrix given by,

$$\mathbf{S} = \frac{\sum_{i=1}^{n_x} (\mathbf{x}_i - \bar{\mathbf{x}})(\mathbf{x}_i - \bar{\mathbf{x}})^T + \sum_{i=1}^{n_y} (\mathbf{y}_i - \bar{\mathbf{y}})(\mathbf{y}_i - \bar{\mathbf{y}})^T}{n_x + n_y - 2} \quad [73]. \quad (6.12)$$

In order to relax the normality assumptions associated with the parametric test, we apply a random permutation test based on the T^2 statistic to compute p-values [74]. The permutation test is run on the multivariate T^2 statistic and does not require multiple comparison correction. A large number of random permutations are applied to the true group labels and the T^2 statistic is recomputed under the permutation. In experiments here, 100,000 random permutations were used. This generates a distribution that is compared to the original T^2 computed from the true labels. The random permutation test p-value is given by the percentage of permuted statistics that exceed the true statistic.

The T^2 statistic is proportional to the difference between group means projected onto the subspace given by the Fisher linear discriminant (FLD),

$$\boldsymbol{\omega} = \mathbf{S}^{-1}(\bar{\mathbf{x}} - \bar{\mathbf{y}})^T. \quad (6.13)$$

The linear discriminant, therefore, provides a direction for interpreting the detected group differences of the hypothesis test. The coefficients of the discriminant can be expanded into the original function basis so that $FLD(t) = \boldsymbol{\phi}(t)\boldsymbol{\omega}$ is a function whose inner product with the original data provides maximal separation between the groups. This function, $FLD(t)$, describes changes of tensor parameters between the two groups as a function of arc length.

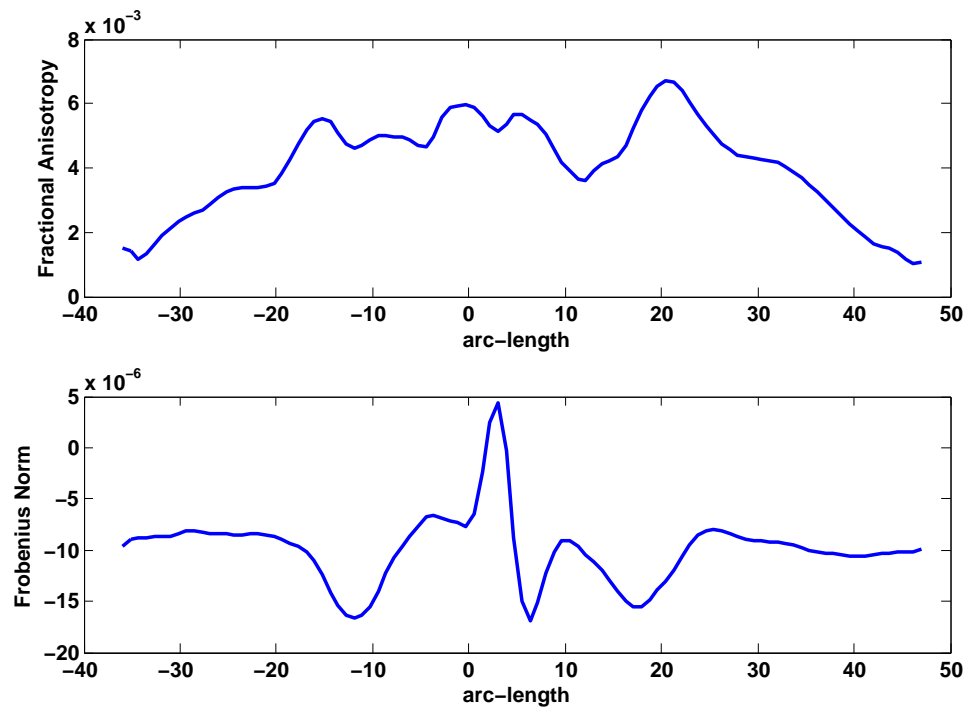
6.4 Example Results

The methodology presented in this chapter was tested on a study of pediatric DTI images. A brief sample of results are presented here with more detailed analysis available in section 7.2.2. A population of 22 1-year-old subjects and 30 2-year-old subjects were chosen from a database of pediatric DTI. In this example, a large group difference was expected, and the purpose of this study is to illustrate the methodology rather than to identify significant differences. Each image was acquired with $2 \times 2 \times 2 \text{ mm}^3$ isotropic voxels, 10 repetitions of the Basser gradient

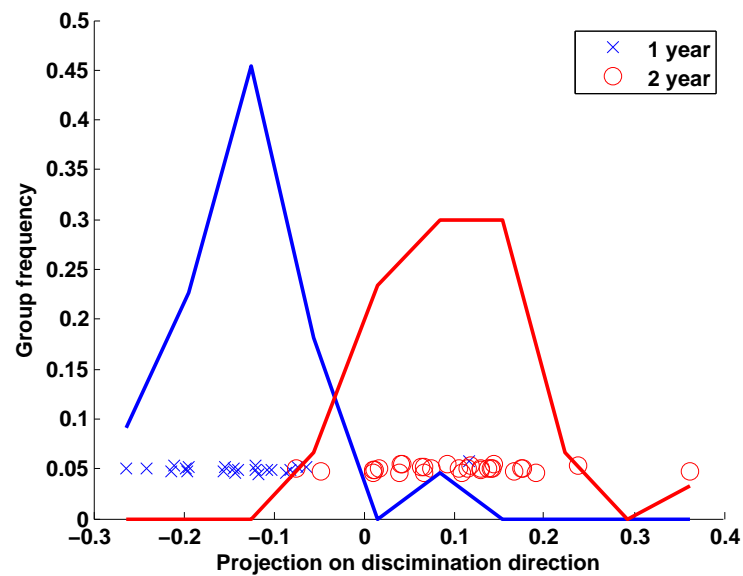
sequence, and a b-value of 1000. The genu of the corpus callosum and the left motor tract are presented as representative fiber bundles. An atlas was computed from the combined set of 52 images, and tractography was performed to extract the two tracts.

Sampled functions of FA and FRO were parametrized by atlas-normalized arc length in the genu and left motor tracts. For the genu curves, a B-spline basis with 60 basis functions was used to provide preliminary smoothing and smooth curve estimation. For the motor tract, 80 basis functions were used. Functional joint PCA of FA and FRO was then estimated for the whole population. The number of PCA modes was selected to retain 90% of the total variance. For this study, 7 and 11 PCA modes were retained for the genu and motor tracts, respectively. The mean function plus the first two principal modes for the genu tract are shown in Fig. 6.3.

The Hotelling T^2 statistic was then computed in the projected PCA space. The genu tract test was extremely significant with a T^2 statistic of 133.1 and parametric p-value of $3.3e-8$. The motor tract was also extremely significant with T^2 statistic of 93.8 and a parametric p-value of $2.7e-6$. In this case, there was such a large difference between groups that the permutation test did not result in any permutations with a statistic greater than the original. The p-values are uncommonly low because of the strong differences in the test data and the relatively large sample size. Visualization of the discriminant direction provides an interpretation of the detected differences and is shown in Fig. 6.4 and Fig. 6.5. The discrimination direction for the genu tract shows that the difference between the groups is primarily caused by an overall increase in FA and correlated decrease in FRO. Furthermore, the increased value of FA in the center of the tract indicates that the central region of the tract provides more discriminative power between the 2 groups. These results are similar to differences that have been found between neonates and 1-year-old subjects in the same tract [41]. The results in the motor tract indicate a similar constant increase in FA across the whole tract. The FRO increases towards the inferior region of the tract, and decreases at a specific location

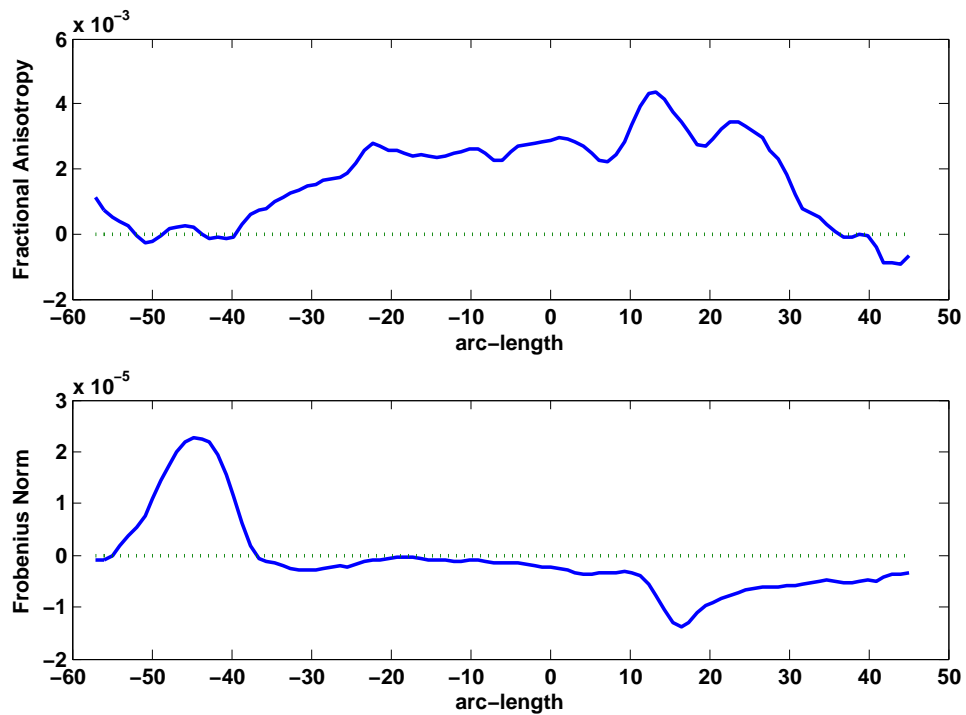


(a) Genu discriminant functions

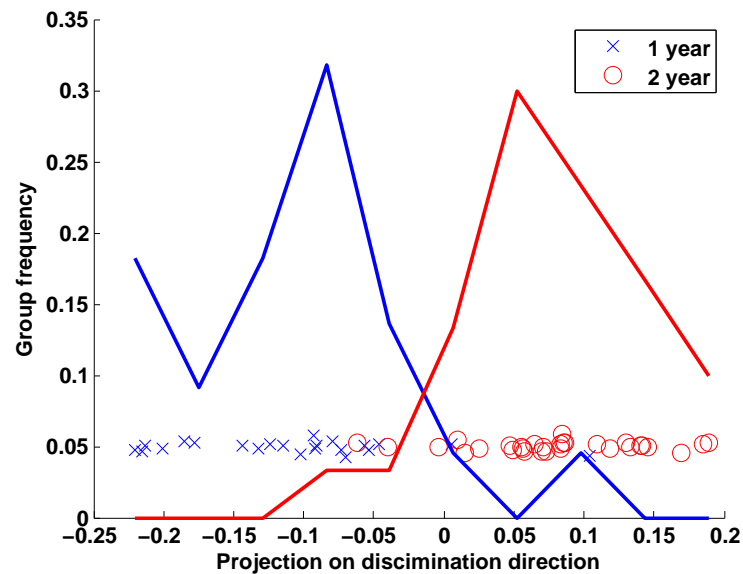


(b) Data functions projected on FLD

Figure 6.4. Discriminant for genu tract. (a) Linear discriminant between groups for the genu tract expanded into original functional basis with (b) projection of data on discriminant. In the genu tract the FA values increase between the groups, and the FRO values decrease. For the motor tract, the results are similar for FA, but the norm increases at the base of the tract and decreases towards the top.



(a) Motor tract discriminant functions



(b) Data functions projection on FLD

Figure 6.5. Discriminant for left motor tract. (a) Linear discriminant between groups for the left motor tract expanded into original functional basis with (b) projection of data on discriminant. In the left motor tract the FA values increase between the groups, and the FRO values decrease. For the motor tract, the results are similar for FA, but the norm increases at the base of the tract and decreases towards the top.

in the superior region of the tract. This decrease could be due to increased fiber crossing associated with development of the corpus callosum.

6.5 Conclusion

Computing fiber tract statistics as a function of arc length provides an intuitive mechanism for detecting and understanding changes in fiber tract properties between populations. This framework avoids the problems of multiple comparison correction by providing a single nonparametric hypothesis test for each fiber bundle. Furthermore, the discrimination information contained within the hypothesis test can be visualized to provide a clinically relevant interpretation of the group differences. The application of this method to different clinical problems is described in the following chapter.

CHAPTER 7

CLINICAL APPLICATIONS

7.1 Introduction

This chapter will cover the application of methods developed in the previous chapters to two clinical studies. The first study looks at the development of the brain in children from birth to 2 years, and the second study is focused on the study of schizophrenia in adults. Further background information on the two application areas was provided in section 1.3. A brief mention of additional applications not performed by the author are mentioned in section 8.3.

7.2 Study of Brain Development

Within the pediatric population, several different experiments have been explored within the framework of the analysis tools of this thesis. First, the atlas building procedure was applied to different age groups to estimate the development of diffusion measures with age. Although this experiment is not a rigorous quantification of changes, it provides a visualization of the difference in tensor measures with age. In addition, the tract specific methodology of Chapter 6 was applied to a group of 1- and 2-year-old subjects to measure tract specific development. Last, neonates within the database diagnosed with isolated prenatal mild ventriculomegaly (MVM) were compared to controls.

Pediatric data were obtained with institutional review board (IRB) approval from the University of North Carolina and Duke University Medical Center. Neonate subjects were scanned unsedated while sleeping. Subjects were imaged on a Siemens 3T Allegra scanner using a DTI protocol with 10 repetitions of a nondiffusion weighted image plus 6 diffusion weighted gradient directions using a b-value of $1000s/mm^2$ and a voxel size of $2 \times 2 mm^3$. Other imaging parameters are TR =

5200 ms and $TE = 73$ ms. After image acquisition, each repetition of the sequence was corrected for head motion by registration to the nondiffusion weighted images using the DTIchecker software¹.

7.2.1 Cross-Sectional Atlases of Development

Atlases were constructed for neonate, 1 year, 2 year, and adult populations to give an overall impression of the development of white matter structures with age. This test was not intended as a quantitative analysis. Instead, this serves primarily as a visualization of the existence of major fiber structures at birth and their maturation as reflected in changes of diffusion values.

For each age group, the data was processed using the methods described in Chapter 4. To bring the separate atlases into register, the RView software was used with an affine initialization followed by a B-spline registration [98, 86, 89]. In this experiment, the FA image of the atlas template for each age group was registered to the atlas for the 1 year group. The registration employed is insufficient for quantitative analysis but gives a reasonable visualization of the corresponding structures between the atlases. Axial slices from each of the registered atlases is shown in Fig. 7.1. Many of the major fiber structures such as the corpus callosum, internal capsule, and fornix can be seen in all of the age groups. Fibers in central tracts such as the internal capsule and corpus callosum have increased FA with age, indicating development of the white matter structure.

7.2.2 Normal Development From One to Two Years

The methodology presented in Chapter 6 was evaluated on a cross-sectional study of normal development, including subjects at one and two years of age. This study was chosen as a test case because of the expected large differences in diffusion properties due to development. In this case, the p-value of the hypothesis testing framework of Chapter 6 is less relevant as large changes are expected, but the discriminant direction provides localized information about major changes in

¹<http://www.ia.unc.edu/dev/download/dtichecker/index.htm>

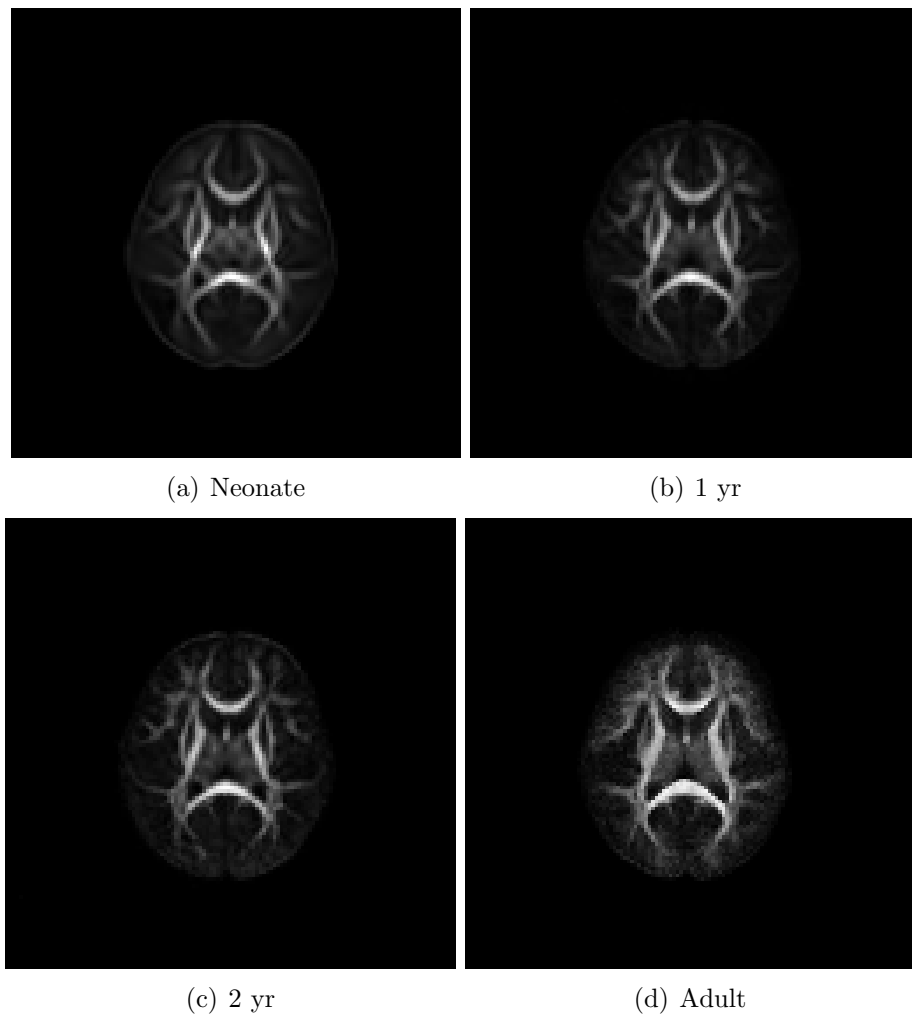


Figure 7.1. Axial slices of atlases at neonate, 1 year, 2 year, and adult.

diffusion properties between the two age groups.

The atlas building procedure of Chapter 4 was applied to a database of 49 healthy controls including 22 1-year-old subjects and 27 2-year-old subjects. The transformations were initialized to a template T2 atlas appropriate for pediatric images. The feature image for atlas building was computed with a Gaussian kernel width of $\sigma = 2.0mm$. Atlas building was performed in a multiresolution framework using two levels of downsampling. After registration, deformed tensor images were averaged to produce an atlas tensor image suitable for fiber tractography.

After registration and averaging, the atlas tensor image was used to identify four tracts of interest: genu, splenium, left cortico-spinal tract, and right cortico-spinal tract. Figure 7.2 shows axial slices of all the images deformed into atlas space. A streamline tractography algorithm using Runge-Kutta integration of the principal eigenvector field was used to extract the fiber tracts. Fibers were tracked from manually drawn seed regions in the atlas image and constrained to pass through a manually drawn target region. The atlas image provides improved SNR that allows lower FA thresholds than typically used for processing of single images. Figure 7.3 shows a comparison of the genu tract for one subject mapped from the atlas and the corresponding tract generated by tractography in the native space. In the entire population, the mapped tracts and individually computed tracts for the genu were mapped to binary voxel images. Dice coefficients were computed for each individual. The median dice coefficient for the cohort was .69, which is a reasonable overlap given the instability of streamline tractography methods. Previous work on comparing histology to fiber tractography has shown the difficulty in using dice coefficients and their dependence on the various parameters for tractography [25].

After generation of the atlas template tracts, data from the individual subject images were mapped to these tracts using the transformations created during atlas building. Tract oriented functions were computed for each subject using an origin defined in the atlas. Thirty B-spline control points evenly spaced in the arc-length parameter t were used to fit each function, and the resulting functions for the genu, splenium, and the left and right cortico-spinal tracts are shown in Fig. 7.4, Fig. 7.5,

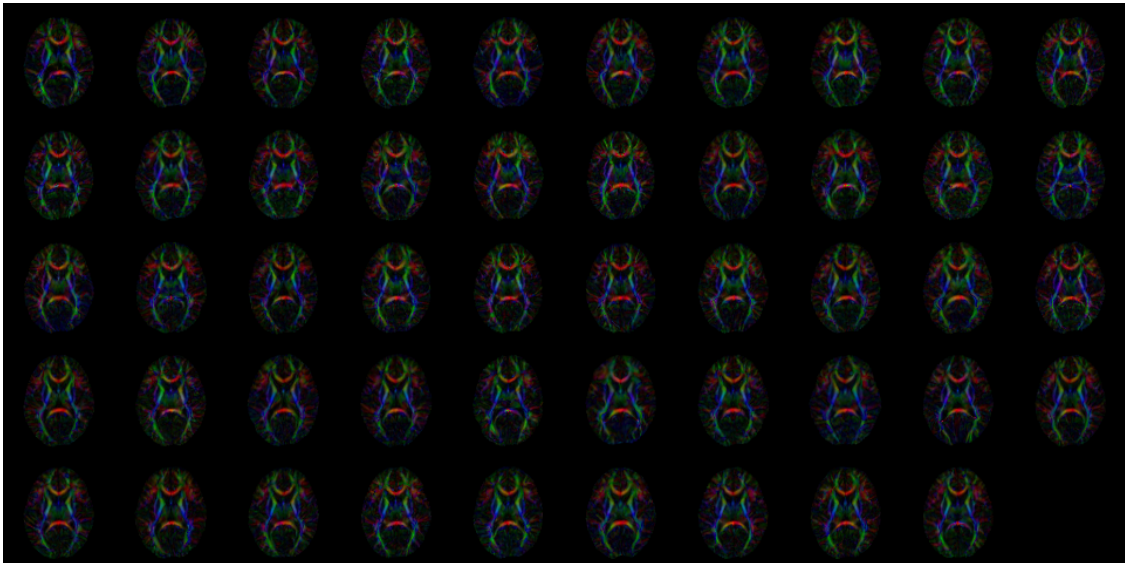


Figure 7.2. Axial slices of all subjects after nonlinear registration

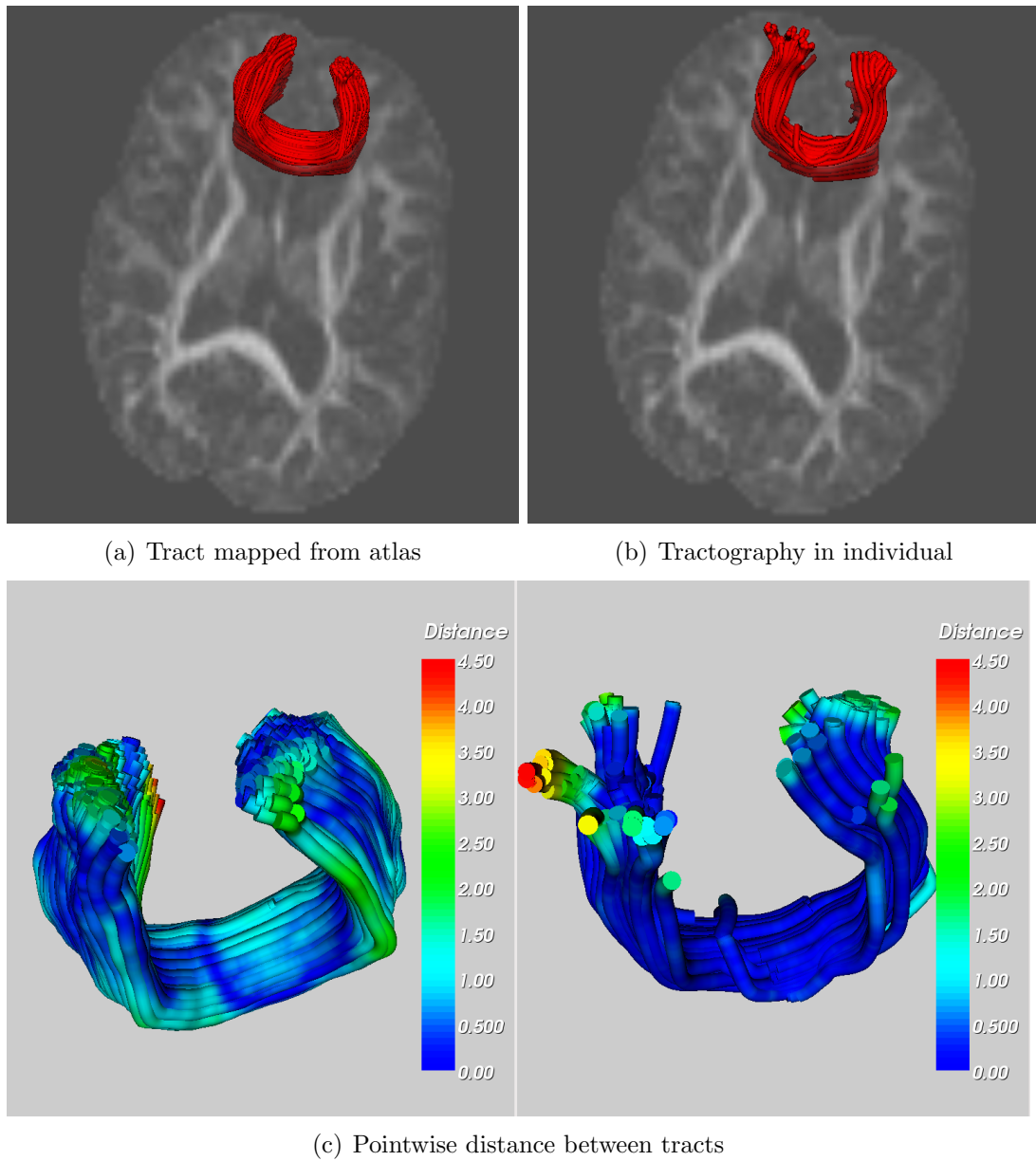


Figure 7.3. Comparison of atlas and individual tractography. The genu tract (a) mapped from atlas is compared with (b) the tract produced by tractography in the individual. (c) Comparison of pointwise distances between the two fiber tracts reveals a maximum difference of 4.5mm between the two tracts. The average distance in the main body of the tract is less than 1.5mm.

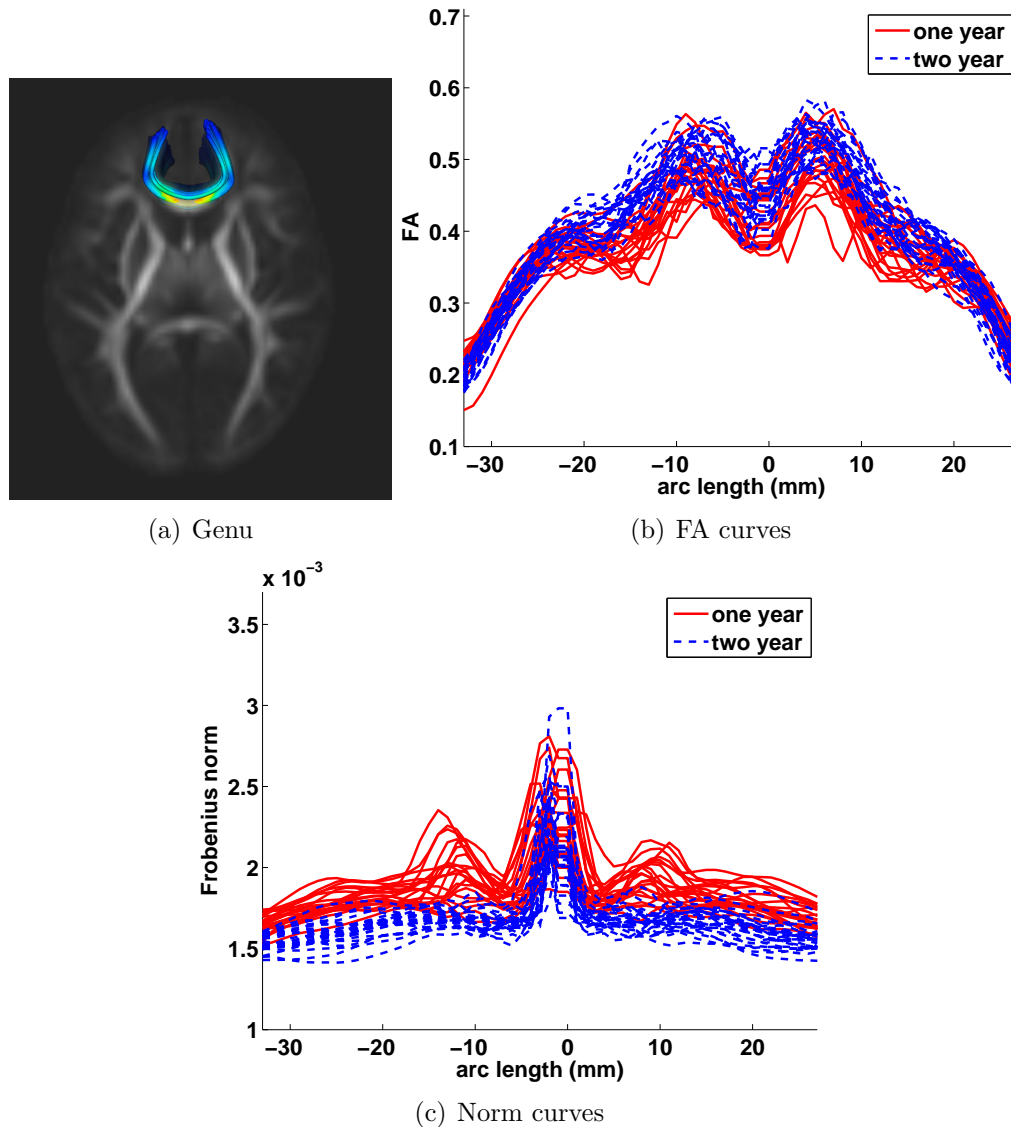


Figure 7.4. Tract and arc length functions for genu. (a) Genu tracts extracted from the tensor atlas shaded by mean FA value. The diffusion values are sampled along the atlas-normalized arc length for each individual in the study for FA and Frobenius norm values. The sampled FA and Frobenius norm functions for the two groups are shown in (b), (c). The 1-year-old subjects are the dashed lines and the 2-year-old subjects are the solid lines. The spikes in the center of the Frobenius norm functions for the genu are due to partial voluming with fluid in the longitudinal fissure.

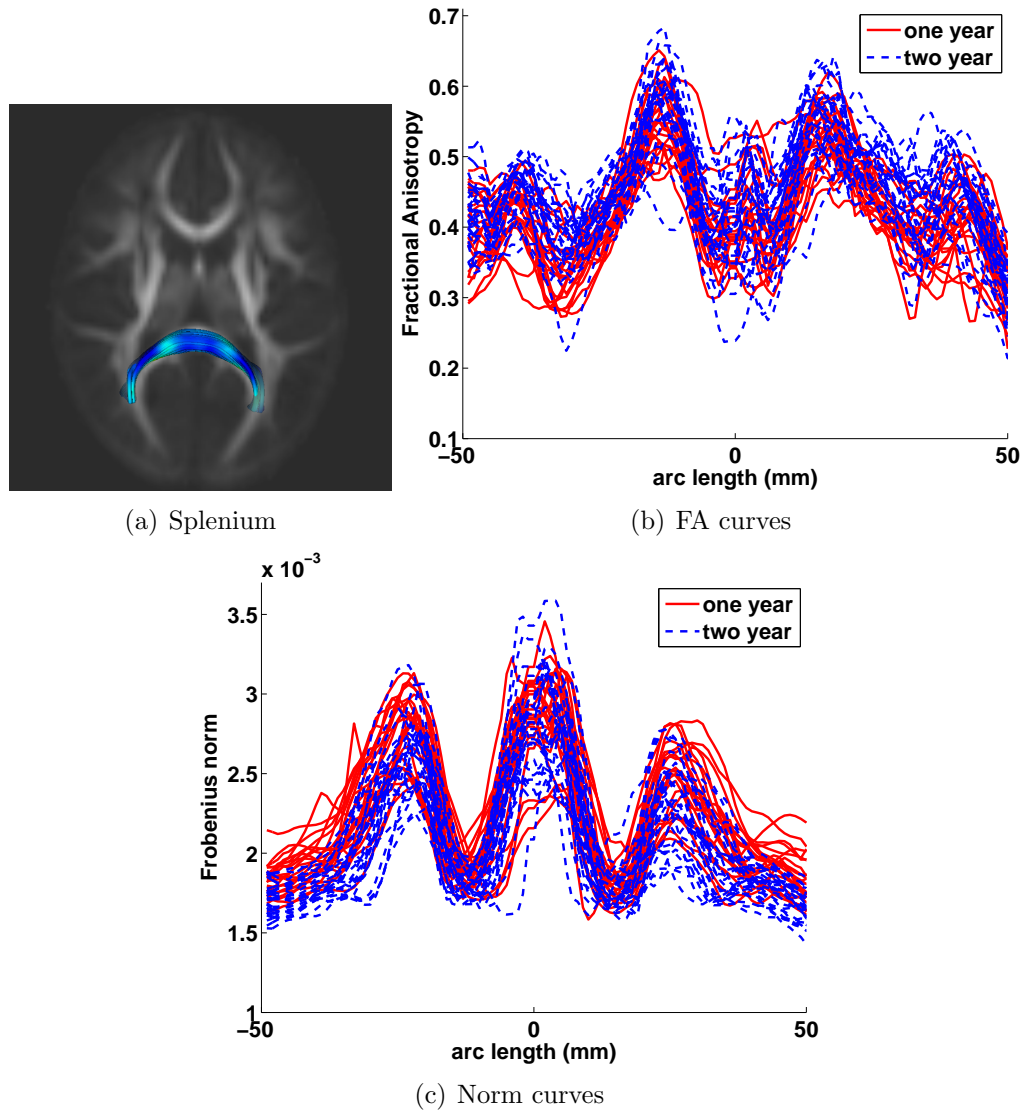


Figure 7.5. Tract and arc length functions for splenium. (a) Splenium tracts extracted from the tensor atlas shaded by mean FA value. The diffusion values are sampled along the atlas-normalized arc length for each individual in the study for FA and Frobenius norm values. The sampled FA and Frobenius norm functions for the 2 groups are shown in (b), (c). The 1-year-old subjects are the dashed lines and the 2-year-old subjects are the solid lines.

Fig. 7.6, and Fig. 7.7. After evaluation of the variance-covariance matrix for each tract, the number of PCA modes for the tract was selected to maintain 90% of the variance resulting in between 6–10 PCA modes per tract. Permutation testing over the Hotelling T^2 statistics was run for each tract with 100,000 permutations, and the FLD associated with the null permutation was computed for visualization. The resulting p-values as well as the maximum and average pointwise differences of diffusion measures between groups along the tract are summarized in Tbl. 7.1. All the tracts indicate a general trend of increase in FA and a correlated decrease in Frobenius norm from 1- to 2-year-old groups. Figure 7.8 shows a visualization of the discriminant function for the genu tract that indicates an increase in FA and a correlated decrease in Frobenius norm from the 1- to 2-year-old groups with the effect focused in the center of the tract and trailing off as the tract enters the grey matter regions of the cortex. In the cortico-spinal tracts, there is some evidence of localized changes. Figure 7.9 shows the mean functions for the two groups and the discriminant direction. The discriminant indicates that FA increases from one to two years in regions of the tract inferior of the callosal fibers, whereas the FA decreases in regions at the callosal fibers and above. This localized change could indicate a possible increase in orientation complexity or crossing fibers during development.

7.2.3 Hypothesis Testing Between Controls and MVMs in Neonates

Prenatal MVM is a condition characterized by enlargement of the lateral ventricles diagnosed by ultrasound and has been associated with increased risk of neuropsychiatric disorders [42]. Previous investigation of DTI quantities in MVM have found a significant decrease in FA from controls in manually identified regions of splenium as well as significant increase in MD in regions of the genu, splenium, and cortico-spinal tracts [41].

The atlas building method described in Chapter 4 was applied to a database of 114 images including 85 controls, 13 MVMs, 12 offsprings of schizophrenics, and 4 offsprings of bipolar. Future work will study the different groups within

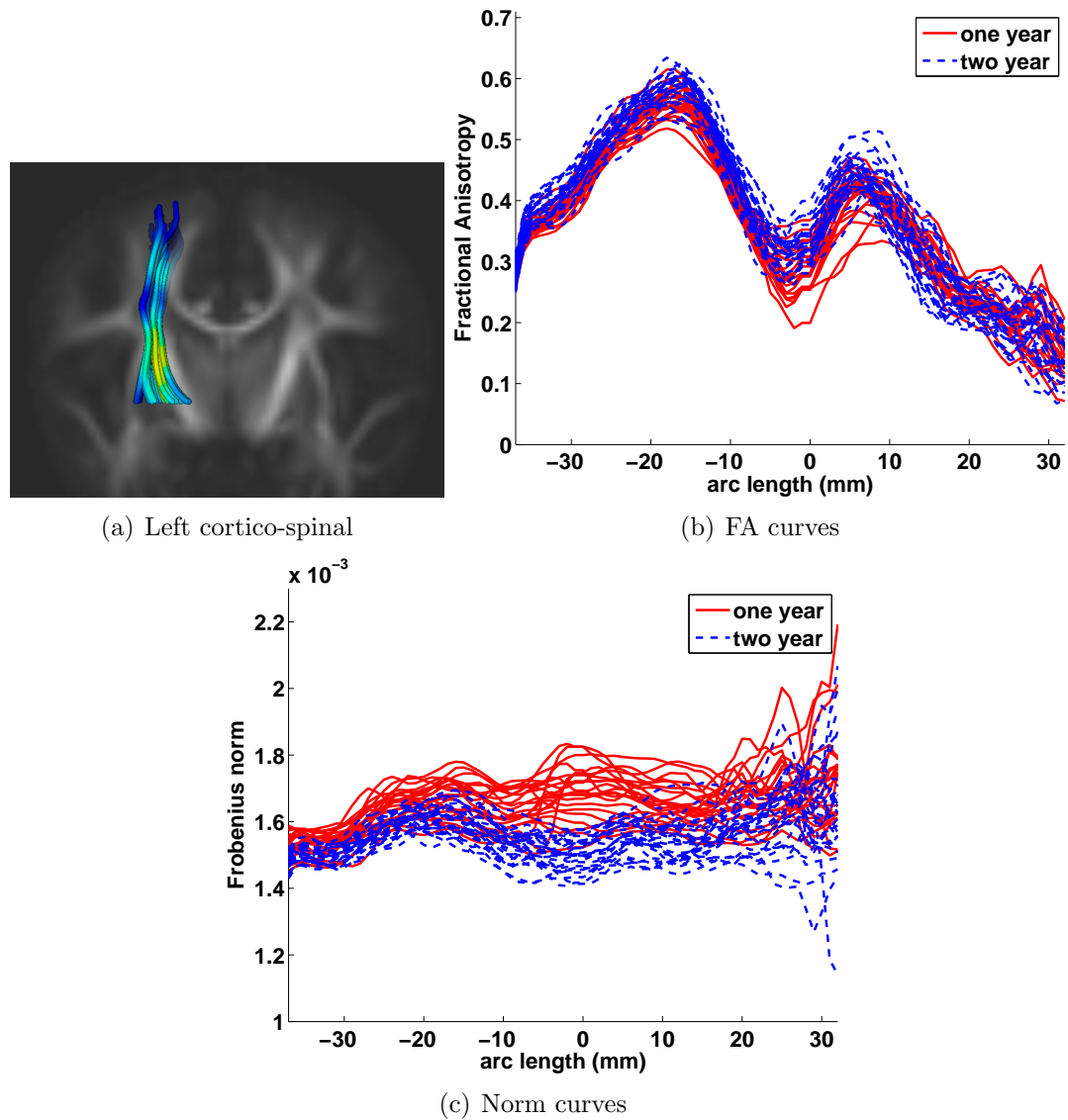


Figure 7.6. Tract and arc length functions for left cortico-spinal tract. (a) Left cortico-spinal tracts, cropped in the internal capsule, in the 1- and 2-year-old population. The tracts are sampled from inferior to superior along the tract to produce the sampled functions in (b) and (c).

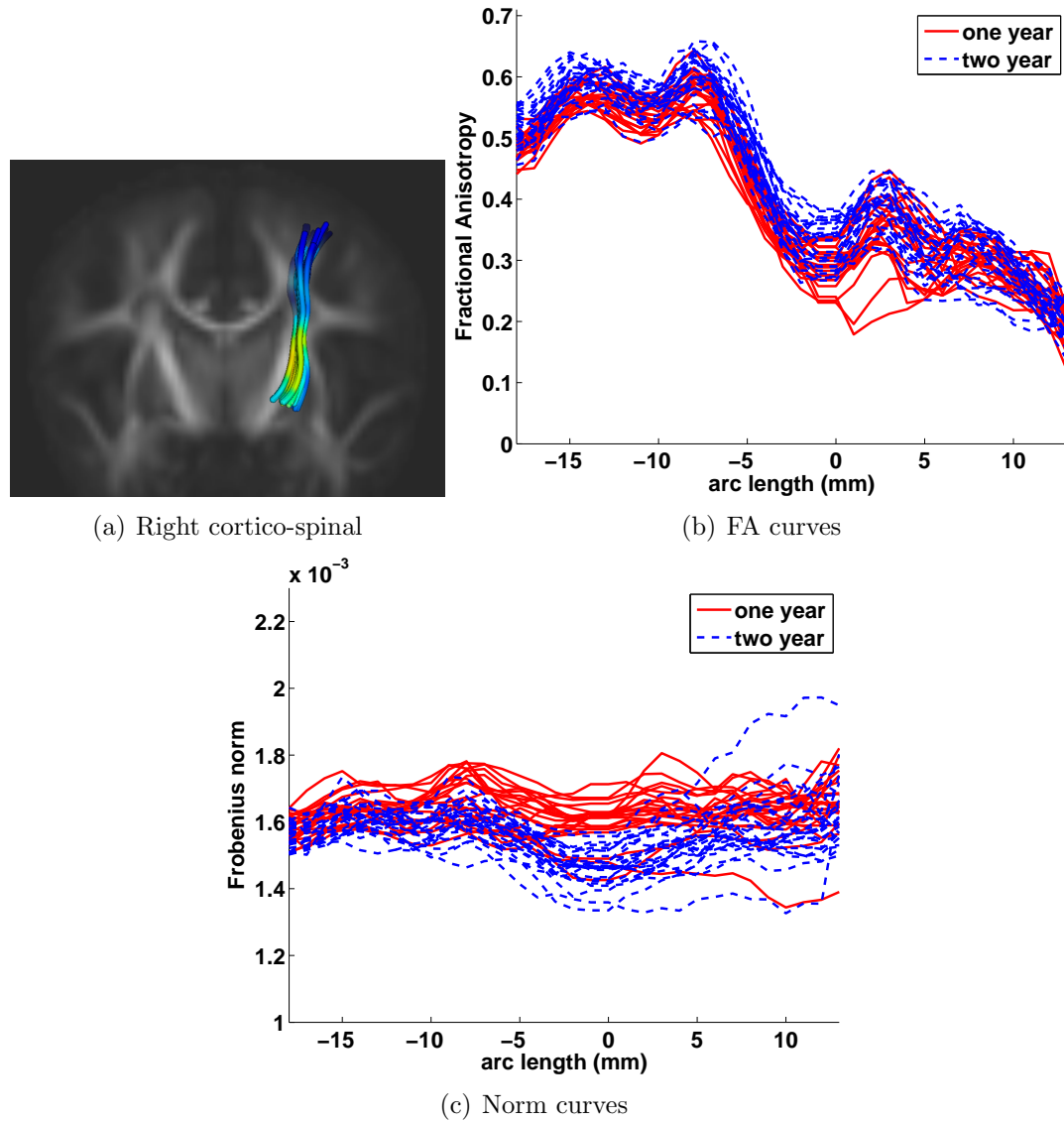


Figure 7.7. Tract and arc length functions for right cortico-spinal tract. (a) right cortico-spinal tract, cropped in the internal capsule, in the 1- and 2-year-old population. The tracts are sampled from inferior to superior along the tract to produce the sampled functions in (b) and (c).

Table 7.1. Tract differences from one to two years

Tract	p-value	FA		Frobenius norm	
		max	avg	max	avg
Genu	<.0001	.060	.020	-2.9×10^{-4}	-1.8×10^{-4}
Splenium	.0024	.053	.022	-2.6×10^{-4}	-1.4×10^{-4}
Left cortico-spinal	.0004	.036	.014	-1.9×10^{-4}	-0.9×10^{-4}
Right cortico-spinal	.0002	.049	.023	-1.3×10^{-4}	-0.7×10^{-4}

The table provides p-values for the hypothesis test of differences between 1- and 2-year-old subjects. Columns 3–4 and 5–6 show the maximum and average pointwise differences between the mean functions of the two groups.

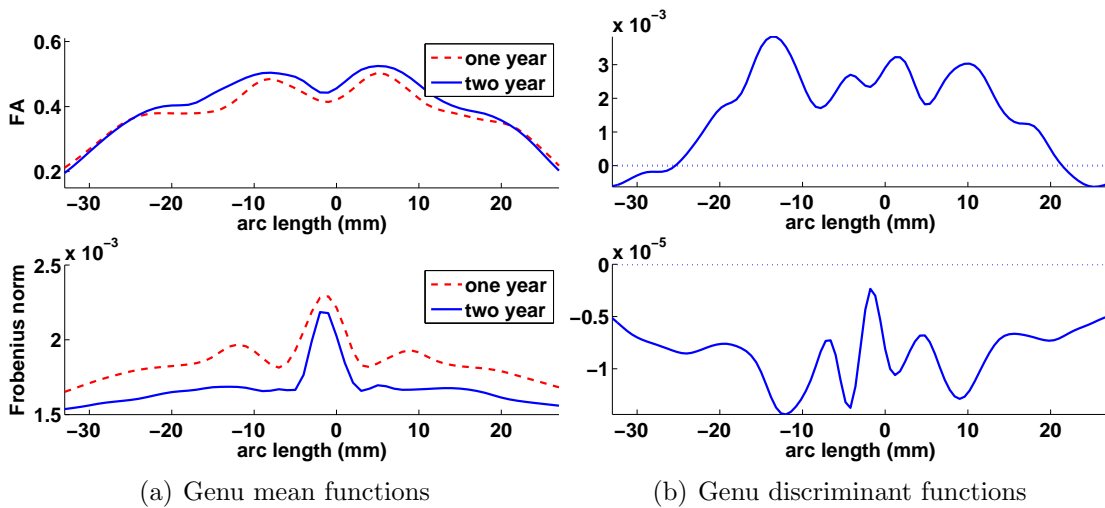


Figure 7.8. Discriminant function for the genu tract. (a) The mean functions for the genu tract 1- and 2-year-old groups along with (b) the linear discriminant that describes the function that maximizes separation between the groups. Here, the FA values increase from 1 to 2 years, and the Frobenius norm values decrease in a correlated manner. The FA changes are localized towards the center of the tract and are less informative at both the left and right ends of the tract.

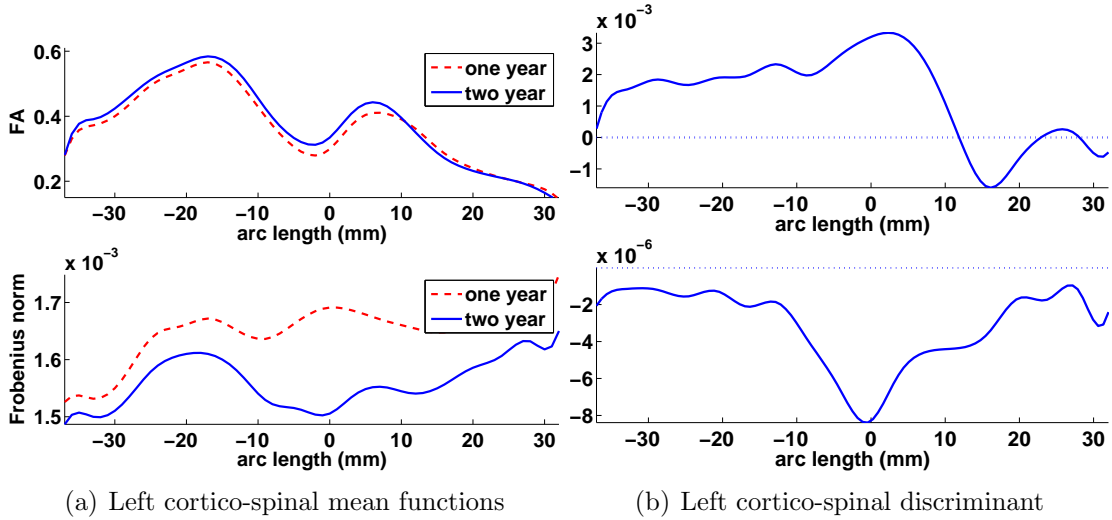


Figure 7.9. Discrimination function left cortico-spinal tract. (a) The mean functions of the left cortico-spinal tract for the 1- and 2-year-old groups along with (b) the linear discriminant which describes the function that maximizes separation between the groups. Here, FA increases in regions inferior of the callosal fibers and decreases as the tract passes near the corpus callosum. This could indicate increased interaction and crossing between fibers in this region.

this database, but this study focuses on the comparison of MVMs to controls. Transformations were initialized to a neonate specific template with T2 weighting. The feature image was computed at $\sigma = 1.5mm$ for each subject, and the atlas building procedure was applied in a multiresolution framework. After diffeomorphic registration of each tensor image, an atlas tensor image was created by averaging the deformed images. In the atlas tensor image, tracts were computed for the genu, splenium, and left and right cortico-spinal tract, as shown in Fig. 7.10.

Analysis of tracts was performed on the left and right cortico-spinal tracts, genu, and splenium. Statistically significant differences were found in the splenium tract but not the genu or cortico-spinal tracts. Figure 7.11 shows the discriminant direction for the splenium tract and indicates a decrease in FA and a correlated increase in Frobenius norm from control subjects to those with MVM. Results for all analyzed tracts are summarized in Tbl. 7.2.

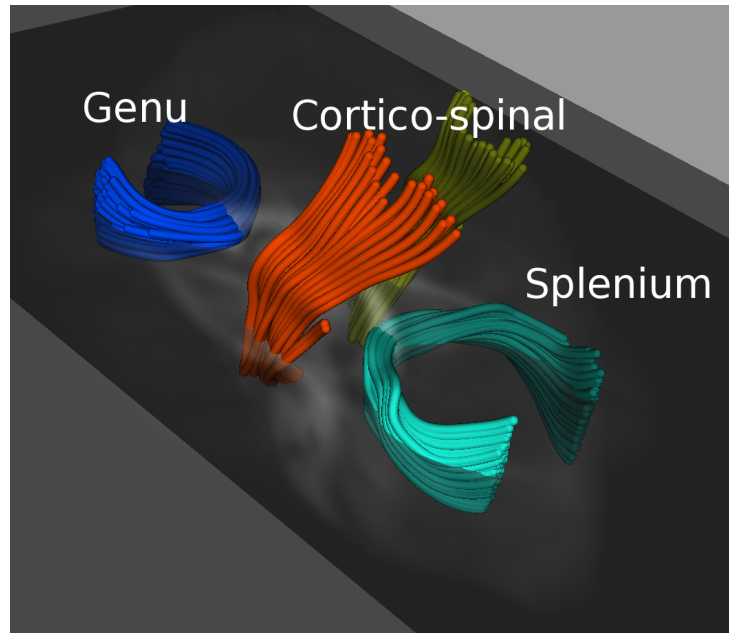


Figure 7.10. Template fiber tracts in atlas of neonate subjects overlaid on the FA image of the neonate atlas.

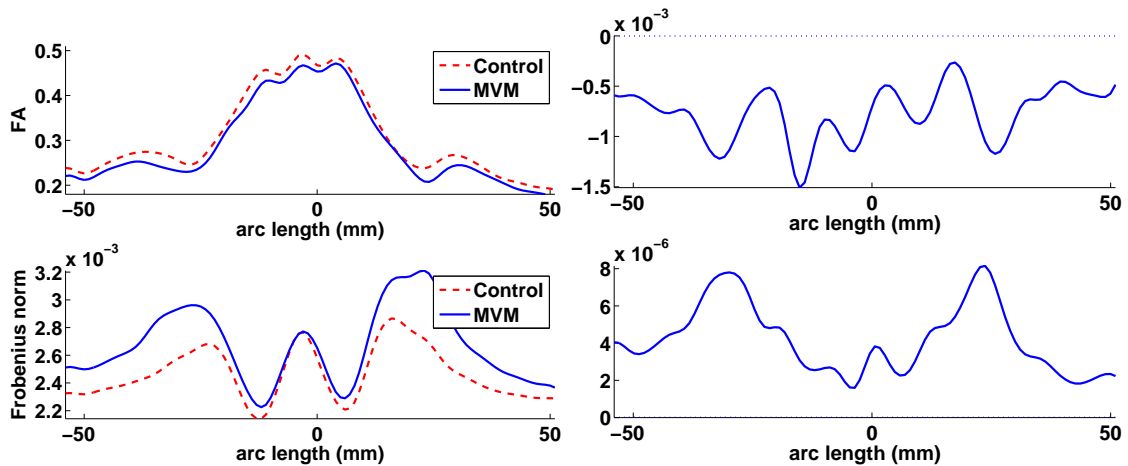


Figure 7.11. Discriminant for splenium from control to MVM groups. (a) The mean functions for the splenium tract in control and MVM neonates are shown along with the (b) Fisher linear discriminant. The discriminant indicates that the significant differences in tract properties are attributed to a decrease in FA and an increase in Frobenius norm in MVMs.

Table 7.2. Tract differences from neonate controls to MVMs

Tract	p-value	FA		Frobenius norm	
		max	avg	max	avg
Genu	.99	.0086	.0020	1.1×10^{-4}	0.32×10^{-4}
Splenium	.0001	.039	-.019	5.7×10^{-4}	2.1×10^{-4}
Left cortico-spinal	.24	.016	.00015	1.5×10^{-4}	-0.6×10^{-4}
Right cortico-spinal	.80	.022	.0034	8.8×10^{-5}	-2.6×10^{-5}

The table provides p-values for the hypothesis test of differences between controls and MVMs. Columns 3–4 and 5–6 show the maximum and average pointwise differences between the mean functions of the two groups.

7.3 Schizophrenia

The tract analysis method was applied to a study of schizophrenia in adults to test for possible tract differences. Data for this study were provided by Marek Kubicki at Brigham and Womens Hospital. An atlas was built from images of 37 subjects in a study of schizophrenia in adults. Each subject was imaged using a protocol with 8 nondiffusion weighted images and 51 diffusion weighted gradients at a voxel resolution of $1.6667 \times 1.6667 \times 1.7 \text{ mm}^3$. A b-value of 900 was used for the diffusion weighted images. After atlas building, the fornix, left and right uncinate, and left and right cingulum were extracted. Visualization of the fiber tracts is shown in Fig. 7.12. Permutation tests for each of the tracts revealed no significant differences at the $\alpha = .05$ significance level. Visualisation of the individual tracts as well as the discriminant function are shown in Fig. 7.13, Fig. 7.14, Fig. 7.15, Fig. 7.16, and Fig. 7.17.

7.4 Conclusion

The methods presented in this thesis have been applied to several different clinical studies, including a study of neurodevelopment and schizophrenia in adults. The use of the methodology in a variety of studies at different institution demonstrates that the framework of this thesis is a generic tool for investigating white matter changes in neuroscience studies. The results of the development studies confirmed previous findings of changes due to age and may provide a tool for investigating these changes in more detail. The results of the schizophrenia study

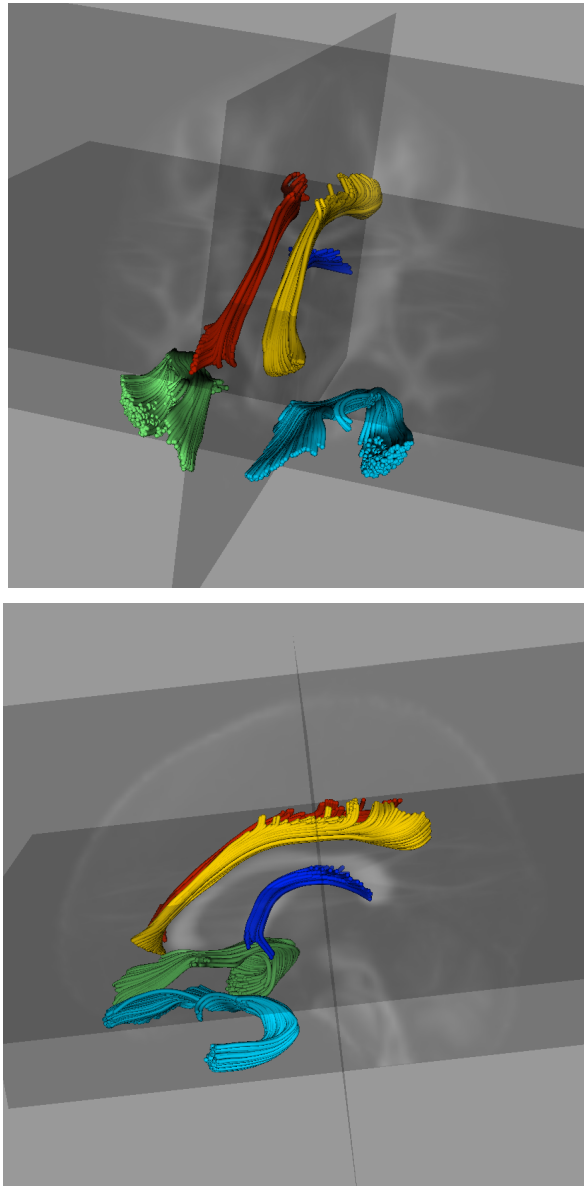


Figure 7.12. Fiber bundles for analysis of schizophrenia data.

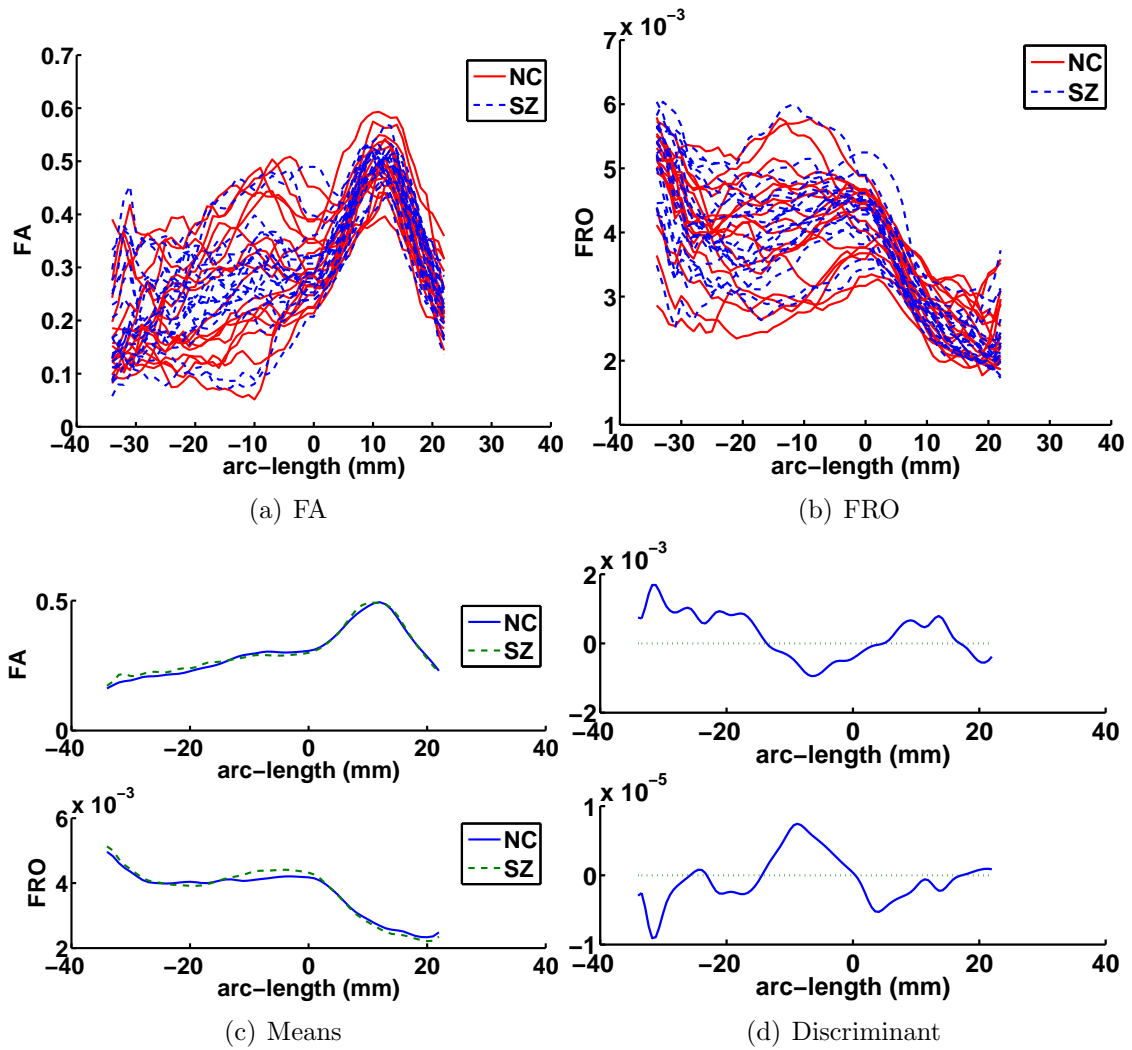


Figure 7.13. Functions and discriminant for fornix. (a) and (b) show the FA and FRO functions for both populations. (c) shows the mean of each population, and (d) shows the discriminant function.

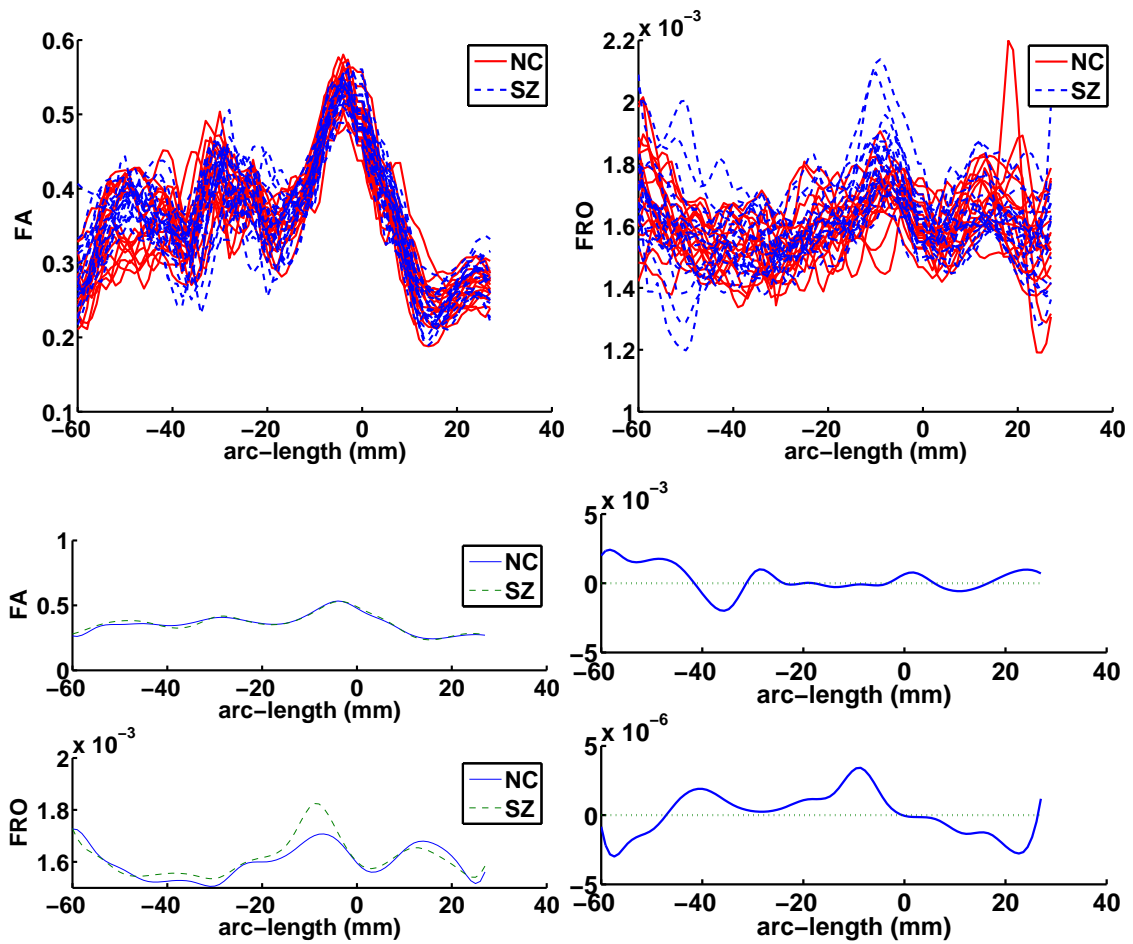


Figure 7.14. Functions and discriminant for left uncinete. (a) and (b) show the FA and FRO functions for both populations. (c) shows the mean of each population, and (d) shows the discriminant function.

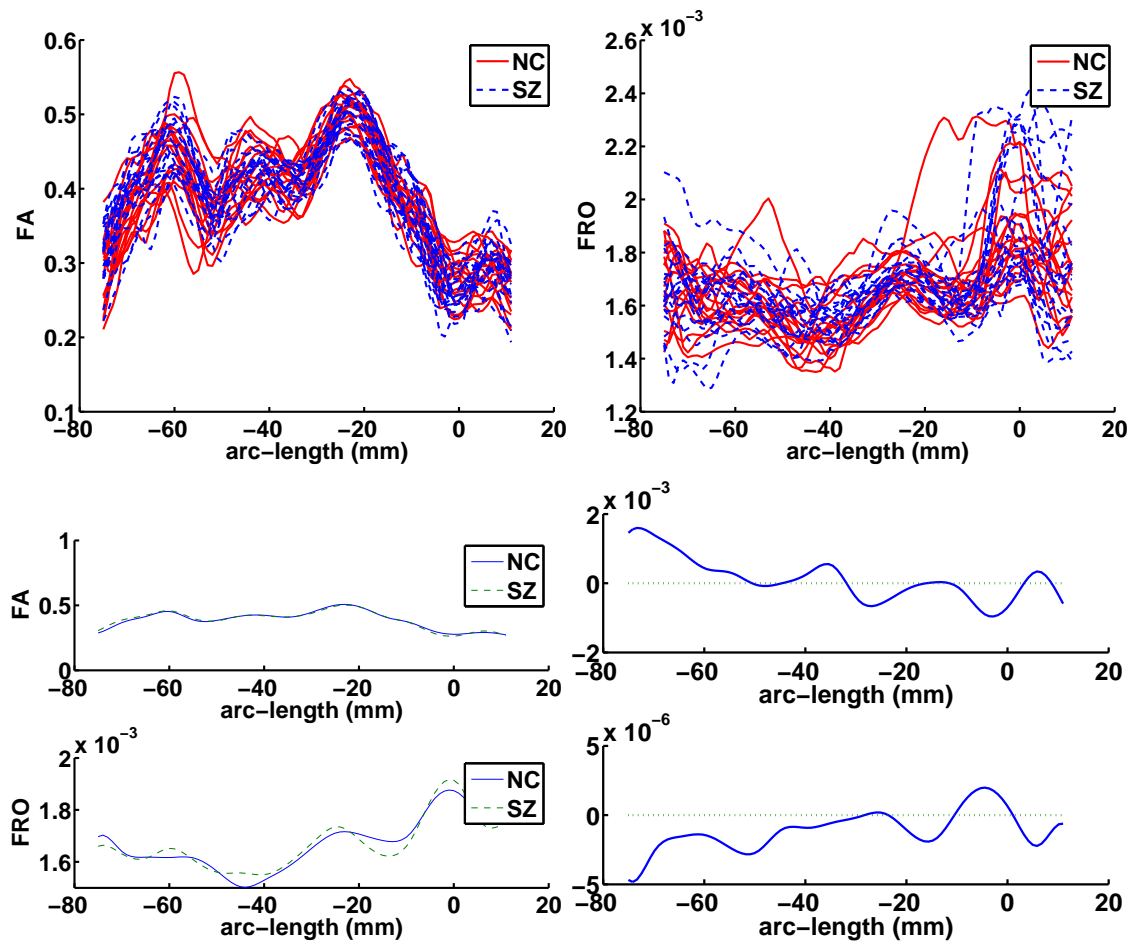


Figure 7.15. Functions and discriminant for right uncinate. (a) and (b) show the FA and FRO functions for both populations. (c) shows the mean of each population, and (d) shows the discriminant function.

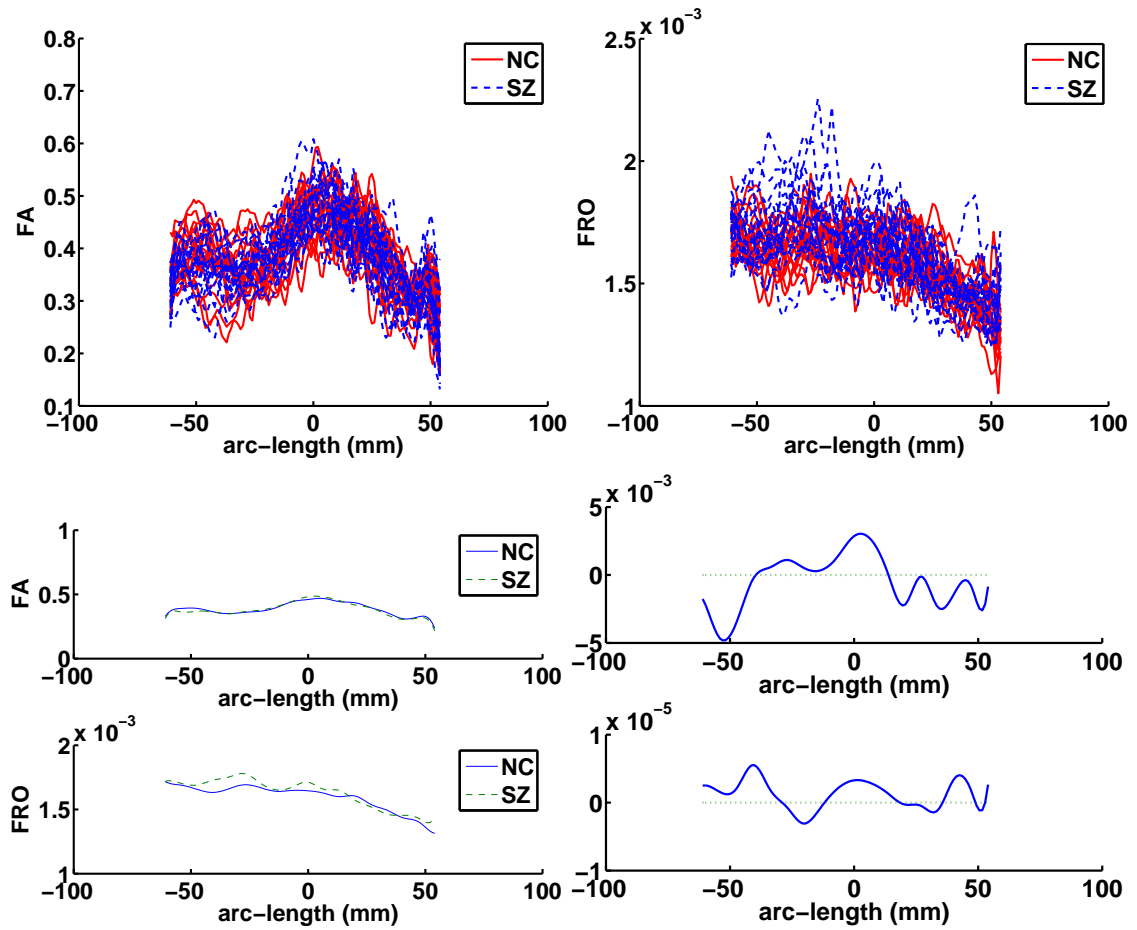


Figure 7.16. Functions and discriminant for left cingulum. (a) and (b) show the FA and FRO functions for both populations. (c) shows the mean of each population, and (d) shows the discriminant function.

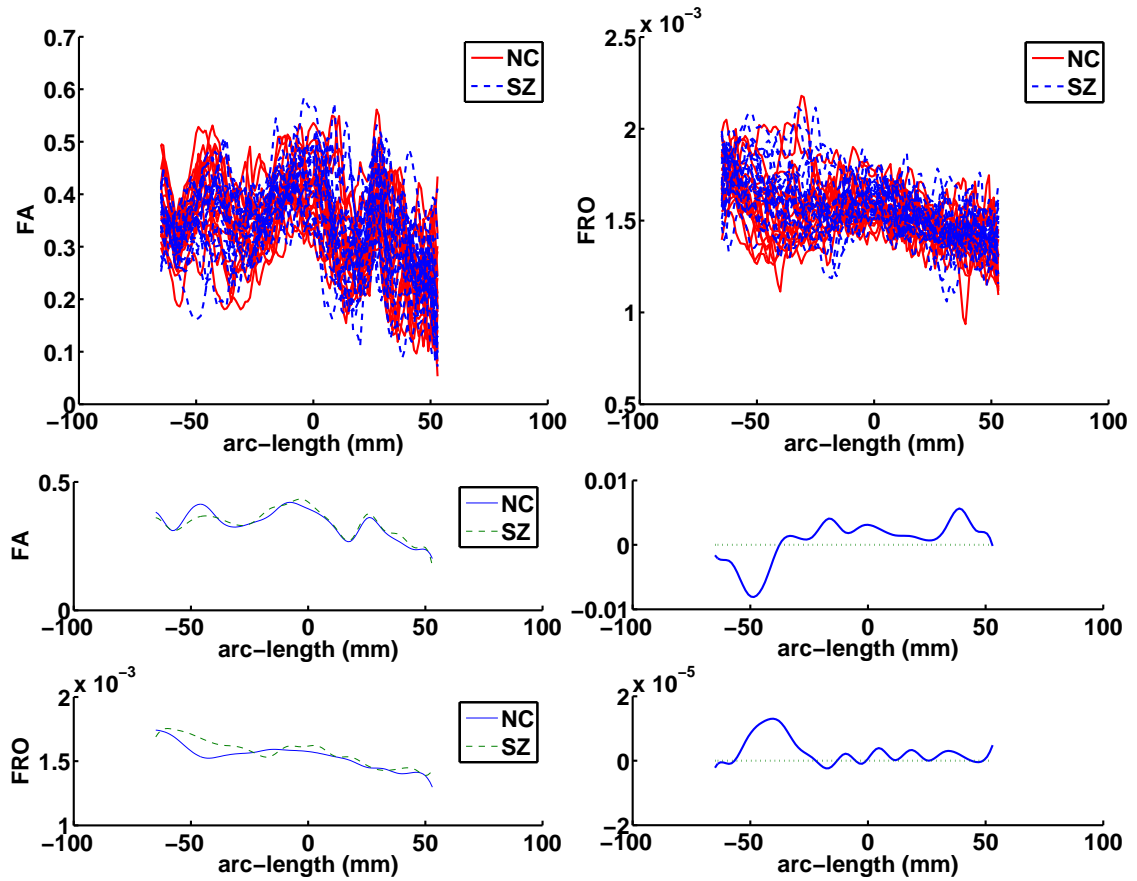


Figure 7.17. Functions and discriminant for right cingulum. (a) and (b) show the FA and FRO functions for both populations. (c) shows the mean of each population, and (d) shows the discriminant function.

are inconclusive with no differences found in this study. Future development of the statistical analysis to perform regression and account for covariates may be necessary to investigate this study in more detail.

CHAPTER 8

DISCUSSION

8.1 Summary of Contributions

This section summarizes the contributions listed in section 1.4 and developed throughout the chapters of this thesis.

1. *An analysis of diffusion tensor estimation under different acquisition schemes illustrates the bias introduced by gradient sampling schemes with repeated directions.*

Chapter 3 reviewed the source and distribution of noise in MRI. Simulation of the noise and its effect on various measures of the estimated tensors showed deficiencies in gradient sampling schemes relying on averaging of repeated directions and suggests the use of nonrepeated sampling of gradient directions. A method to improve retrospective analysis with ML estimation is also presented. A novel experiment on repeated acquisition of real images supports the results of the simulation.

2. *An analysis of diffusion tensor estimation methods shows a preference towards weighted least squares tensor estimation to achieve efficient computation with reduced bias and variability of derived tensor measures.*

A review of published methods for diffusion tensor estimation was presented in Chapter 3. A comparison of the different methods was performed using several different gradient acquisition schemes. This result extended the previous contribution by showing that weighted least squares or maximum likelihood estimation are needed to take full advantage of the recommended gradient sampling schemes.

3. *A method for spatial normalization of tensor images based on unbiased atlas building allows populations of tensor images to be analyzed in a common*

coordinate frame.

Chapter 4 extended a previous atlas building method by developing a scalar feature image sensitive to the medial structure of brain white matter. Experiments on populations, especially as presented in section 7.2.1, demonstrated ability of this method to produce atlas images representative of the population. Fiber tracts extracted from this atlas are used in the analysis method of Chapter 6. A user manual for the atlas building procedure is listed in Appendix A. This method has also been used for other studies not covered in this thesis. A sample of these other applications is presented in section 8.3 of this chapter.

4. *Measures for evaluating geometric and functional differences in tractography are introduced and evaluated with specific application to validation of the spatial normalization.*

Chapter 5 presents a set of methods for measuring the similarity of fiber bundles computed with streamline tractography. The measures evaluate both geometric similarity and similarity of the diffusion properties sampled by the fiber bundle. These methods may be used for quality control, evaluation of new tractography algorithms, and evaluation of atlas-based tractography. Binary overlap measures were shown to be problematic in the setting of tractography because of the thin shapes of the tracts. A closest point measure was created that provided an upper confidence limit on the distance between two tracts at a specific quantile. An evaluation of the atlas building method of Chapter 4 showed close geometric agreement for most tracts and differences of around 10% for FA and 4% for MD between tracts computed in the atlas and individual space.

5. *A novel method for computing tract oriented statistics enables population comparison to account for multivariate tensor shape measures and along tract correlation.*

To evaluate differences in the diffusion properties sampled by fiber bundles, Chapter 6 presents a statistical framework for comparing tract oriented mea-

asures of diffusion. The atlas building framework of Chapter 4 is used to create a template tensor image for all images in a study. The fiber tracts defined by this atlas are mapped to each subject to sample the diffusion properties at the corresponding anatomical location. The geometry of the atlas tract is then used to reduce each tract to a function of arc length for several diffusion parameters of interest such as FA and FRO. A multivariate hypothesis test is then used to test for differences between the populations of smooth functions, and the discrimination function embedded in the hypothesis test provides a representation of the most descriptive differences between two populations. B-spline fitting and PCA are used to regularize the solution.

6. *The atlas building method is applied to cross-sectional data of normal development to understand the maturation of diffusion properties over time.*

Section 7.2.1 presents the application of the atlas building method to data from a study of normal development. In this analysis, only cross-sectional analysis of the data is considered. Atlases built at several age points show that many major fiber bundles exist already at birth but continue to develop into adulthood as evidenced by changes in FA and tensor norm. Section 8.4.4 of this chapter discusses future work in longitudinal analysis and regression. Tract based analysis in section 7.2.2 further quantifies these changes in specific tracts from age 1 to 2 years.

7. *The tract oriented statistical method is applied to group analysis of pediatric and adult schizophrenia data.*

Several applications of the atlas building and tract statistics methods are presented in Chapter 7. An increase in FA and correlated decrease in FRO are shown from 1 to 2 years. Significant differences were found in the splenium tract between neonates diagnosed with MVM and healthy controls. Analysis of several tracts in schizophrenia showed no significant differences but illustrated the use of the methodology. Future developments in controlling for other clinical factors such as age and drug treatment are discussed in section 8.4.5 of this thesis.

8. *The framework developed in this thesis is made available as an open source toolkit for the benefit of the scientific community.*

The methods presented in this thesis are made available as open source software for use by the scientific community. The tensor estimation routines of Chapter 3 as well as the tensor resampling techniques discussed in Chapter 4 are made available in the DWIPProcess library. Appendix A describes how to use the software for tensor estimation, atlas building, and fiber tractography.

In summary, this thesis presents a framework that can be used for the analysis of diffusion image populations. The application of the framework to different clinical problems shows how neuroscience investigations can be improved by these image analysis techniques.

Thesis: Populations of diffusion tensor images provide valuable insight into white matter tissue structure. Measurement error and image pre-processing steps must be controlled to minimize error in statistics. Computation of an anatomically relevant coordinate system through atlas building and fiber tract modeling provides an intuitive shape-based framework for understanding differences in white matter microstructure. The combination of preprocessing, atlas building, and tract analysis provides a robust framework for making inferences about white matter differences in populations.

8.2 Limitations

There are several key assumptions in the proposed methodology that present limitations for the scope of this work. Some of these deficiencies can be addressed with future research.

8.2.1 Atlas Building

The atlas building methodology of Chapter 4 assumes that the overall appearance of DTI images is sufficiently similar between two groups that registration to a single coordinate system is feasible. This is a common assumption made in brain mapping approaches including popular software framework such as SPM and

FSL. In studies where subjects present with severe geometric distortions such as tumors, the approach presented in this thesis is likely not feasible. Tracts that are small or inconsistent even among the same group will be challenging to identify in the atlas. For this reason, I have focused on large major fiber bundles where consistency is expected. Smaller structures such as the short u-shaped fibers connecting neighboring gyri are not likely to be reliably identified using the atlas building method.

Misregistration in the atlas building procedure can confound the results of tract oriented statistics. Furthermore, the statistical analysis relies on tensor shape measures to make inference about potential changes in tissue structure at specific locations. However, there are several other effects that could have an impact on the tensor shape besides changes in tissue properties. For example, varying degrees of partial voluming effects can cause differences in total diffusivity that do not necessarily reflect changes in axon density or myelination. This can happen especially in fiber tracts adjacent to the ventricles. Part of the underlying change found in the splenium of the MVM population may be due to partial voluming with the lateral ventricles. Further studies are necessary to investigate the underlying biological cause of detected differences in DTI measures.

8.2.2 HARDI

The assumption of a single Gaussian diffusion profile per-voxel is a limitation for the analysis of brain regions that contain fiber crossings. This section addresses potential future work in extending the atlas building approach to HARDI data. Specifically, this section addresses potential approaches for resampling HARDI after deformation.

In the case of rigid transformations consisting only of translation plus an orthonormal rotation matrix, the problem of transforming HARDI is well-posed as a transformation of the coordinate system in which the measurements were obtained. In this case, a tensor D transformed by the rotation R can be represented as

$$D' = RDR^T. \tag{8.1}$$

Alternatively, we could update the gradient directions to reflect the new measurement frame replacing direction g with

$$g' = Rg. \quad (8.2)$$

In the context of image resampling, there may be some advantages to transforming the diffusion weighted images and updating the gradients based on resampling issues. When least-squares tensor estimation is used, the methods are equivalent, but for more advanced tensor estimation approaches, the transformation of diffusion weighted images may have resampling advantages. Furthermore, if DW images are transformed, then any model of interest (Q-Ball, DSI, CHARMED, two-tensor, etc.) can be estimated from the resampled data.

The finite strain model for tensor reorientation applies immediately to higher order diffusion models such as Gaussian mixtures, DSI, q-Ball, etc. In this case, for a diffusion model $Q(g)$ written as a radial function of the unit direction g , we can compute the rotated diffusion by $Q(R^T g)$. The PPD approach would need to be adapted based on specific modeling assumptions to account for the features of a higher-order diffusion model that needed to be preserved. For example, in a mixture of Gaussian model, the preservation of the two different principal diffusion directions could be balanced by weighting them according the volume fraction.

I propose two alternative methods for nonrigid transforms based on transformation and resampling of the DWI. The first method I will call gradient finite strain (GFS) and the second method I will call normalized gradient (NG).

The gradient finite strain approach is a straightforward extension of the finite strain model to reflect changes to the gradient directions instead of changes to the tensor. In this model, the transformation can be thought of as finding the closest rigid matrix to the transformation at a given point and applying that to the gradient directions. As mentioned before, for the case of tensors estimated using linear-least squares these methods are equivalent, but for other tensor estimation or higher order models, more information is retained in the GFS model. Similar to the FS approach, this method also has no impact on the shape of the diffusion model, because the transformation is projected to a pure rotation.

The normalized gradient approach is similar to that proposed by Tao and Miller [100]. In this method, the local transformation is applied to the gradient directions, which are then renormalized to be of unit length.

$$g' = \frac{Ag}{\|Ag\|} \quad (8.3)$$

The motivation for this method is an analysis of the units of Stejskal-Tanner equation. Units of space appear only in the orientation of the gradient directions g_i .

8.3 Additional Projects

The atlas building procedure has successfully been applied to projects by other researchers, indicating that the framework of this thesis can be applied to generic neuroimaging problems investigating white matter changes.

Collaborators at the University of Utah and University of North Carolina at Chapel Hill have performed study of aging in adults using the atlas building method presented in this thesis. A database of healthy adults from age 20 to 76 has been collected by Elizabeth Bullitt at University of North Carolina at Chapel Hill. After quality control, 86 images were selected from this database and the atlas building method of Chapter 4 was applied. A depiction of the constructed atlas and fiber tracts is shown in Fig. 8.1. Fiber tracts in the atlas are processed in a manner similar to that described in Chapter 6. Additional research is being performed to constrain the tract PCA to account for the age of the subject to apply regression analysis to the data.

Zhexing Liu, Hongtu Zhu, Bonita L. Marks, Laurence M. Katz, Guido Gerig, and Martin Styner have used the atlas building method to register a set of data from a study of the effect of fitness level on brain structure. Instead of the tract-based analysis described in this thesis, a bootstrap and permutation test analysis procedure was performed voxelwise on the registered images [116]. Preliminary evidence indicates there may be differences in diffusion measures due to physical activity.

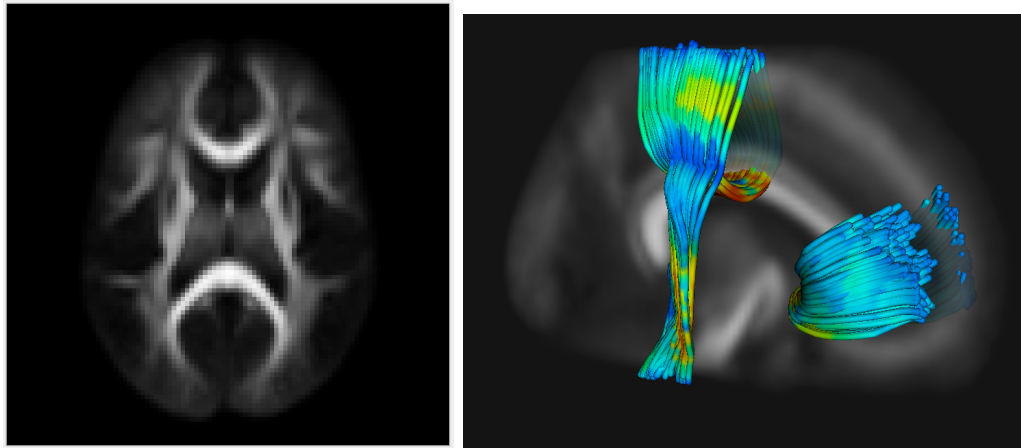


Figure 8.1. FA image and fiber tracts from atlas of adults.

Other studies include a singleton-twin neonate DTI analysis with 270 subjects, a function connectivity (fcMRI) and DTI study of early development with atlases for neonates, 1- and 2-year-old subjects (25 each), and analysis of 25 subjects with repeated scans at birth, 1year and 2years with focus on longitudinal data analysis of diffusion. The atlas building method has also been applied to nonhuman primate data by March Niethammer and UNC Chapel Hill.

8.4 Future Work

The methodology presented in this thesis can be extended in several ways to improve both reliability and accuracy as well as to extend the statistical analysis to several new areas of analysis.

8.4.1 Improvement of Atlas Building

Several key issues in the atlas building framework remain to be addressed in future work. Specifically, further developments in image match metrics and methods for tensor reorientation under deformations can improve future studies.

Two major considerations should be made in the development of new image match metrics. First, the image match metric may need to be reformulated to better optimize the orientation of fiber bundles. The current image metric serves primarily to align regions of high anisotropy. However, the alignment of principal eigenvectors

eventually used for tractography are not explicitly optimized. As a result, averages of the deformed images used for fiber tracking may have lower anisotropy than the original images. A second possible area of investigation is the more general problem of estimating transformations between images where quantitative intensity changes are to be evaluated. The process of registration is likely to confound the eventual analysis by aligning voxels with the same intensity resulting in minimal changes for statistical testing. There may be information theoretic arguments that need to be addressed regarding complementary data and the smoothness of the allowed registration.

In addition to improvements in metrics for diffusion image registration, additional improvements could be made in the methods for resampling diffusion images. In this thesis, the methods of Alexander et al. have been implemented for tensor reorientation [2]. Future improvements could focus on resampling DWI instead of DTI. This provides advantages both in terms of the ability to estimate higher order diffusion models as well as potential to better handle partial voluming effects. An initial prototype has been implemented incorporating the image resampling into the tensor estimation routine.

8.4.2 Physical Meaning of Diffusion Measures

One of the most important challenges in generating new scientific knowledge from DTI studies is identifying the underlying biological causes for changes in diffusion parameters. Daniel Alexander has recently published a new experimental design for directly measuring tissue properties such as axon radius [3]. Sharon Peled recently proposed that incorporation of a term for free isotropic diffusion can improve the biological meaning of anisotropy measures [79]. Significant work also remains in the validation of fiber tractography. Some initial work using histology of a macaque brain has attempted to validate DTI tractography [25]. Further development of similar work is necessary to be able to generate practical knowledge about biology from DTI.

8.4.3 Tract Oriented Analysis

Several limitations in the tract oriented analysis presented in Chapter 6 could be addressed by future research. The current strategy for identifying corresponding points along a tract relies on the arc length along each streamline from a user defined origin. This has several drawback when tracts have high curvature as streamlines closer to the interior of the bend will be shorter than streamlines along the edge, much like runners along track. Other researchers have developed methods for identifying along bundles correspondence by using distance maps [64] and optimal point match based on the Hungarian algorithm [76]. Additional improvements to the correspondence algorithm could explicitly account for the local curvature of the streamlines.

As pointed out by Yushkevich et al., not all tracts are well-approximated by a 1-dimensional representation [112]. Although there is some advantage to the greater flexibility of geometric description of the medial model, the high dimension low sample size problem addressed in applying global statistics, as in Chapter 6, becomes significantly more complicated.

Assuming that perfect correspondence can be found to assign points to a one parameter, there are still additional statistical challenges in modeling this as a single function. The distribution of many statistics such as FA are highly non-Gaussian. In this thesis, the FA of homologous points is averaged to produce a function of an arc length parameter t . However, for heavy tailed distributions, common for distributions of low FA, the mean is a not an informative summary statistic. Furthermore, the mean is sensitive to outliers due to partial voluming from residual misalignment of images. Statistics appropriate to the underlying distribution will have to developed: for example, a fit of the FA distribution by a beta distribution.

8.4.4 Longitudinal Tract Oriented Statistics

Chapter 6 presents a statistical method for hypothesis testing of tract statistics. The method uses multivariate tests in the space of PCA coefficients. The general linear model in statistics provides a mechanism for linking regression with hypothesis testing. Future work can investigate multilinear regression of tract parameters

with respect to a continuously varying parameter such as age. However, the problem of performing regression in multiple dimensions and especially on manifolds remains an active area of research [26, 111].

8.4.5 Incorporating Covariates

In addition to expanding tract oriented analysis to other statistical tools such as regression, future clinical studies will need to incorporate clinical covariates into statistical analysis. The methods of this thesis assume the only important clinical variable is the group to which the subjects are assigned. However, controlling for other clinical variables such as age, drug treatment, developmental scores, gender, etc. are likely to be important in finding clinically significant results.

CHAPTER 9

PUBLICATIONS

9.1 Journal Publications

- **Casey B. Goodlett**, P. Thomas Fletcher, John H. Gilmore, Guido Gerig. *Group analysis of DTI fiber tract statistics with application to neurodevelopment*. NeuroImage 45 (1) Supp. 1, 2009. p. S133-S142.
- Fan Zhang, Edwin Hancock, **Casey Goodlett**, Guido Gerig. *Probabilistic white matter fiber tracking using particle filtering and von Mises-Fisher sampling*. Medical Image Analysis 13 (1), 2009. p. 5-18.

9.2 Peer-Reviewed Conference Publications

- **Casey Goodlett**, P. Thomas Fletcher, John Gilmore, Guido Gerig. *Group statistics of DTI fiber bundles using spatial functions of tensor measures*. Lecture Notes in Computer Science, Medical Image Computing and Computer-Assisted Intervention, Springer-Verlag LNCS vol. 5241, 2008. pp. 1068-1075. *Runner up for MICCAI young scientist award*
- **Casey Goodlett**, P. Thomas Fletcher, Weili Lin, Guido Gerig. *Quantification of measurement error in DTI: Theoretical predictions and validation*. Lecture Notes in Computer Science, Medical Image Computing and Computer-Assisted Intervention, Springer-Verlag LNCS vol. 4791, 2007. pp. 10-17. *Oral Presentation*
- Fan Zhang, **Casey Goodlett**, Edwin Hancock, Guido Gerig. *Probabilistic fiber tracking using particle filtering*. Lecture Notes in Computer Science, Medical Image Computing and Computer-Assisted Intervention, Springer-Verlag LNCS vol. 4791, 2007. pp. 144-153.
- **Casey Goodlett**, Brad Davis, Remi Jean, John Gilmore, Guido Gerig.

Improved correspondence for DTI population studies via unbiased atlas building. Lecture Notes in Computer Science, Medical Image Computing and Computer-Assisted Intervention, Springer-Verlag LNCS vol. 4191, 2007. pp. 260 - 267.

9.3 Invited Presentations

- April 18, 2009. Diffusion Tensor MRI for the Clinician and the Neuroscientist: From Experimental Design to Data Analysis at ISMRM 2009. *Atlas Building and Tractography for Statistical Analysis of DTI*
- October 27, 2007. Advances in Diffusion MRI Analysis tutorial at MICCAI 2007. *Unbiased Atlas Building as a Coordinate System for Population Analysis of DTI*

9.4 Peer-Reviewed Short Papers and Workshops

- **Casey Goodlett**, P. Thomas Fletcher, Weili Lin, and Guido Gerig. *Noise-induced bias in low-direction diffusion tensor MRI: Replication of Monte-Carlo simulation with in-vivo scans.* ISMRM 2007.
- **Casey Goodlett**, Isabelle Corouge, Matthieu Jomier, and Guido Gerig, *A quantitative DTI fiber tract analysis suite*, The Insight Journal, vol. ISC/NA-MIC/ MICCAI Workshop on Open-Source Software, 2005, Online publication: <http://hdl.handle.net/1926/39>. *Oral Presentation.*

APPENDIX A

SOFTWARE USER GUIDE

This section provides an overview of the software environment required to run the atlas building procedure described in this thesis. The reader is assumed to have a basic understanding of using CMake to build programs from source code. The following instruction guide also assumes the use of a linux or UNIX environment.

The purpose of this procedure is to bring a population of tensor images into spatial correspondence. Spatial normalization of the population of images provides a reference coordinate system for the statistical analysis of diffusion parameters. The goal of this method is to enable comparison of diffusion properties and is not intended to evaluate shape differences of white matter structures.

A.1 Basic Software Environment

The tools described in this section require the following foundational software. A basic script to setup the software environment is available from <http://www.sci.utah.edu/~gcasey/research/code/setupenviron.sh>.

ITK The options `ITK_USE_REVIEW` and `ITK_USE_TRANSFORM_IO_FACTORIES` must be enabled. Version 3.8 or newer is recommended. <http://www.itk.org>

VTK Version 5.2 or greater is recommended. <http://www.vtk.org>.

Qt Version 3 is required. <http://www.trolltech.com/products>

SOViewer Available only through CVS at `:pserver:anoncvs:@public.kitware.com:/cvsroot/SOViewer`

TEEM Compiling with zlib support is recommended to enable compression of images. <http://teem.sourceforge.net>

NeuroLib CVS checkout available from `demeter.ia.unc.edu:/cvsroot`. Instruction for compiling the software are available from <http://www.ia.unc.edu/>

`dev/tutorials/Developer/neurolib-linux.htm`. Enable the programs `FiberTracking`, `FiberViewer`, `convertITKformats`, `DTIprocess` and `MriWatcher`.

A.2 Preprocessing

Images obtained from a typical clinical DTI scan are obtained from the scanner in DICOM format. The first step in processing of these images is convert them into a 3-dimensional format. NRRD is the NA-MIC standard image format for processing diffusion weighted and diffusion tensor images. Conversion of DICOM to NRRD is possible using the `DicomToNrrdConverter` tool in Slicer 3. Users of the NeuroLib library can use the `DicomConvert` tool to create a volume image from DICOM and then create the appropriate header with gradient information manually. Further documentation on the NRRD format for encoding DTI information is available at http://wiki.na-mic.org/Wiki/index.php/NAMIC_Wiki:DTI:Nrrd_format.

Before computation of diffusion tensors, several types of correction may need to be performed depending on image quality and the imaging pulse sequence. Rigid registration between images with different diffusion weighting may need to be performed to correct for subject motion during the acquisition. Eddy current distortions may need to be corrected to account for the varying gradient directions in DTI sequences. A common technique to correct for both of these issues is to use a single affine transformation per diffusion weighted image to account for both patient motion and eddy current distortion.

A.2.1 Tensor Estimation

After correction for image transformations, `dtiestim` estimates a tensor image from the set of diffusion weighted images. The main options for the `dtiestim` program are described below. This program is included in the `DTIProcess` project in NeuroLib.

```

dtiestim - dtiestim dwi-image tensor-image [options]
-H,--help Obtains help on the use of dtiestim
-M,--brain-mask A binary image that enables tensor estimation in voxels
    only where the mask is greater than zero.
-t,--threshold <threshold> Threshold on the nondiffusion weighted im-
    ages to estimate tensors. If this is not specified we attempt to detect the
    threshold by the OTSU algorithm on the nondiffusion weighted image.
-m,--method <method> Options are
    lls Linear least squares. Standard estimation technique that recovers
        the tensor parameters by multiplying the log of the normalized signal
        intensities by the pseudo-inverse of the gradient matrix. Default
        option.
    wls Weighted least squares. This method is similar to the linear least
        squares method except that the gradient matrix is weighted by the
        original lls estimate. See [87] for more information on this method.
        This method is recommended for most applications. It is
        not currently the default due to occasional matrix singularities.
    nls Nonlinear least squares. This method does not take the log of the
        signal and requires an optimization based on Levenberg-Marquadt
        to optimize the parameters of the signal. The lls estimate is used
        as an initialization.
    ml Maximum likelihood estimation. This method is experimental and
        is not currently recommended.

```

For example, to estimate tensors from the diffusion weighted image `dwi.nhdr` the following command line could be used.

```
$ dtiestim dwi.nhdr tensors.nrrd -t 200 -m wls
```

The output tensor image is represented as a double precision, six channel image representing the tensor elements $\{D_{xx}, D_{xy}, D_{xz}, D_{yy}, D_{yz}, D_{zz}\}$. Note that this is different than the teem representation that uses an additional channel as a mask. The Slicer 3 default representation uses 9 channels to represent each element of the diffusion tensor $\{D_{xx}, D_{xy}, D_{xz}, D_{yx}, D_{yy}, D_{yz}, D_{zx}, D_{zy}, D_{zz}\}$.

After tensor estimation, `dtiprocess`, found in the DTIPProcess project of NeuroLib, can be used to compute scalar maps for various tensor measures. The `dtiprocess` has two major use cases. The first is the production of scalar invariant images from a tensor field. The usage for this is described below. The second major use case is resampling tensor fields, which is described later in section A.3.4.

```

dtiprocess - dtiprocess tensor-image [options]
-f,--fa-output <faimage> Produces the FA image from a tensor field. The
  FA for locations with no tensors is set to zero. The FA is written to
  an unsigned short image by default with the FA multiplied by 10,000
  to fit within the integer range. If floating point is preferred see the
  --scalar-float option.
-m,--md-output <mdimage> Produces the MD image from a tensor field.
  The MD for locations with no tensors is set to zero. The MD is written to
  an unsigned short image by default with the MD multiplied by 100,000
  to fit within the integer range. If floating point is preferred see the
  --scalar-float option.
--lambda1-output <lambdaimage> Produces the image of largest eigenval-
  ues ( $\lambda_1$ ) of each tensor. The eigenvalue is multiplied by 100,000 and
  written as an unsigned short by default. See --scalar-float for
  floating point precision.
--lambda2-output <lambdaimage> Produces the image of middle eigenval-
  ues ( $\lambda_2$ ) of each tensor. The eigenvalue is multiplied by 100,000 and
  written as an unsigned short by default. See --scalar-float for
  floating point precision.
--lambda3-output <lambdaimage> Produces the image of smallest eigen-
  values ( $\lambda_3$ ) of each tensor. The eigenvalue is multiplied by 100,000
  and written as an unsigned short by default. See --scalar-float for
  floating point precision.
--scalar-float If this option is specified then tensor invariants are written
  in unscaled floating point format instead of scaled to fit in the integer
  range.
-c,--color-fa-output <cfaimage> Produces the colored FA image from a
  tensor field. This is equivalent to assigning an RGB intensity to each
  voxel where the principal eigenvector expressed in left posterior superior
  (LPS) coordinates maps to directly to an RGB vector scaled by the FA
  value.

```

The following command computes the FA and MD images.

```
$ dtiprocess tensors.nrrd -f fa.nrrd -m md.nrrd
```

A.2.2 Data Requirements and Quality Control

Quality control of the set of diffusion should be performed to ensure that images are free from artifacts. The first major concern is that all images must be of the exact same dimension and should contain the same anatomy. The easiest solution to populations that contain images of different sizes is to pad those smaller images

with zeros in the diffusion weighted images. However, if the images are smaller due to slices of anatomy that have been omitted, for example the top of the head, there is a higher risk of registration failure. The `unu` tool is the recommended tool for padding images in NRRD format. For example, if the difference between images is the number of axial slices, images can be padded using the following command for diffusion weighted images with the third axis representing the axial direction.

```
$ unu pad -i dwi.nrrd -o paddeddwi.nrrd -min 0 0 0 0
    -max M M M <max # slices> M -b pad -v 0
```

Alternatively individual images can be padded using the following command.

```
$ unu pad -i dwi0000.nrrd -o paddeddwi0000.nrrd -min 0 0 0
    -max M M M <max # slices> -b pad -v 0
```

Further documentation on the options for `unu` are available in the command line documentation or at <http://teem.sourceforge.net>.

MriWatcher is a useful tool for checking for image artifacts in a population of images. Images should be checked prior to registration for consistency of quality. Images with slice dropouts or substantial artifacts should be excluded from the atlas building procedure. Visual inspection of both the FA and MD images is recommended.

A.3 Atlas Building

The atlas building consists of two stages. First, affine alignment is used to initialize the transformation for a second stage of nonrigid registration. However, prior to registration, quality control of the images is essential to obtain reliable results

A.3.1 Affine Alignment

The recommended method to initialize the transformations for each image is to use a template T2 weighted MR image that is aligned in a desired coordinate system such as AC-PC space. The baseline image of the diffusion weighted sequence

should be used as the moving image and the template as the fixed image. For a DWI sequence encoded in a 4D NRRD file. The baseline image can be extracted as follow

```
$ unu slice -i dwi.nrrd -o b0.nrrd -a 3 -p <index of b0 image>
```

If there are multiple baseline images, they can be averaged to produce a single image using

```
$ unu crop -i dwi.nrrd -min 0 0 0 0 -max M M M <# baseliens> |  
  unu proj -a 3 -m mean -o b0.nrrd
```

An alternative method is to use one image in the sequence as a template. In this case, affine transformations based on mutual information of the baseline images is also recommended.

Currently, the RView software is used to compute the affine alignment of the images. Binaries for the RView software are available from <http://www.doc.ic.ac.uk/~dr/software/index.html>.

```
$ areg <targetimage> <sourceimage> -dofout <doffile> -p15  
  -parameter params.txt
```

The `params.txt` specifies the parameters of the affine registration. A sample file is given below:

```

#
# Target image parameters
#
Target blurring (in mm)           = 1.0
Target resolution (in mm)         = 2.0
#
# Source image parameters
#
Source blurring (in mm)           = 1.0
Source resolution (in mm)         = 2.0
#
# Registration parameters
#
No. of resolution levels          = 3
No. of bins                       = 48
No. of iterations                 = 20
No. of steps                      = 5
Length of steps                   = 2.0
Similarity measure                = NMI
Lambda                           = 0

```

A.3.2 Feature Image

As described by Goodlett et al., a feature image based on the Hessian of the FA image is used as the basis for registration [43]. The program used to compute the feature image is `maxcurvature`. The program is used as follows:

```
$ maxcurvature <inputimage> -o <outputimage> -s <sigma>
```

For most adult images, a sigma of 2.0 is recommended. For neonate or primate images, a smaller sigma of 1.0 – 1.5 is more appropriate. If the data is particularly noisy, a larger sigma of 2.5 – 4 may be necessary.

A.3.3 Nonrigid Alignment

There are two methods available for nonrigid registration. The fluid atlas building approach as implemented in `AtlasWerks` has been used extensively. This software is not available as open source.

A.3.3.1 AtlasWerks

The fluid registration procedure is implemented in the `AtlasWerks` program. A sample set of parameters for `AtlasWerks` suitable for DTI images is shown below.

```
$ AtlasWerks \
  --scaleLevel=4 --numberOfIterations=50 \
  --alpha=0.1 \
  --beta=0.1 \
  --gamma=0.01 \
  --maxPerturbation=0.4 \
--scaleLevel=2 --numberOfIterations=50 \
  --alpha=0.1 \
  --beta=0.1 \
  --gamma=0.01 \
  --maxPerturbation=0.4 \
--scaleLevel=1 --numberOfIterations=100 \
  --alpha=0.01 \
  --beta=0.01 \
  --gamma=0.001 \
  --maxPerturbation=0.4
-o=atlaswerks/avgimage_ \
-f=atlaswerks/f \
-p=atlaswerks/i \
<Image0> <Image1> <...> \
<InitTrans0> <InitTrans1> <...>
```

A.3.3.2 MultiImageRegistration

Recently, Polina Golland and Serdar Balci at MIT released a B-spline unbiased atlas building technique <http://hdl.handle.net/1926/568>. This can be downloaded from the NA-MIC sandbox at <http://svn.na-mic.org/NAMICSandbox/trunk/MultiImageRegistration>.

The parameters for B-spline atlas building are specified in two files. The first file is a text file listing the input files. There are 3 required inputs in this file: the input folder, the output folder, and the list of files. These files should be the result of the feature images computer as described in Sec A.3.2. A sample `filenames.txt` is given below:

```
#
# The path of the input folder for images.
# All images are assumed to be in the same folder.
# (don't forget to have backslash as the last character)
#
# If images are in different folders ignore
# this parameter and supply the full pathname
# as filename.
#
-i /usr/sci/projects/neuro/PNL-new/mirlinks/

#
# The path of the output folder.
# All outputs are saved to this folder
#
#
-o /usr/sci/projects/neuro/PNL-new/mirreg/
```

```

# names of the input files
# if inputFolder is specified, the pathname is relative to that
# folder. Otherwise supply the full pathname
#
-f image-001-curv.nrrd
-f image-002-curv.nrrd
-f image-003-curv.nrrd
-f image-004-curv.nrrd

```

The second file required contains the list of parameters for the algorithm. For the method described in this paper, the variance metric is the most appropriate. The `useBspline` option should be enabled. The `useBsplineHigh` option should be disabled initially. This option controls whether the B-spline control points are refined after the initial B-spline registration. Users can experiment with this option, but it does not always run reliably. The three `numberOfSpatialSamples` options control the percentage of the image used in computing the image match term. Increasing this value improves the stability of the optimization but requires more computation time. If the objective function does not decrease consistently, try increasing this term. The `useNormalizeFilter` should be disabled because the intensities of the images are standardized prior to running this algorithm.

If users wish to use an affine alignment for each image from previous registration to a template, they should create in the output directory the directory tree `Affine/TransformFiles`. In this directory, there should be a file for each input image specified in the `filenames.txt` file. The file should end in a `.txt` extension and should contain an itk `AffineTransform` in double precision. These transformation files can be created from RView `.dof` files using the `tio` executable from DTIPProcess.

```

#
# PARAMETERS OF BINARY FILE

```

```
#

#
# metricType specifies which objective function to use
# possible options:
#
#   entropy: congealing with entropy
#   variance: registering to the mean template image using
#               sum of square differences

-metricType variance

#
# If useBpline is set off, only affine registration is done,
# if it is on and useBspline high is off, bspline registration
# is done with specified grid region. If useBsplineHigh is on
# bspline registration with mesh refinement is performed
#
# Options to use:
#   useBspline on/off
#   useBsplineHigh on/off
#

-useBspline on
-useBsplineHigh off

#
```

```
# defines the initial bspline grid size along each dimension
#
    -bsplineInitialGridSize 8

#
# When using Bspline grid refinement, this options defines
# how many number of refinements to use. After each level
# number B-spline control points are doubled (8->16->32)
#
    -numberOfBsplineLevel 2

#
# All objective functions make use of stochastic subsampling
# following options define the number of spatial samples as
# percentage of the total number of voxels in the image (Try
# to increase the number of samples if the registration
# accuracy is poor)
#
    -numberOfSpatialSamplesAffinePercentage 0.050
    -numberOfSpatialSamplesBsplinePercentage 0.1
    -numberOfSpatialSamplesBsplineHighPercentage 0.2

#
# following options define number of multiresolution levels
# used in optimization if set to one no multiresolution
# optimization is performed. Affine/Bspline/BsplineHigh
# define number of multiresolution levels used for each
```

```
# registration stage
#
# (For high resolution anatomical images at 256x256x128 voxels
# we used 3 levels, decrease the number of levels if the
# resolution of the input image is low )

    -multiLevelAffine 2
    -multiLevelBspline 2
    -multiLevelBsplineHigh 2

#
# Following options define the number iterations to be
# performed Optimization is terminated after a fixed number
# of iterations no other termination options are used
#

    -optAffineNumberOfIterations 50
    -optBsplineNumberOfIterations 40
    -optBsplineHighNumberOfIterations 40

#
# Following options define the learning rate of the
# optimizers for each stage of the registration
#
# (decrease the learning rate if you get
# "all samples mapped outside" error
#
```

```
-optAffineLearningRate 1e-10
-optBsplineLearningRate 1e-6
-optBsplineHighLearningrate 1e-7

#
# Currently there are three optimizer types. "gradient" is
# a fixed step gradient descent search. "lineSearch" is
# gradient descent search where step size is determined
# using line search.
#
# optimizerType gradient/lineSearch/SPSA
#

    -optimizerType lineSearch

#
# Specifies the percentage increase in the sampling rate
# after each multiresolution level
#

    -affineMultiScaleSamplePercentageIncrease 4.0
    -bsplineMultiScaleSamplePercentageIncrease 4.0
```

```
#  
# Specifies increase in the number of iterations  
# after each resolution level  
#  
    -affineMultiScaleMaximumIterationIncrease 2.0  
    -bsplineMultiScaleMaximumIterationIncrease 2.0  
  
#  
# Specifies optimizer step length increase after each  
# multiresolution level  
#  
    -affineMultiScaleStepLengthIncrease 4.0  
    -bsplineMultiScaleStepLengthIncrease 4.0  
  
#  
# the width of the parzen window to compute the entropy  
# used by all metric types computing entropy  
#  
    -parzenWindowStandardDeviation 10.0  
  
#  
# Use normalize filter to normalize input images  
# to have mean zero and standard deviation 1.  
#  
    -useNormalizeFilter off  
  
#  
# Write 3D images to file.
```

```
# turn off to save disk space
#

    -write3DImages on

#####

#
# ADVANCED OPTIONS
#
#####

#
# the level of registration to be started
# Use this option if you want to start the registration
# using the results of a previous registration
#
# 0 (default): no initialization, all registrations are
#               performed
# 1 : Affine parameters are read from the file
# 2 : B-spline parameters are read from file (initial size should
# match the transform from file )
#

    -StartLevel 1
```

```
#
# Uses a mask on the images. Only pixels inside the mask are
# considered during the registration possible options mask
# none/single/all none: do not use mask single: only use
# mask for the first image all: use mask for all images
#
    -mask all

#
# specifies the mask type
# possible options:
#     maskype connectedThreshold/neighborhoodConnected
#
# connectedThreshold: adds all pixels
#                       to the mask if its value is smaller
#                       than threshold1 than add connected
#                       pixels whose value is smaller than
#                       threshold2
# neighborhoodConnected: same as connectedThreshold but a
#                           pixel is added only if it is all
#                           connected within a radius of one
#
    -maskType connectedThreshold
    -threshold1 0
    -threshold2 1

#
# specifies the translation scale coefficients with respect
```

```
# to the affine coefficients smaller values mean larger step
# size along translation directions 1/scale is used!
```

```
-translationScaleCoeffs 1e-4
```

```
#
# Maximum number of iterations performed for a line search
# if the optimizer is lineSearch
#
```

```
-maximumLineIteration 6
```

```
-BSplineRegularizationFlag on
```

```
-gaussianFilterKernelWidth 5
```

Once the parameters are determined, the registration is run using the command:

```
$ MultiImageRegistration filenames.txt parameters.txt
```

After completion of this routine, the B-spline deformation parameters have been computed. To resample the feature images using the transformations, use the command:

```
$ ComputeOutputs filenames.txt parameters.txt
```

To apply the deformations to the tensor field, the B-spline parameters must be converted into deformation fields using the command:

```
$ ComputeDeformations filenames.txt parameters.txt
```

This will create deformation fields for each level of transformation. For example, the B-spline registration run at a grid spacing of 8 will be in the directory

OUTPUT_DIRECTORY/Bspline_Grid_8/DeformationImage. The deformation field is expressed in world coordinates.

A.3.4 Tensor Resampling and Averaging

Resampling of tensor fields using a transformation is implemented in the executable `dtiprocess`. To deform images using the deformation fields produced in the previous steps the `--deformation-output` and `--forward` options should be used.

```
dtiprocess - dtiprocess tensor-image [options]
-r,--rot-output Output name for the resampled tensor field given computed from an affine transformation. This option requires the transformation to be specified using the --dof-file option.
-d,--dof-file Filename of an ITK affine transformation. This option requires the output image to be specified using the --rot-output option.
-w,--deformation-output Output name for the resampled tensor field given computed from a deformation field. This option requires the deformation field to be specified using the --foward option.
-F,--forward Filename of a deformation field to resample a tensor field. This option requires the output filename to be specified using --deformation-output.
--h-field If this option is used the --forward transformation represents an h-field rather than a deformation field. This option should be used in conjunction with the output from AtlasWerks but not MultiImageRegistration.
```

For example, a tensor field may be resampled with a deformation field by the command:

```
$ dtiprocess tensors.nrrd -w resampled-tensors.nrrd\
-F transform.nrrd
```

If the transformation is an h-field, then the `--h-field` option must be specified. To transform using an affine transformation, the command is

```
$ dtiprocess tensors.nrrd -r resampled-tensors.nrrd\
-d transform.txt
```

The `dtiaverage` executable is used to average tensor fields using the command:

```
$ dtiaverage atlas.nrrd image1.nrrd image2.nrrd ...
```

A.3.5 Tractography

The application for performing fiber tractography is `fibertrack`. This program implements a simple streamline tractography method based on the principal eigenvector of the tensor field. A fourth order Runge-Kutta integration rule is used to advance the streamlines.

```
fibertrack - fibertrack [options]
-i,--input-tensor-file <tensorfile> The filename of the tensor field to
  use for tractography.
-r,--input-roi-file <labelfile> The filename of the image which con-
  tains the labels used for seeding and constraining the algorithm.
-o,--output-fiber-file <fiberfile> The filename for the fiber file pro-
  duced by the algorithm. This file must end in a .fib, .vtk, or
  .vtp extension for ITK spatial object, legacy vtkPolyData, and XML
  vtkPolyData formats, respectively. Slicer3 currently uses the XML
  vtkPolyData format .vtp.
-s,--source-label <sourcelabel=2> The label of voxels in the
  <labelfile> to use for seeding tractography. One tract is seeded from
  the center of each voxel with this label.
-t,--target-label <sourcelabel=1> The label of voxels in the
  <labelfile> used to constrain tractography. Tracts that do not
  pass through a voxel with this label are rejected. Set this keep all
  tracts.
--min-fa The minimum FA threshold to continue tractography.
--whole-brain If this option is enabled, all voxels in the image are used to
  seed tractography. When this option is enabled, both source and target
  labels function as target labels.
```

An example using both a seed and target region is

```
$ fibertrack -i tensors.nrrd -r roi.nrrd -o output.fib -s 2\
  -t 1 --min-fa 0.2
```

APPENDIX B

GRADIENT DIRECTION SCHEMES

Table B.1: 6 direction gradient list.

0.70711	0	0.70711
-0.70711	0	0.70711
0	0.70711	0.70711
0	0.70711	-0.70711
0.70711	0.70711	0
-0.70711	0.70711	0

Table B.2: 21 direction gradient list.

-0.99823	-0.036499	0.047033
0.037648	0.85056	0.52452
-0.85783	0.49589	0.13495
0.25729	-0.025629	0.96599
-0.59516	-0.43791	0.67381
-0.54816	0.49097	0.67711
-0.82631	0.04477	0.56144
0.48971	0.84011	0.23324
-0.82302	-0.53713	0.18476
0.77956	-0.037959	0.62517
-0.45054	0.84917	0.27554
-0.3338	-0.024468	0.94233
-0.044461	0.45427	0.88975
0.25947	-0.87224	0.41457
-0.33418	-0.85152	0.40402
-0.063334	-0.54422	0.83655
0.47387	-0.48088	0.7377
0.84672	0.43078	0.31224
0.48855	0.47013	0.73505
0.78015	-0.55755	0.28372
0.99647	-0.046849	0.0696

Table B.3: 60 direction gradient list.

-0.225320	0.055654	0.981680
-0.509270	0.152240	0.854970
0.365440	0.508180	-0.791900
0.021612	0.966370	-0.302640
-0.403870	0.408240	0.826600
0.284580	0.786030	0.584630
-0.629650	0.819730	-0.024646
-0.883010	0.083680	0.476810
-0.181710	0.620060	0.773770
-0.322260	0.859670	-0.452790
0.226280	0.978710	-0.002019
-0.319160	0.924110	0.242330
0.102410	0.024489	-1.024000
0.368650	0.214140	-0.943050
-0.759420	0.326850	-0.580390
-0.507860	0.329140	-0.822490
-0.339180	0.951390	-0.112360
-0.834270	0.481130	-0.310410
0.236480	0.797350	-0.590180
0.540960	0.845280	0.025840
0.747820	0.234010	0.628630
0.948520	0.121280	0.325580
0.505680	0.383160	0.778810
0.004191	0.924110	0.397120
0.652440	0.309380	-0.723390
-0.765730	0.325120	0.578560
0.327430	0.906330	0.283500
-0.563340	0.586620	-0.594410
-0.864100	0.552980	-0.021943
0.986890	0.067139	-0.300100
-0.262280	0.543680	-0.806280
-0.729290	0.045479	-0.707170
-0.972560	0.251390	0.186710
0.979030	0.325320	0.016802
-0.264230	0.152910	-0.972750
0.244590	0.376850	0.899190
-0.091015	0.331460	0.949350
0.073455	0.572770	-0.829230
0.785590	0.631900	0.073338
0.204960	0.063818	0.988980
0.826550	0.546660	-0.226320

Table B.3: Continued

0.533020	0.063079	0.849640
0.616840	0.749590	-0.310270
0.874730	0.339830	-0.395190
-0.551450	0.771510	0.331530
-0.595060	0.775770	-0.325180
-0.264520	0.801000	0.544430
0.125040	0.642030	0.764910
0.581470	0.606830	0.603480
0.015824	0.295740	-0.977300
0.614060	0.597040	-0.587000
-0.972950	0.236110	-0.079699
-0.785120	0.559300	0.297070
-0.058150	0.793590	-0.643820
0.850160	0.424510	0.363930
-0.947880	0.094560	-0.330890
0.580350	0.756110	0.350100
-0.569340	0.565710	0.605840
0.333620	0.899950	-0.318550
-0.036549	1.005900	0.028565

REFERENCES

- [1] ALEXANDER, A. L., LEE, J. E., LAZAR, M., BOUDOS, R., DUBRAY, M. B., OAKES, T. R., MILLER, J. N., LU, J., JEONG, E.-K., MCMAHON, W. M., BIGLER, E. D., AND LAINHART, J. E. Diffusion tensor imaging of the corpus callosum in autism. *NeuroImage* 34, 1 (2007), 61 – 73.
- [2] ALEXANDER, D., PIERPAOLI, C., BASSER, P. J., AND GEE, J. Spatial transformations of diffusion tensor magnetic resonance images. *Medical Imaging, IEEE Transactions on* 20, 11 (Nov. 2001), 1131–1140.
- [3] ALEXANDER, D. C. A general framework for experiment design in diffusion MRI and its application in measuring direct tissue-microstructure features. *Magnetic Resonance in Medicine* 60, 2 (2008), 439–448.
- [4] ANDERSON, A. W. Theoretical analysis of the effects of noise on diffusion tensor imaging. *Magnetic Resonance in Medicine* 46, 6 (15 Nov. 2001), 1174–1188.
- [5] ARSIGNY, V., FILLARD, P., PENNEC, X., AND AYACHE, N. Fast and simple calculus on tensors in the log-Euclidean framework. In *MICCAI* (2005), vol. 3749 of *LNCS*, pp. 115–122.
- [6] ARSIGNY, V., FILLARD, P., PENNEC, X., AND AYACHE, N. Log-Euclidean metrics for fast and simple calculus on diffusion tensors. *Magnetic Resonance in Medicine* 56, 2 (2006), 411–421.
- [7] AWATE, S., HUI, Z., AND GEE, J. A fuzzy, nonparametric segmentation framework for dti and mri analysis: With applications to dti-tract extraction. *Medical Imaging, IEEE Transactions on* 26, 11 (Nov. 2007), 1525–1536.
- [8] BARNEA-GORALY, N., KWON, H., MENON, V., ELIEZ, S., LOTSPEICH, L., AND REISSA, A. L. White matter structure in autism: preliminary evidence from diffusion tensor imaging. *Biological Psychiatry* 55, 3 (Feb. 2004), 323–326.
- [9] BASSER, P., MATTIELLO, J., AND LEBIHAN, D. Mr diffusion tensor spectroscopy and imaging. *Biophysical Journal* 66, 1 (1994), 259 – 267.
- [10] BASSER, P., AND PIERPAOLI, C. Microstructural and physiological features of tissues elucidated by quantitative DT-MRI. *Journal Magnetic Resonance* 111, 3 (June 1996), 209–219.

- [11] BASSER, P. J. Relationships between diffusion tensor and q-space MRI. *Magnetic Resonance in Medicine* 47, 2 (Feb. 2002), 392–397.
- [12] BASSER, P. J., AND PAJEVIC, S. Statistical artifacts in diffusion tensor MRI (DT-MRI) caused by background noise. *Magnetic Resonance in Medicine* 44, 1 (2000), 41–50.
- [13] BASSER, P. J., AND PAJEVIC, S. Dealing with uncertainty in diffusion tensor MR data. *Israel Journal of Chemistry* 43, 1 (2003), 129–144.
- [14] BASSER, P. J., PAJEVIC, S., PIERPAOLI, C., DUDA, J., AND ALDROUBI, A. In vivo fiber tractography using DT-MRI data. *Magnetic Resonance in Medicine* 44, 4 (2000), 625–632.
- [15] BASTIN, M. E., ARMITAGE, P. A., AND MARSHALL, I. A theoretical study of the effect of experimental noise on the measurement of anisotropy in diffusion imaging. *Magn Reson Imaging* 16, 7 (1998), 773–85.
- [16] BASU, S., FLETCHER, P. T., AND WHITAKER, R. Rician noise removal in diffusion tensor MRI. In *Medical Image Computing and Computer Assisted Intervention (MICCAI)* (2006), vol. 4190 of *LNCS*, pp. 117–125.
- [17] BIHAN, D. L. Looking into the functional architecture of the brain with diffusion MRI. *Nature Reviews Neuroscience* 4, 6 (2003), 469–480.
- [18] BONEKAMP, D., NAGAE, L. M., DEGAONKAR, M., MATSON, M., ABDALLA, W. M., BARKER, P. B., MORI, S., AND HORSKÁ, A. Diffusion tensor imaging in children and adolescents: Reproducibility, hemispheric, and age-related differences. *NeuroImage* 34 (2007), 733–742.
- [19] BRAIN DEVELOPMENT COOPERATIVE GROUP, AND EVANS, A. C. The NIH MRI study of normal brain development. *NeuroImage* 30, 1 (2006), 184–202.
- [20] BURNS, J., JOB, D., BASTIN, M. E., WHALLEY, H., MACGILLIVRAY, T., JOHNSTONE, E. C., AND LAWRIE, S. M. Structural disconnectivity in schizophrenia: a diffusion tensor magnetic resonance imaging study. *The British Journal of Psychiatry* 182, 5 (2003), 439–443.
- [21] CANNY, J. A computational approach to edge detection. *Pattern Analysis and Machine Intelligence, IEEE Transactions on* 8, 6 (Nov. 1986), 679–698.
- [22] CASICIO, C. J., GERIG, G., AND PIVEN, J. Diffusion tensor imaging: Application to the study of the developing brain. *Journal of the American Academy of Child and Adolescent Psychology* 46, 2 (Feb. 2007), 213–223.
- [23] COROUGE, I., FLETCHER, P. T., JOSHI, S., GOUTTARD, S., AND GERIG, G. Fiber tract-oriented statistics for quantitative diffusion tensor MRI analysis. *Medical Image Analysis* 10, 5 (2006), 786–798.

- [24] COROUGE, I., GOUTTARD, S., AND GERIG, G. Towards a shape model of white matter fiber bundles using diffusion tensor mri. In *Biomedical Imaging: Nano to Macro, 2004. IEEE International Symposium on* (Washington DC, April 2004), pp. 344–347.
- [25] DAUGUET, J., PELED, S., BEREZOVSKII, V., DELZESCAUX, T., WARFIELD, S. K., BORN, R., AND WESTIN, C.-F. Comparison of fiber tracts derived from in-vivo DTI tractography with 3d histological neural tract tracer reconstruction on a macaque brain. *NeuroImage* 37, 2 (2008), 530–538.
- [26] DAVIS, B., FLETCHER, P., BULLITT, E., AND JOSHI, S. Population shape regression from random design data. In *Computer Vision, 2007. ICCV 2007. IEEE 11th International Conference on* (Oct. 2007), pp. 1–7.
- [27] DESCOTEAUX, M., ANGELINO, E., FITZGIBBONS, S., AND DERICHE, R. Apparent diffusion coefficients from high angular resolution diffusion imaging: Estimation and applications. *Magnetic Resonance in Medicine* 56, 2 (2006), 395–410.
- [28] DING, Z., GORE, J. C., AND ANDERSON, A. W. Classification and quantification of neuronal fiber pathways using diffusion tensor MRI. *Magnetic Resonance in Medicine* 49, 4 (2003), 716–721.
- [29] DURSTON, S., HULSHOFF, H. E., CASEY, B., GIEDD, J. N., BUITELAAR, J. K., AND VAN ENGELAND, H. Anatomical MRI of the developing human brain: What have we learned? *Journal of the American Academy of Child and Adolescent Psychiatry* 40, 9 (2001), 1012–1020.
- [30] ENNIS, D. B., AND KINDLMANN, G. Orthogonal tensor invariants and the analysis of diffusion tensor magnetic resonance images. *Magnetic Resonance in Medicine* 55, 1 (Jan. 2006), 136–146.
- [31] FILLARD, P., ARSIGNY, V., PENNEC, X., AND AYACHE, N. Clinical DT-MRI estimation, smoothing and fiber tracking with log-Euclidean metrics. In *Proceedings of the Third IEEE International Symposium on Biomedical Imaging (ISBI 2006)* (Crystal Gateway Marriott, Arlington, Virginia, USA, Apr. 2006), LNCS, pp. 786–789.
- [32] FILLARD, P., ARSIGNY, V., PENNEC, X., AND AYACHE, N. Clinical DT-MRI estimation, smoothing and fiber tracking with log-Euclidean metrics. *IEEE Transactions on Medical Imaging* 26, 11 (Nov. 2007), 1472–1482. PMID: 18041263.
- [33] FLETCHER, P., AND JOSHI, S. Principal geodesic analysis on symmetric spaces: Statistics of diffusion tensors. In *ECCV 2004, Workshop CVAMIA* (2004), pp. 87–98.
- [34] FLETCHER, P. T., AND JOSHI, S. Riemannian geometry for the statistical analysis of diffusion tensor data. *Signal Processing* 87, 2 (2007), 250–262.

- [35] FLETCHER, P. T., TAO, R., JOENG, W.-K., AND WHITAKER, R. A volumetric approach to quantifying region-to-region white matter connectivity in diffusion tensor MRI. In *Information Processing in Medical Imaging* (2007), vol. 4584 of *LNCS*, pp. 346–358.
- [36] FRIMAN, O., FARNEBACK, G., AND WESTIN, C.-F. A bayesian approach for stochastic white matter tractography. *Medical Imaging, IEEE Transactions on* 25, 8 (Aug. 2006), 965–978.
- [37] FRISTON, K., ASHBURNER, J., KIEBEL, S., NICHOLS, T., AND PENNY, W., Eds. *Statistical Parametric Mapping: The Analysis of Functional Brain Images*. Academic Press, 2007.
- [38] GERIG, G., JOMIER, M., AND CHAKOS, M. Valmet: A new validation tool for assessing and improving 3d object segmentation. In *Medical Image Computing and Computer Assisted Intervention (MICCAI)* (2001), vol. 2208 of *LNCS*, Springer-Verlag, pp. 516–523.
- [39] GIEDD, J. N., BLUMENTHAL, J., JEFFRIES, N. O., CASTELLANOS, F. X., LIU, H., ZIJDENBOS, A., PAUS, T. C., EVANS, A. C., AND RAPOPORT, J. L. Brain development during childhood and adolescence: a longitudinal MRI study. *Nature Neuroscience* 2, 10 (1999), 861–863.
- [40] GILMORE, J. H., LIN, W., COROUGE, I., VETSA, Y. S., SMITH, J. K., KANG, C., GU, H., HAMER, R. A., LIEBERMAN, J. A., AND GERIG, G. Early postnatal development of corpus callosum and corticospinal white matter assessed with quantitative tractography. *American Journal of Neuro-radiology* 28, 9 (Nov. 2007), 1789–1795.
- [41] GILMORE, J. H., SMITH, L. C., WOLFE, H. M., HERTZBERG, B. S., SMITH, J. K., CHESCHEIR, N. C., EVANS, D. D., KANG, C., HAMER, R. M., LIN, W., AND GERIG, G. Prenatal mild ventriculomegaly predicts abnormal development of the neonatal brain. *Biological Psychiatry* 64, 12 (2008), 1069 – 1076. Schizophrenia: Neural Circuitry and Molecular Mechanisms.
- [42] GILMORE, J. H., VAN TOL, J., KLIEWER, M. A., SILVA, S. G., COHEN, S. B., HERTZBERG, B. S., AND CHESCHEIR, N. C. Mild ventriculomegaly detected in utero with ultrasound: clinical associations and implications for schizophrenia. *Schizophrenia Research* 33, 3 (Oct. 1998), 133–140.
- [43] GOODLETT, C., DAVIS, B., JEAN, R., GILMORE, J., AND GERIG, G. Improved correspondance for DTI population studies via unbiased atlas building. In *Medical Image Computing and Computer Assisted Intervention (MICCAI)* (2006), vol. 4191 of *LNCS*, Springer-Verlag, pp. 260–267.
- [44] GUO, A. C., PETRELLA, J. R., KURTZBERG, J., AND PROVENZALE, J. M. Evaluation of White Matter Anisotropy in Krabbe Disease with Diffusion Tensor MR Imaging: Initial Experience. *Radiology* 218, 3 (2001), 809–815.

- [45] HAINES, D. E. *Fundamental Neuroscience for Basic and Clinical Applications*, third ed. Churchill Livingstone, 2005.
- [46] HASAN, K. M., PARKER, D. L., AND ALEXANDER, A. L. Comparison of gradient encoding schemes for diffusion-tensor MRI. *Journal of Magnetic Resonance Imaging* 13, 5 (2001), 769–780.
- [47] HERMOYE, L., SAINT-MARTIN, C., COSNARD, G., LEE, S.-K., KIM, J., NASSOGNE, M.-C., MENTEN, R., CLAPUYT, P., DONOHUE, P. K., HUA, K., WAKANA, S., JIANG, H., VAN ZIJL, P. C., AND MORI, S. Pediatric diffusion tensor imaging: Normal database and observation of the white matter maturation in early childhood. *NeuroImage* 29, 2 (2006), 493–504.
- [48] JONES, D., GRIFFIN, L., ALEXANDER, D., CATANI, M., HORSFIELD, M., HOWARD, R., AND WILLIAMS, S. Spatial normalization and averaging of diffusion tensor MRI data sets. *Neuroimage* 17, 2 (2002), 592–617.
- [49] JONES, D. K. The effect of gradient sampling schemes on measures derived from diffusion tensor MRI: A monte carlo study. *Magnetic Resonance in Medicine* 51, 4 (2004), 807–815.
- [50] JONES, D. K., AND BASSER, P. J. Squashing peanuts and smashing pumpkins: How noise distorts diffusion-weighted MR data. *Magnetic Resonance in Medicine* 52, 5 (2004), 979–993.
- [51] JONES, D. K., SYMMS, M. R., CERCIGNANI, M., AND HOWARD, R. J. The effect of filter size on VBM analyses of DT-MRI data. *NeuroImage* 26, 2 (June 2005), 546–554.
- [52] JONES, D. K., TRAVIS, A. R., EDEN, G., PIERPAOLI, C., AND BASSER, P. J. PASTA: pointwise assessment of streamline tractography attributes. *Magnetic Resonance in Medicine* 53, 6 (2005), 1462–1467.
- [53] JOSHI, S., DAVIS, B., JOMIER, M., AND GERIG, G. Unbiased diffeomorphic atlas construction for computational anatomy. *NeuroImage* 23, Supplement1 (Nov. 2004), S151–S160.
- [54] KAILATH, T. The divergence and bhattacharyya distance measures in signal selection. *Communication Technology, IEEE Transactions on* 15, 1 (1967), 52–60.
- [55] KOAY, C. G., CAREW, J. D., ALEXANDER, A. L., BASSER, P. J., AND MEYERAND, M. E. Investigation of anomalous estimates of tensor-derived quantities in diffusion tensor imaging. *Magnetic Resonance in Medicine* 55, 4 (2006), 930–936.
- [56] KREHER, B. W., SCHNEIDER, J. F., MADER, I., MARTIN, E., HENNIG, J., AND IL'YASOV, K. A. Multitensor approach for analysis and tracking of complex fiber configurations. *Magnetic Resonance in Medicine* 24, 5 (2005), 1216–1225.

- [57] KUBICKI, M., PARK, H., WESTIN, C., NESTOR, P., MULKERN, R., MAIER, S., NIZNIKIEWICZ, M., CONNOR, E., LEVITT, J., FRUMIN, M., KIKINIS, R., JOLESZ, F., MCCARLEY, R., AND SHENTON, M. DTI and MTR abnormalities in schizophrenia: Analysis of white matter integrity. *NeuroImage* 26, 3 (July 2005), 1109–1118.
- [58] KUBICKI, M., WESTIN, C.-F., MAIER, S. E., FRUMIN, M., NESTOR, P. G., SALISBURY, D. F., KIKINIS, R., JOLESZ, F. A., MCCARLEY, R. W., AND SHENTON, M. E. Uncinate Fasciculus Findings in Schizophrenia: A Magnetic Resonance Diffusion Tensor Imaging Study. *Am J Psychiatry* 159, 5 (2002), 813–820.
- [59] KUBICKI, M., WESTIN, C.-F., MCCARLEY, R. W., AND SHENTON, M. E. The application of DTI to investigate white matter abnormalities in schizophrenia. *Annals of the New York Academy of Sciences* 1064, 1 (2005), 134–148.
- [60] LE BIHAN, D., AND BRETON, E. Imagerie de diffusion in vivo par résonance magnétique nucléaire. *Comptes Rendus de l'Académie des Sciences* 301, 15 (1985), 1109–1112.
- [61] LENGLET, C., ROUSSON, M., DERICHE, R., FAUGERAS, O. D., LEHERICY, S., AND UGURBIL, K. A riemannian approach to diffusion tensor images segmentation. In *Information Processing in Medical Imaging (IPMI)* (2005), pp. 591–602.
- [62] LIM, K., AND HELPERN, J. Neuropsychiatric applications of DTI - a review. *NMR in Biomedicine* 15, 7-8 (2002), 587–593.
- [63] LIN, F., YU, C., JIANG, T., LI, K., LI, X., QIN, W., SUN, H., AND CHAN, P. Quantitative analysis along the pyramidal tract by length-normalized parameterization based on diffusion tensor tractography: Application to patients with relapsing neuromyelitis optica. *Neuroimage* 33, 1 (Oct. 2006), 154–160.
- [64] MADDAH, M., GRIMSON, W. E. L., WARFIELD, S. K., AND WELLS, W. M. A unified framework for clustering and quantitative analysis of white matter fiber tracts. *Medical Image Analysis* 12, 2 (2008), 191–202.
- [65] MADDAH, M., KUBICKI, M., WELLS, W. M., WESTIN, C.-F., SHENTON, M. E., AND GRIMSON, W. E. L. Findings in schizophrenia by tract-oriented DT-MRI analysis. In *Medical Image Computing and Computer-Assisted Intervention - MICCAI 2008* (2008), vol. 5241 of *Lecture Notes in Computer Science*, Springer-Verlag, pp. 917–924.
- [66] MANGIN, J.-F., POUPON, C., CLARK, C., BIHAN, D. L., AND BLOCH, I. Distortion correction and robust tensor estimation for MR diffusion imaging. *Medical Image Analysis* 6, 3 (Sept. 2002), 191–198.

- [67] McROBBIE, D. W., MOORE, E. A., GRAVES, M. J., AND PRINCE, M. R. *MRI: From Picture to Proton*, second ed. Cambridge University Press, 2006.
- [68] MELONAKOS, J., MOHAN, V., NIETHAMMER, M., SMITH, K., KUBICKI, M., AND TANNENBAUM, A. Finsler tractography for white matter connectivity of the cingulum bundle. In *Medical Image Computing and Computer Assisted Intervention (MICCAI)* (2007), vol. 4791 of *LNCS*, Springer-Verlag, pp. 36–43.
- [69] MELONAKOS, J., PICHON, E., ANGENENT, S., AND TANENBAUM, A. Finsler active contours. *IEEE Transactions on Pattern Analysis and Machine Intelligence* 30, 3 (Mar. 2008), 412–423.
- [70] MORI, S., ITOH, R., ZHANG, J., KAUFMANN, W. E., VAN ZIJL, P. C., SOLAIYAPPAN, M., AND YAROWSKY, P. Diffusion tensor imaging of the developing mouse brain. *Magn Reson Med* 46, 1 (2001), 18–23.
- [71] MORI, S., WAKANA, S., NAGAE-POETSCHER, L. M., AND VAN ZIJL, P. C. *MRI Atlas of Human White Matter*, 1st edition ed. Elsevier, 2005.
- [72] MUESER, K. T., AND MCGURK, S. R. Schizophrenia. *The Lancet* 363, 9426 (2004), 2063 – 2072.
- [73] MUIRHEAD, R. J. *Aspects of Multivariate Statistical Theory*. Wiley, 2005.
- [74] NICHOLS, T. E., AND HOLMES, A. P. Nonparametric analysis of functional neuroimaging: A primer with examples. *Human Brain Mapping* 15, 1 (2002), 1–25.
- [75] O’DONNELL, L., AND WESTIN, C.-F. Automatic tractography segmentation using a high-dimensional white matter atlas. *Medical Imaging, IEEE Transactions on* 26, 11 (Nov. 2007), 1562–1575.
- [76] O’DONNELL, L. J., WESTIN, C.-F., AND GOLBY, A. J. Tract-based morphometry for white matter group analysis. *NeuroImage* 45, 3 (2009), 832 – 844.
- [77] ÖZARSLAN, E., AND MARECI, T. H. Generalized diffusion tensor imaging and analytical relationships between diffusion tensor imaging and high angular resolution diffusion imaging. *Magnetic Resonance in Medicine* 50, 5 (24 Nov. 2003), 955–965.
- [78] ÖZARSLAN, E., VEMURI, B. C., AND MARECI, T. H. Generalized scalar measures for diffusion MRI using trace, variance, and entropy. *Magnetic Resonance in Medicine* 53 (2005), 866 – 876.
- [79] PELED, S. New perspectives on the sources of white matter DTI signal. *Medical Imaging, IEEE Transactions on* 26, 11 (2007), 1448–1455.

- [80] PELED, S., FRIMAN, O., JOLESZ, F., AND WESTIN, C.-F. Geometrically constrained two-tensor model for crossing tracts in DWI. *Magnetic Resonance in Medicine* 24, 9 (2006), 1263–1270.
- [81] PENNEC, X., FILLARD, P., AND AYACHE, N. A riemannian framework for tensor computing. *International Journal of Computer Vision* 66, 1 (January 2006), 41–66.
- [82] PEYRAT, J.-M., SERMESANT, M., PENNEC, X., DELINGETTE, H., CHENYANG XU, MCVEIGH, E., AND AYACHE, N. A computational framework for the statistical analysis of cardiac diffusion tensors: Application to a small database of canine hearts. *Medical Imaging, IEEE Transactions on* 26, 11 (Nov. 2007), 1500–1514.
- [83] PIERPAOLI, C., AND BASSER, P. J. Toward a quantitative assessment of diffusion anisotropy. *Magnetic Resonance in Medicine* 36, 6 (Dec. 1996), 1996.
- [84] RAMSAY, J., AND SILVERMAN, B. *Functional Data Analysis*, second ed. Springer, 2005.
- [85] ROUSSEEUW, P., AND VAN DRIESEN, K. A fast algorithm for the minimum covariance determinant estimator. *Technometrics* 41 (1999), 212–223.
- [86] RUECKERT, D., SONODA, L., HAYES, C., HILL, D., LEACH, M., AND HAWKES, D. Nonrigid registration using free-form deformations: application to breast mr images. *Medical Imaging, IEEE Transactions on* 18, 8 (1999), 712–721.
- [87] SALVADOR, R., PEÑA, A., MENON, D. K., CARPENTER, T. A., PICKARD, J. D., AND BULLMORE, E. T. Formal characterization and extension of the linearized diffusion tensor model. *Human Brain Mapping* 24, 2 (Feb. 2005), 144–155.
- [88] SCHMITHORST, V. J., WILKE, M., DARDZINSKI, B. J., AND HOLLAND, S. K. Correlation of White Matter Diffusivity and Anisotropy with Age during Childhood and Adolescence: A Cross-sectional Diffusion-Tensor MR Imaging Study. *Radiology* 222, 1 (2002), 212–218.
- [89] SCHNABEL, J. A., RUECKERT, D., QUIST, M., BLACKALL, J. M., CASTELLANO-SMITH, A. D., HARTKENS, T., PENNEY, G. P., HALL, W. A., LIU, H., TRUWIT, C. L., GERRITSEN, F. A., HILL, D. L. G., AND HAWKES, D. J. A generic framework for non-rigid registration based on non-uniform multi-level free-form deformations. In *MICCAI '01: Proceedings of the 4th International Conference on Medical Image Computing and Computer-Assisted Intervention* (2001), Springer-Verlag, pp. 573–581.
- [90] SIJBERS, J., AND DEN DEKKER, A. Maximum likelihood estimation of signal amplitude and noise variance from MR data. *Magnetic Resonance in Medicine* 51, 3 (Mar. 2004), 586–594.

- [91] SIJBERS, J., DEN DEKKER, A. J., SCHEUNDERS, P., AND DYCK, D. V. Maximum-likelihood estimation of rician distribution parameters. *Medical Imaging, IEEE Transactions on* 17, 3 (June 1998), 357–361.
- [92] SKARE, S., LI, T.-Q., NORDELL, B., AND INGVAR, M. Noise considerations in the determination of diffusion tensor anisotropy. *Magnetic Resonance Imaging* 18, 6 (July 2000), 659–669.
- [93] SMITH, S. M., JENKINSON, M., JOHANSEN-BERG, H., RUECKERT, D., NICHOLS, T. E., MACKAY, C. E., WATKINS, K. E., CICCARELLI, O., CADER, M. Z., MATTHEWS, P. M., AND BEHRENS, T. E. Tract-based spatial statistics: Voxelwise analysis of multi-subject diffusion data. *NeuroImage* 31 (2006), 1487–1505.
- [94] SMITH, S. M., JENKINSON, M., WOOLRICH, M. W., BECKMANN, C. F., BEHRENS, T. E., JOHANSEN-BERG, H., BANNISTER, P. R., LUCA, M. D., DROBNJAK, I., FLITNEY, D. E., NIAZY, R. K., SAUNDERS, J., VICKERS, J., ZHANG, Y., STEFANO, N. D., BRADY, J. M., AND MATTHEWS, P. M. Advances in functional and structural mr image analysis and implementation as fsl. *NeuroImage* 23, Supplement 1 (2004), S208 – S219. Mathematics in Brain Imaging.
- [95] SNOOK, L., PLEWES, C., AND BEAULIEU, C. Voxel based versus region of interest analysis in diffusion tensor imaging of neurodevelopment. *NeuroImage* 34, 1 (1 Jan. 2007), 243–252.
- [96] SONG, S.-K., SUN, S.-W., RAMSBOTTOM, M. J., CHANG, C., RUSSELL, J., AND CROSS, A. H. Dysmyelination revealed through mri as increased radial (but unchanged axial) diffusion of water. *NeuroImage* 17, 3 (2002), 1429 – 1436.
- [97] STEJSKAL, E., AND TANNER, J. Spin diffusion measurements: Spin echoes in the presence of a time-dependent field gradient. *Journal of Chemical Physics* 42, 1 (1965), 288–292.
- [98] STUDHOLME, C., HILL, D. L. G., AND HAWKES, D. J. An overlap invariant entropy measure of 3d medical image alignment. *Pattern Recognition* 32, 1 (1999), 71 – 86.
- [99] SYDYKOVA, D., STAHL, R., DIETRICH, O., EWERS, M., REISER, M. F., SCHOENBERG, S. O., MÖLLER, H.-J., HAMPEL, H., AND TEIPEL, S. J. Alzheimer’s disease: A diffusion tensor imaging and voxel-based morphometry study. *Cerebral Cortex* 17, 10 (2007), 2276–2282. In Press.
- [100] TAO, X., AND MILLER, J. V. A method for registering diffusion weighted magnetic resonance images. In *Medical Image Computing and Computer Assisted Intervention (MICCAI)* (2006), vol. 4191 of *LNCS*, pp. 594–602.
- [101] TOGA, A. W., AND MAZZIOTTA, J. C., Eds. *Brain Mapping: The Methods*, 2nd ed. Elsevier Science, 2002.

- [102] TUCH, D. S. Q-ball imaging. *Magnetic Resonance in Medicine* 52, 6 (2004), 1358–1372.
- [103] TUCH, D. S., REESE, T. G., WIEGELL, M. R., MAKRIS, N., BELLIVEAU, J. W., AND WEDEEN, V. J. High angular resolution diffusion imaging reveals intravoxel white matter fiber heterogeneity. *Magnetic Resonance in Medicine* 48, 4 (Sept. 2002), 577–582.
- [104] VAN LEEMPUT, K., MAES, F., VANDERMEULEN, D., AND SUETENS, P. Automated model-based bias field correction of MR images of the brain. *IEEE Trans Med Imaging* 18, 10 (1999), 885–96.
- [105] VAN LEEMPUT, K., MAES, F., VANDERMEULEN, D., AND SUETENS, P. Automated model-based tissue classification of MR images of the brain. *IEEE Trans Med Imaging* 18, 10 (1999), 897–908.
- [106] WANG, Z., AND VEMURI, B. DTI segmentation using an information theoretic tensor dissimilarity measure. *Medical Imaging, IEEE Transactions on* 24, 10 (Oct. 2005), 1267–1277.
- [107] WARNER, T. D., BEHNKE, M., EYLER, F. D., PADGETT, K., LEONARD, C., HOU, W., GARVAN, C. W., SCHMALFUSS, I. M., AND BLACKBAND, S. J. Diffusion tensor imaging of frontal white matter and executive functioning in cocaine-exposed children. *Pediatrics* 118, 5 (Nov. 2006), 2014–2024.
- [108] WESTIN, C.-F., MAIER, S., MAMATA, H., NABAVI, A., JOLESZ, F., AND KIKINIS, R. Processing and visualization for diffusion tensor MRI. *Medical Image Analysis* 6, 2 (June 2002), 93–108.
- [109] XU, D., HAO, X., BANSAL, R., PLESSEN, K. J., AND PETERSON, B. S. Seamless warping of diffusion tensor fields. *Medical Imaging, IEEE Transactions on* 27, 3 (Mar. 2008), 285–299.
- [110] XU, D., MORI, S., SHEN, D., VAN ZIJL, P. C., AND DAVATZIKOS, C. Spatial normalization of diffusion tensor fields. *Magnetic Resonance in Medicine* 50, 1 (July 2003), 175–182.
- [111] XU, S., STYNER, M., GILMORE, J., PIVEN, J., AND GERIG, G. Multivariate nonlinear mixed model to analyze longitudinal image data: Mri study of early brain development. In *Computer Vision and Pattern Recognition Workshops, 2008. CVPRW '08. IEEE Computer Society Conference on* (June 2008), pp. 1–8.
- [112] YUSHKEVICH, P. A., ZHANG, H., SIMON, T. J., AND GEE, J. C. Structure-specific statistical mapping of white matter tracts. *NeuroImage* 41, 2 (June 2008), 448–461.
- [113] ZHANG, F., HANCOCK, E. R., GOODLETT, C., AND GERIG, G. Probabilistic white matter fiber tracking using particle filtering and von mises-fisher sampling. *Medical Image Analysis* 13, 1 (2008), 5–18.

- [114] ZHANG, H., AVANTS, B. B., YUSHKEVICH, P. A., WOO, J. H., WANG, S., McCLUSKEY, L. F., ELMAN, L. B., MELHEM, E. R., AND GEE, J. C. High-dimensional spatial normalization of diffusion tensor images improves the detection of white matter differences in amyotrophic lateral sclerosis. *Medical Imaging, IEEE Transactions on - Special Issue on Computational Diffusion MRI* 26, 11 (Nov. 2007), 1585–1597.
- [115] ZHANG, H., YUSHKEVICH, P. A., ALEXANDER, D. C., AND GEE, J. C. Deformable registration of diffusion tensor MR images with explicit orientation optimization. *Medical Image Analysis* 10, 5 (2006), 764–785.
- [116] ZHU, H., IBRAHIM, J., TANG, N., ROWE, D., HAO, X., BANSAL, R., AND PETERSON, B. A statistical analysis of brain morphology using wild bootstrapping. *Medical Imaging, IEEE Transactions on* 26, 7 (July 2007), 954–966.
- [117] ZIYAN, U., SABUNCU, M. R., O'DONNELL, L. J., AND WESTIN, C.-F. Nonlinear registration of diffusion MR images based on fiber bundles. In *Medical Image computing and Computer Assisted Intervention (MICCAI)* (2007), vol. 4791 of *LNCS*, Springer-Verlag, pp. 351–358.